DISSERTATION

BARIUM TAGGING IN SOLID XENON FOR THE EXO EXPERIMENT

Submitted by

Brian Mong

Department of Physics

In partial fulfillment of the requirements

For the Degree of Doctor of Philosophy

Colorado State University

Fort Collins, Colorado

Fall 2011

Doctoral Committee:

Advisor: William Fairbank, Jr.

Stephen Lundeen
Bruce Berger
Alan Van Orden

ABSTRACT

BARIUM TAGGING IN SOLID XENON FOR THE EXO EXPERIMENT

Neutrinoless double beta decay experiments are searching for rare decay modes never before observed to uncover the absolute mass of the neutrino, as well as to discover if it is a Majorana fermion. Detection of the daughter nucleus can help provide positive identification of this event over most radioactive backgrounds. The goal of the Enriched Xenon Observatory (EXO) is to measure the rate of $0\nu\beta\beta$ decay in ^{136}Xe , incorporating ^{136}Ba daughter identification by laser induced fluorescence spectroscopy. Here, we investigate a technique in which the ^{136}Ba daughter is grabbed with a cryogenic probe by freezing it in solid xenon ice, and detected directly in the solid xenon.

The absorption and fluorescence spectra of barium in solid xenon were observed for the first time in this work. Identification of the $6s^2\ {}^1S_0 \rightarrow 6s6p\ {}^1P_1$ transition in both absorption (558 nm) and emission spectra (594 nm) were made. Additional blue absorption and emission lines were observed, but their transitions were not identified. Saturation of the $6s^2\ {}^1S_0 \rightarrow 6s6p\ {}^1P_1$ transition was not observed with increased excitation rates using resonance excitation at 558 nm. From this a limit on the metastable decay rate was deduced to be greater than 10^4 s^{-1}. Finally a fluorescence spectrum was obtained from a sample with only 20,000 atoms in the laser beam. With potential improvements of 10^7 in detection efficiency, single barium atom detection seems possible in solid xenon. A fiber probe detector based on a bare single mode fiber

was also constructed and tested with fluorescing dye molecules. Successful detection of a few dye molecules in solution at the probe tip was demonstrated.

ACKNOWLEDGMENTS

I would like to thank first of all my parents with who's loving support made it possible to have the opportunities that I have been given. The wisdom I have received from them I will cherish most of all and which has made me a successful person. Also thanks to my sister who has been always been encouraging, and whom I respect and thank greatly for her service to our country and for my freedom.

To Richard Sonnenfeld, my advisor at NMT, who has been more than a great advisor, but a great friend and role model even to today. Also a shout out to all my friends at NMT that have made those four years truly memorable.

To Bill Fairbank, I can never thank you enough for the opportunity you have given me. The work was exciting and difficult and everything I had hoped. I only hope to someday be as gifted a physicist and scientist. Also thanks to EXO as a whole for having an interesting problem to solve, and a fun project to work on. Thanks to my lab-mates in particular who were great sounding boards, and in particular Shon for the work we did together.

Lastly but most importantly thanks to my wife and best friend Heather who I have to thank for everything. Without you support, encouragement, and love I would not have the honor to present this work.

TABLE OF CONTENTS

LIST OF FIGURES

LIST OF TABLES

Chapter 1

Introduction

1.1 Overview

While substantial evidence has been collected to indicate neutrinos have mass, the actual masses of the three neutrinos have not been established. To learn more about neutrinos, the Enriched Xenon Observatory (EXO) experiment is searching for neutrinoless double beta decay ($0\nu\beta\beta$) in ^{136}Xe

$$^{136}Xe \rightarrow ^{136}Ba + 2e^{-}. \tag{1.1}$$

Observation of this decay would be direct evidence that the neutrino is its own antiparticle, and would give information on the absolute neutrino mass [1]. In order to accurately measure this decay rate, EXO is preparing a unique method for rejection of background events based on detection of the ^{136}Ba daughter ion or atom by laser induced fluorescence, a technique called 'tagging' [2]. This would provide an additional level of confirmation for the identification of double beta decay events, while

discriminating against radioactive backgrounds from the detector materials and environment. Such backgrounds ultimately become the limiting factor in any other $0\nu\beta\beta$ search.

A brief review of neutrino history and properties is given in this chapter, including results that demonstrate neutrinos have a small but finite mass. The physics of measuring the neutrino masses using $0\nu\beta\beta$ is then outlined. The current EXO experiment without tagging (EXO-200), and its successor which is planned to be a ton scale experiment with barium tagging (EXO) are discussed. EXO is currently in development, with several competing tagging methods being explored within the EXO collaboration.

In Chapters 2-5 the development of a potential tagging technique for EXO is discussed. The core principle of this technique is trapping the ^{136}Ba daughter in solid xenon using a cryogenic probe, and detecting it via laser spectroscopy in the solid. The final charge state of the daughter ^{136}Ba is unknown in the solid, but is likely to be Ba^+ or neutral[1]. Laser induced fluorescence spectroscopy of many neutral barium atoms in solid xenon is demonstrated in this work as the initial step in development of this tagging scheme. A cryogenic probe with a single-mode fiber is considered as a method to detect a single ^{136}Ba daughter. In this scheme the probe's fiber brings excitation light to the ^{136}Ba atom or ion frozen to the tip, and collects the fluorescence. A single-mode fiber optic probe was built and tested to determine feasibility for single barium atom detection. Results are presented for detection of Rhodamine-6G dye molecules in solution, as well as quantum dots, which were used as barium analogues.

[1]This work does not adddress this question, but studies with barium deposited in singly and doubly ionized states are being investigated with the same apparatus by another researcher.

1.2 Neutrinos

The neutrino (ν) was first proposed by Wolfgang Pauli in 1930 as an explanation to the apparent non-conservation of spin and energy observed in β-decay,

$$(A, Z) \rightarrow (A, Z + 1) + e^{-} + \bar{\nu_e}. \tag{1.2}$$

In this decay, the neutrino carries spin=1/2 and the remaining decay energy with it, which had gone undetected in the initial measurements. The neutrino was eventually confirmed by detection of the reverse process, called inverse beta decay

$$\bar{\nu_e} + p^{+} \rightarrow \beta^{+} + n^{0} \tag{1.3}$$

in 1956 by Cowan and Reines et. al. [3]. Raymond Davis used inverse beta decay to measure the neutrino flux originating from the sun by the reaction

$$\nu_e + {}^{37}Cl \rightarrow {}^{37}Ar + e^{-} \tag{1.4}$$

with the Homestake chlorine detector. The measurement was found to be significantly below all predictions [4, 5]. This deficiency is now known to be due to neutrino flavor mixing [6], a theory first put forth by B. Pontecorvo [7].

1.2.1 Neutrino Oscillations

The results of several neutrino oscillation experiments have provided substantial evidence for neutrino flavor mixing, requiring that neutrinos have mass, contrary to the Standard Model of particle physics [8]. These experiments may be categorized by

the neutrino source studied. Some examples of experiments in theses categories are: solar neutrinos which were measured by the Homestake experiment, SNO [9], and Borexino [10]; atmospheric neutrinos measured by Super Kamiokande [11]; reactor neutrinos measured by KamLAND [12]; and neutrino beam measurements made by K2K [13], and MINOS [14].

Neutrino oscillations arise because the neutrino flavor eigenstates (ν_e, ν_τ, and ν_μ) are mixtures of neutrino mass eigenstates (m_1, m_2, and m_3). A transformation matrix $U_{\alpha i}$ relates the two bases

$$|\nu_\alpha\rangle = \sum_i U^*_{\alpha i} |\nu_i\rangle \tag{1.5}$$

where α denotes flavor eigenstates and i denotes mass eigenstates. This matrix is called the Pontecorvo-Maki-Nakagawa-Sakata transformation matrix and has the form

$$U = \begin{pmatrix} 1 & 0 & 0 \\ 0 & c_{23} & s_{23} \\ 0 & -s_{23} & c_{23} \end{pmatrix} \begin{pmatrix} c_{13} & 0 & s_{13}e^{-i\delta} \\ 0 & 1 & 0 \\ -s_{13}e^{i\delta} & 0 & c_{13} \end{pmatrix} \begin{pmatrix} c_{12} & s_{12} & 0 \\ -s_{12} & c_{12} & 0 \\ 0 & 0 & 1 \end{pmatrix} \tag{1.6}$$

where $c_{ij} = \cos\theta_{ij}$, $s_{ij} = \sin\theta_{ij}$ [15]. The angle (θ_{ij}) is known as the mixing angle, and the phase δ contains information on violation of Charge-Parity (CP) symmetry.

Oscillations arise because the phase of the waveforms of the neutrino traveling from emitted source to detector in quantum mechanics oscillates at a frequency proportional to its momentum, which is related to its mass

$$|v_i(t)\rangle = e^{-i(E_i t - \vec{p_i}\cdot\vec{x})/\hbar} |v_i(0)\rangle \ . \tag{1.7}$$

Since neutrinos are ultra-relativistic ($E \simeq pc$), Eqn. 1.7 can be simplified as

$$|v_i(t)\rangle = e^{-im_i^2 \frac{L}{2E}} |v_i(0)\rangle \ . \tag{1.8}$$

The emitted neutrino, in an initial flavor eigenstate α, travels from the source as a mixture of mass eigenstates, as described by the Dirac equation, to the detector. There the neutrino can be detected in flavor eigenstate β with a probability given by

$$P_{\alpha\to\beta} = \left| \delta_{\beta\alpha} + \sum_{i\geq 2} U_{\beta i} U^*_{\alpha i} \left(e^{-i\Delta m^2_{i1} \frac{L}{2E}} - 1 \right) \right|^2 \ , \tag{1.9}$$

where $\Delta m^2_{ij} = m^2_i - m^2_1$, L is the distance from source to detector, and E is the neutrino energy [16]. Oscillations therefore require that neutrinos be non-trivial mixtures of mass eigenstates, i.e. the mixing angles θ_{12}, θ_{23}, and θ_{13} cannot all be zero, with nonzero mass differences.

In many oscillation measurements, the experiment is primarily sensitive to only two of the mass eigenstates. In this case the transformation matrix behaves like a 2-D rotation matrix

$$U = \begin{pmatrix} \cos\theta & \sin\theta \\ -\sin\theta & \cos\theta \end{pmatrix} . \tag{1.10}$$

The probability for a neutrino with energy (E) to change flavor from a source to the detector a distance (L) away is then given by:

$$P\left(\nu_\alpha \to \nu_\beta\right) = \sin^2\left(2\theta\right) \sin^2\left(1.27 \frac{\Delta m^2(eV^2) L(km)}{E(GeV)}\right), \tag{1.11}$$

where Δm^2 is defined as

$$\Delta m^2_{ij} = \left| m^2_i + m^2_j \right| . \tag{1.12}$$

The two neutrino approximation is appropriate when the sizes of the other possible oscillation effects are small. In most cases, the 1-3 oscillations are too small to observe because the oscillation amplitude is set by the mixing parameter θ_{13}, which is much smaller than θ_{12} and θ_{23}. The oscillation wavelengths are set by the size of Δm^2, so some measurements are only sensitive to the shorter-wavelength oscillations where the longer-wavelength 2-3 oscillations have not yet become significant.

A synthesis of results (2008) from several oscillation experiments [15] give the values for the mixing angles as ($\pm 2\sigma$):

$$\sin^2(\theta_{12}) = 0.312^{0.040}_{0.034} \tag{1.13}$$

$$\sin^2(\theta_{23}) = 0.466^{0.136}_{0.100} \tag{1.14}$$

$$\sin^2(\theta_{13}) < 3.6 \times 10^{-2}, \tag{1.15}$$

and mass differences for the eigenstates as

$$\left| m^2_3 - \frac{m^2_2 + m^2_1}{2} \right| = 2.39^{+0.27}_{-0.20} \times 10^{-3} eV^2 \tag{1.16}$$

$$\Delta m^2_{21} = 7.68^{+0.34}_{-0.36} \times 10^{-5} eV^2. \tag{1.17}$$

There is new experimental evidence that suggests $\sin^2(\theta_{13})$ is nonzero [17, 18].

These known quantities are summarized graphically in Fig. 1.1. Mass eigenstates are represented as color bars which show the probability of that mass state being measured in a particular flavor eigenstate. Because oscillation experiments are sen-

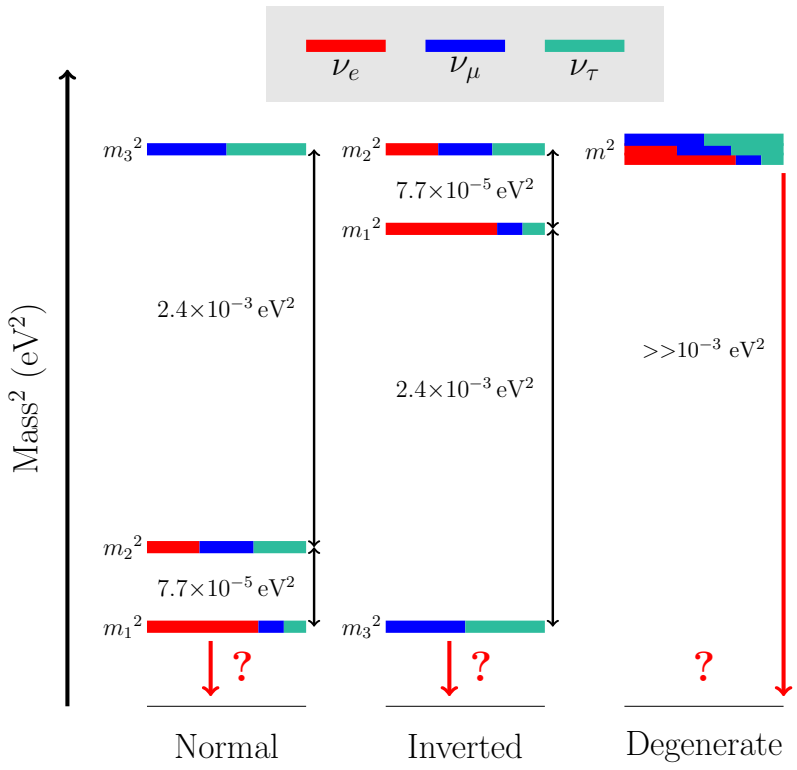

Figure 1.1: Diagram of neutrino mixing, absolute mass, and hierarchy problem.

sitive to the absolute value of the mass difference (Eqn. 1.16), the hierarchy of the masses remains unknown as well as the overall mass scale. The 'Normal' hierarchy is defined as having the small mass splitting lower than m_3, while 'Inverted' hierarchy has the small mass splitting above the m_3. The 'Degenerate' hierarchy is where the absolute mass is large enough that the mass splittings are relatively small. The major problems left in understanding neutrinos are determining the absolute mass scale, measuring θ_{13}, determining if neutrinos are their own anti-particles, and probing the CP-violation phase δ.

1.2.2 Absolute Neutrino Mass

Several experiments have placed upper limits on the absolute neutrino mass. The most direct search has been done by measuring the β-decay spectrum near the endpoint in tritium (^3H) and comparing the measured energy spectrum to a theoretical one with $m_\nu = 0$. This measurement has been performed in two independent experiments (Mainz and Troitsk) to give a combined limit of $\langle m \rangle < 1.8$ eV [19]. Soon a larger β-decay endpoint experiment named KATRIN will start taking data, with an anticipated mass sensitivity of < 0.2 eV [20].

Cosmological measurements have also been able to set limits on the neutrino mass. By combining several cosmological measurements (WMAP5+SDSS LRG+ SDSS, DEEP2, and LBG bg) the combined neutrino mass is found to be less than 0.28 eV ($\Sigma m_\nu < 0.28$ eV) [21]. Since this measurement is highly model dependent, this result is not considered a solid limit [22].

1.2.3 Neutrinoless Double Beta Decay

There are two possible decay modes for double beta decay: $2\nu\beta\beta$

$$(A, Z) \rightarrow (A, Z + 2) + 2e^- + 2\bar{\nu}_e \ , \tag{1.18}$$

and $0\nu\beta\beta$

$$(A, Z) \rightarrow (A, Z + 2) + 2e^- \ . \tag{1.19}$$

This second decay is only possible if the neutrino is its own antiparticle, in which the neutrino is called a Majorana particle. No fundamental particle is currently known to be a Majorana particle, but neutrinos are potential candidates [8]. These decay modes are shown in Fig. 1.2. The $2\nu\beta\beta$ is a standard second order decay. In $0\nu\beta\beta$ decay an antineutrino from one beta decay vertex is absorbed as a neutrino in the other beta decay vertex, which is only possible if the neutrino is a Majorana particle. $2\nu\beta\beta$ decays have been observed in about a dozen isotopes, and are predicted in many

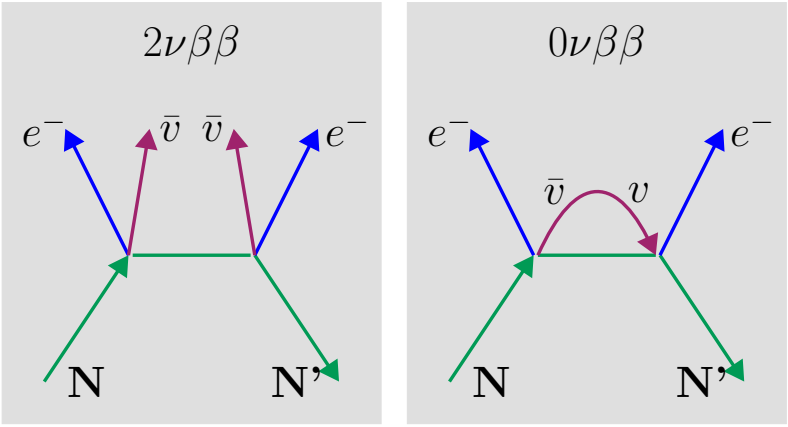

Figure 1.2: Double beta decay process diagram for $2\nu\beta\beta$ and $0\nu\beta\beta$.

others [23], but $0\nu\beta\beta$ has yet to be observed with certainty for any isotope. Isotopes

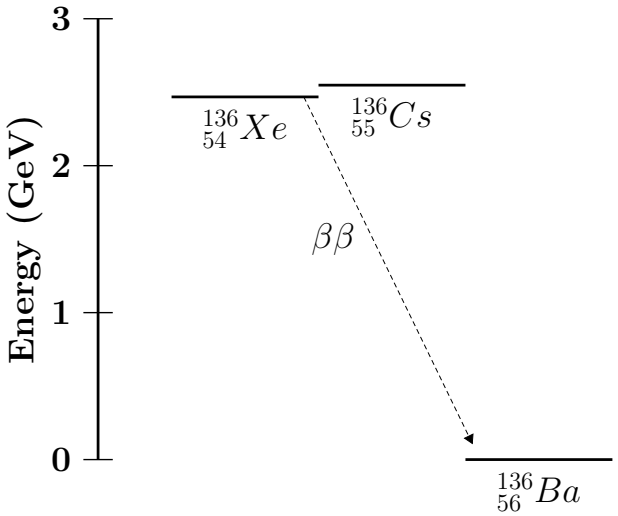

Figure 1.3: Nuclear energy states for for A=136. The double beta decay energy is $Q_{\beta\beta} = 2457.83(37)$KeV.

used for double-beta decay experiments have energetically forbidden 'single' β-decay which would otherwise dominate in the detector. For example, the beta decay in ^{136}Xe to ^{136}Cs cannot occur, as shown in Fig. 1.3. The decay energy, $Q_{\beta\beta}$ in both modes is the energy difference of the parent and daughter nuclear states. For ^{136}Xe the end point energy is $Q_{\beta\beta} = 2457.83(37)$KeV [24].

It is possible to distinguish $0\nu\beta\beta$ from $2\nu\beta\beta$ events by measuring the energy of the electrons produced in the decay. This is demonstrated with Monte-Carlo simulation of ^{136}Xe in Fig. 1.4 showing the energy distribution of the two decay modes. In $2\nu\beta\beta$ the electrons share the decay energy with the neutrinos, which are not detected, giving a continuous decay energy spectrum up to the decay energy. In $0\nu\beta\beta$ essentially all of the decay energy goes to the electrons since no neutrinos are produced, resulting in a delta function at the decay energy.

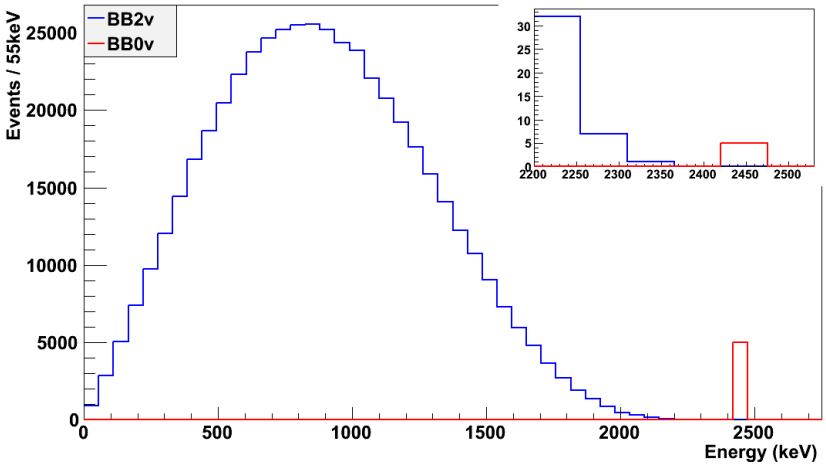

Figure 1.4: $2\nu\beta\beta$ and $0\nu\beta\beta$ electron energy spectrum for $0\nu\beta\beta$:$2\nu\beta\beta$ ratio of 1:100 (1:1$\times 10^5$ inset) assuming 500,000 $2\nu\beta\beta$ events.

The effective neutrino mass ($\langle m_\nu \rangle$) is related to the $0\nu\beta\beta$ half-life measurement [25] ($T_{1/2}^{0\nu\beta\beta}$) by

$$\langle m_\nu \rangle^2 = \left(T_{1/2}^{0\nu\beta\beta} G^{0\nu\beta\beta}(E_0, Z) \left| M_{GT}^{0\nu\beta\beta} - \frac{g_V^2}{g_A^2} M_F^{0\nu\beta\beta} \right|^2 \right)^{-1}, \tag{1.20}$$

where $G^{0\nu\beta\beta}(E_0, Z)$ is a known phase space factor, $M_{GT}^{0\nu\beta\beta}$ and $M_F^{0\nu\beta\beta}$ are nuclear matrix elements calculated from models, and $\langle m_\nu \rangle$ defined as

$$\langle m_\nu \rangle = \sum_i m_i {U_{ei}}^2. \tag{1.21}$$

The absolute neutrino masses can be solved for using our knowledge of $U_{\alpha i}$ and the mass squared differences from neutrino oscillations. Even by setting a limit then on the $T_{1/2}^{0\nu\beta\beta}$ $0\nu\beta\beta$ searches can set upper limits on the effective Majorana neutrino mass.

The Heidelberg-Moscow experiment, conducted at Gran Sasso, is the most sensitive $0\nu\beta\beta$ search in ^{76}Ge which some of the experimenters have claimed a significant observation (6σ), which gives $\langle m \rangle = 0.32^{+0.03}_{-0.03}$ eV [26]. This claim is controversial and drew immediate criticism [27, 28], as well as a retraction from one of the original authors [29]. This observation is based on 11 events with 71.7kg $\cdot$ years exposure, that gives a $T^{0\nu}_{1/2} = 1.19 \times 10^{25}$ years [30].

1.2.4 The Gotthard experiment

Half-life limits have been placed on a number of isotopes that potentially undergo $0\nu\beta\beta$ [31]. The best limit on ^{136}Xe is currently held by a gas phase experiment run at the Gotthard Underground Laboratory. The detector was a 180 liter (70 cm diameter, 75 cm long) time projection chamber (TPC) containing 5 bar of 62.5% isotopically enriched xenon gas. That amounts to 1.5×10^{25} ^{136}Xe atoms [32]. A TPC detector was used because it gives the ability to reconstruct the ionizing particle tracks of the two electrons generated in double-beta decay. Double beta decay events with two electron tracks with a common origin had a distinct signature, allowing significant reduction of background events.

The detector recorded ionization tracks created in an event by drifting freed electrons in the volume with an electric field (970 volts/cm) to the readout wires, shown in Fig. 1.5. A grounded grid shielded the detection wires from induction signals behind it. The "sense" wires 3.5 mm behind the grid at +2600 volts pulled the electrons through the grid. This large electric field amplified the signal by accelerating the initial electrons, creating a factor of 10^3 to 10^4 more ionization. The amplified charge induced signal on an X-Y readout plane behind the wires with 168 channels in each di-

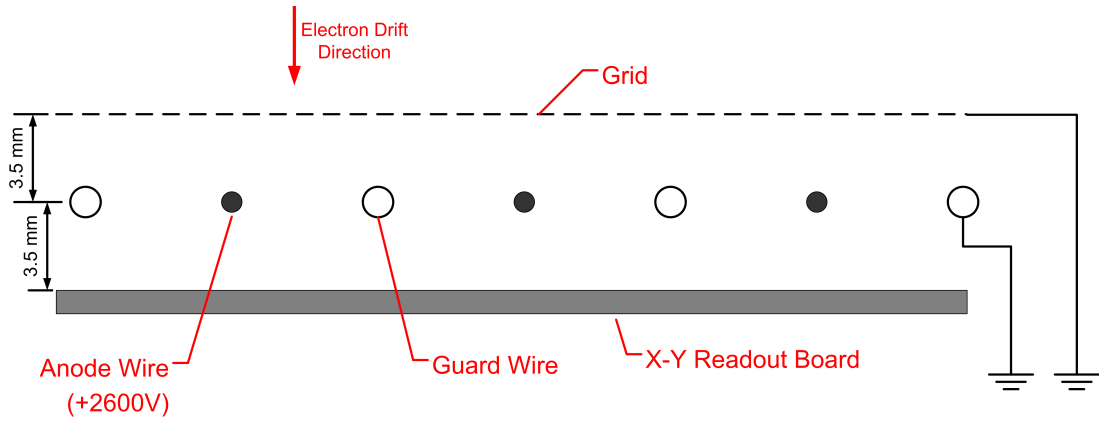

Figure 1.5: Readout system used in the TPC for the Gotthard xenon experiment. Ionization drifts past the grid, pulled through by the potential on the anode wires. Ionization was multiplied in this high field region, then collected on the anode wires and measured with a charge sensitive preamp. Induced signals were also recorded on 168 channels of each X and Y wire pads etched on the readout board. Replicated from [33].

rection. The total charge was collected on all of the sense wires which were connected to a single charge sensitive preamp. Guard wires between each sense wire served to ensure X-Y induction signals were only detected on channels directly below the charge location. Both X-Y and charge signals were recorded as a function of time. Using the drift time in the large chamber and the recorded signals, 3-dimensional tracks could be reconstructed.

The Gotthard ^{136}Xe experiment had two substantial runs (>6000 hours each) with a significant hardware upgrade between them. With the combined results, a limit of 4.4×10^{23} years for the neutrinoless double beta decay mode in ^{136}Xe was derived. This corresponds to an effective Majorana neutrino mass of <2-5 eV depending on the nuclear matrix model used [32]. A weak point for the the experiment was its small usable fiducial volume. This was because in the gas track lengths are long and only

about 30% of the TPC volume could completely contain an entire $0\nu\beta\beta$ event [34] according to their Monte Carlo simulations.

1.3 EXO-200 experiment

The EXO-200 detector located at the Waste Isolation Pilot Plant in New Mexico has been built to test the technology for a larger ultra-low background liquid phase TPC, as well as to search for the Majorana neutrino mass down to around 110 meV. Since the experiment is operated in the liquid phase, additional cooling infrastructure is needed, but the benefit is a compact detector with a large mass. The setup is shown in Fig. 1.6. The xenon is enriched to 80% in ^{136}Xe , giving EXO-200 about 50 times more ^{136}Xe isotope then the Gotthard xenon experiment in a smaller volume. The EXO-200 TPC is approximately 42 cm in diameter and 42 cm long.

The detector is a split TPC with the cathode at the center of the cylinder, and two independent anodes/readout planes. One half of the detector is shown in Fig. 1.7. The maximum drift distance, from the cathode to the first set of detection wires, is approximately 19 cm. Charge signals created by ionizing events are detected on two sets of wires, called U and V wires, set at 60 degrees with respect to each other, and recorded as a function of time. There are 38 individually readout U and V wires in each detector half. As the electrons drift to the anode they induce signal on the first set of wires, the V-wires, set at a lower negative potential with respect to the cathode. The second set of wires at ground, draw the electrons past the V wires using a larger drift field and collect the electrons. Combining the U and V wires signals with the APD signal, a 3-dimensional event position can be calculated knowing the electron drift velocity.

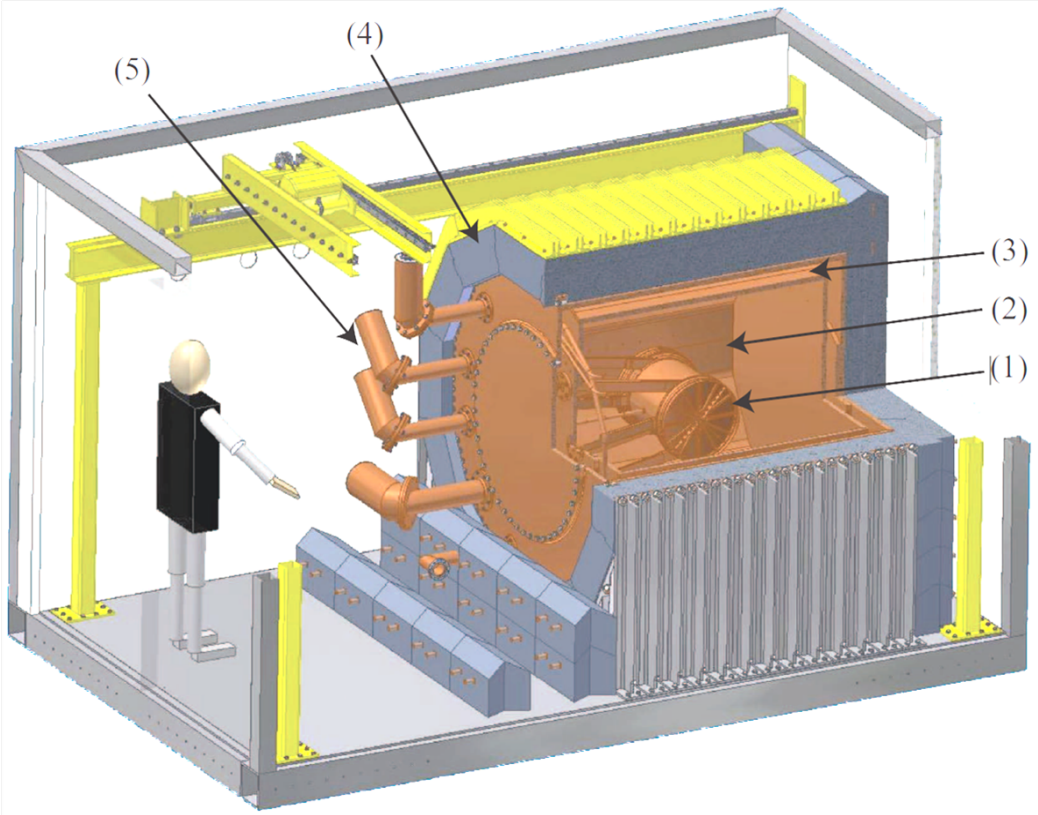

Figure 1.6: EXO-200 infrastructure for cooling and shielding the TPC. (1) TPC at approx. 40cm diameter. (2) HFE liquid conducts heat away from the TPC to large heat exchangers on (3) the inner cryostat. A vacuum space insulates the cold inner cryostat from the outer cryostat. (4) Lead shielding surrounds the detector to reduce radioactive backgrounds. (5) Feedthrough ports for signal wires, high voltage, xenon, and HFE inside the closed cryostat.

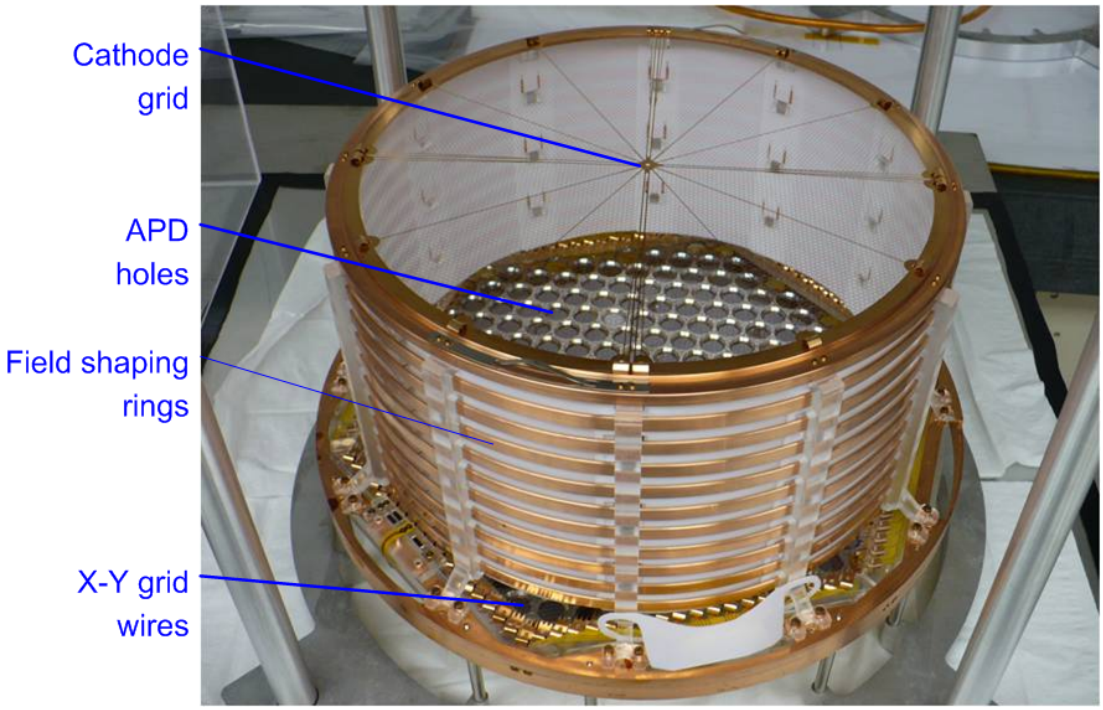

Figure 1.7: Half of the EXO-200 TPC during construction. Cathode grid is common to both halves of the TPC. APD plane is shown without APD's installed, which are arranged behind the grid wires. U-V grid wires cross 60-degrees with respect to each other. The V wires are set at a slightly negative potential, and U wires are grounded. The electrons are drawn through the V wires by the larger field between U and V wires. Electrons are drifted by the V wires which induce signal, and are collected on the U wires.

Avalanche photo diodes (APDs) are placed behind the grid wires to record the scintillation signal from the decay; this gives the initial event time. Scintillation light originates from energy deposited by the ionizing particles in the liquid xenon, sometimes resulting in excited rather than fully ionized xenon [35]. This gives EXO-200 the ability to determine an absolute Z-position, which is useful for locating the daughter ^{136}Ba for tagging. APDs also provide complimentary information on the decay energy by measuring the energy in scintillation [35], improving the total energy resolution.

Table 1.1: EXO-200 predicted sensitivity.

Mass (ton)	Eff. (%)	Run time (yr)	σ/E @ 2.5MeV (%)	Radioactive bkg. (events)	$T^{0\nu}_{1/2}$, 90% C.I. (yr)	Majorana mass (meV)	
						RQRPA	NSM
0.2	70	2	1.6	40	6.4×10^{25}	109	135

Track lengths in liquid are significantly shorter than in gas, so EXO-200 cannot resolve tracks. It relies on energy resolution for background rejection, and ultra low radioactivity parts to reduce backgrounds in the region of interest. Every part in or near the detector has been screened for radioactivity to meet stringent background goals [36]. EXO-200 projections are shown in Table 1.1. EXO-200 is currently running with 200kg of enriched ^{136}Xe. After two years it is expected to have a sensitivity to a Majorana mass of around 110 meV (depending on the nuclear matrix elements), shown in Table 1.1.

1.4 EXO

EXO is a proposed larger scale (1-10 ton) ^{136}Xe $0\nu\beta\beta$ search. Active barium tagging is being developed for EXO as an additional background rejection tool. Currently in the research phase, options for tagging are still being explored by several collaborators, taking many different forms. Schematics of four of these methods, which are discussed in more detail below, are shown in Fig. 1.8.

Detection of barium directly in the liquid (in-situ) is a simple approach being explored (Fig. 1.8A). In this technique laser light would be directed to the reconstructed position of a $0\nu\beta\beta$ candidate. There the barium would be detected by observing its

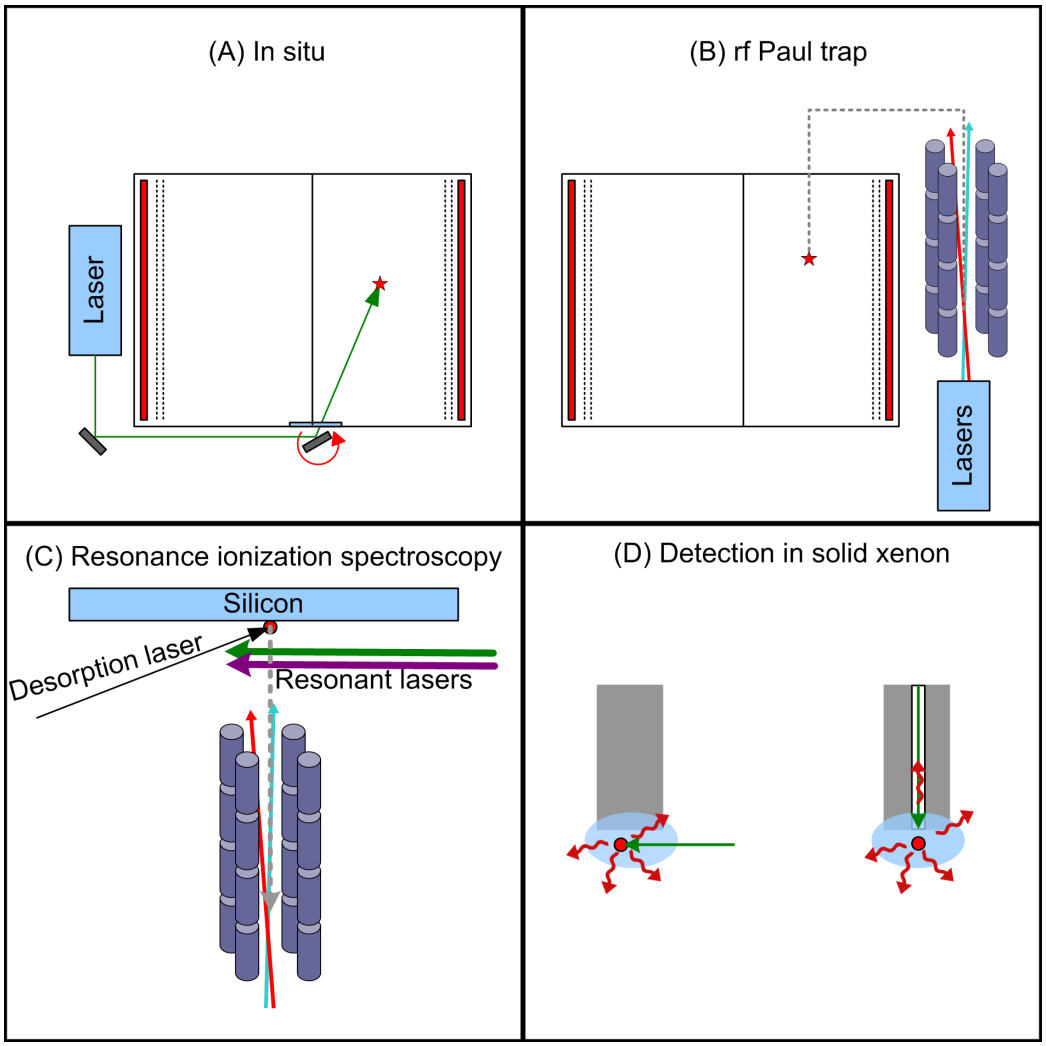

Figure 1.8: Tagging schema being explored for EXO. (A) Direct tagging in the liquid TPC. (B) Cryogenic grabber probe to place in RF Paul trap where detection in vacuum conditions can be done. (C) A grabber probe technique that does not use solid xenon, but desorbes the neutralized atom off the grabber probe and ionizes it so that is can be trapped in the RF Paul trap. (D) Detection of the ion or atom in solid xenon directly on the cryogenic grabber probe. Options are to scan the tip with lasers, or to use a fiber optic in the probe to provide excitation light and collect fluorescence.

characteristic fluorescence. This technique is still being explored, and work is ongoing to characterize barium fluorescence in liquid xenon.

The grab and trap method (Fig. 1.8B) would have a probe to grab the barium daughter inside the TPC and then release it in a quadrapole linear RF Paul trap. In research on this technique, detection of single barium ions (Ba^+) in a low pressure (8×10^{-5} to 4×10^{-3}) buffer gas by laser induced fluorescence has been demonstrated [37]. While the technique for single ion detection works well, getting the barium into the trap from a liquid TPC is non-trivial. A cryogenic probe has been investigated for the purpose of freezing and transporting the decay site, with barium ion, in xenon ice to the trap [38]. Releasing the barium ion from ice into a Paul trap has not been demonstrated.

Resonance ionization spectroscopy (Fig. 1.8C) would use a solid grabber probe which could pull the barium-ion to its surface where it would attach (no ice). The probe could then be removed from the liquid xenon and placed into the RF Paul trap in vacuum. To release the barium, which is likely neutralized on the probe, a desorption laser is used. Two additional lasers can then be used to resonantly ionize the barium atom, the first laser exciting the atom to the $6s6p\ ^1P_1$ state (553.5 nm), and the next laser (389.7 nm) excites to a higher resonant state, which auto-ionizes. Using resonance ionization allows for selective and efficient ionization of the atoms. The barium ion, now singly ionized, can be trapped and detected in the RF Paul trap. This is similar to the technique in Fig. 1.8B, except the transport does not require using xenon ice to preserve the ionization. This technique has successfully demonstrated release of barium atoms deposited on a silicon target as ions.

Detection of barium in solid xenon on a cryogenic probe (Fig. 1.8D) is an appealing technique for EXO. By freezing the barium daughter ion in solid xenon it can be kept

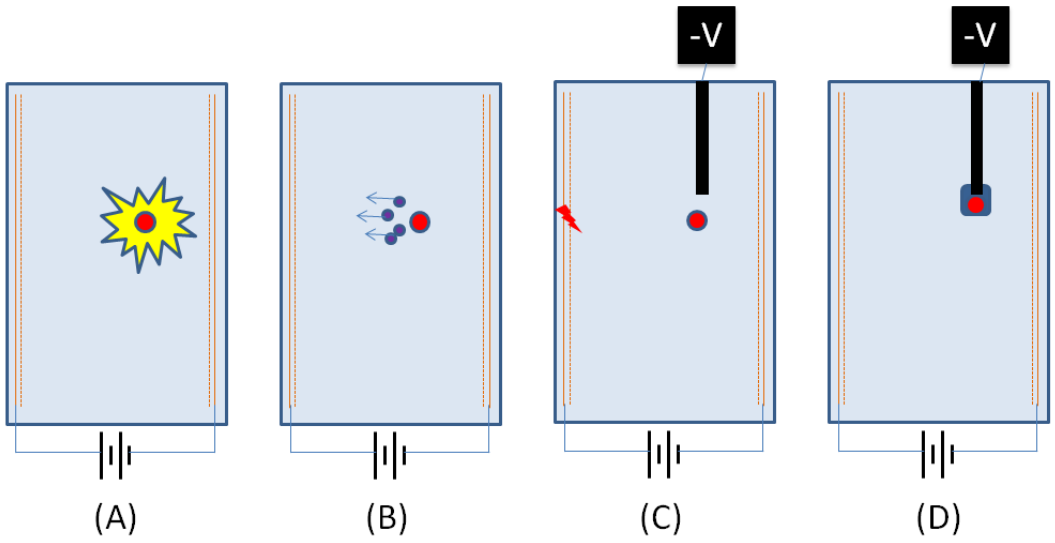

Figure 1.9: Possible detection scheme for EXO using a cryogenic probe to grab the candidate event. (A) A candidate double beta decay triggers the detector's APDs with scintillation light. (B) Ionization from the decay drifts to the readout plane and the detector reconstructs the position of the barium daughter. (C) Cryogenic probe either moves to the barium position, or a potential pulls the ion to the probe tip. (D) The cryogenic probe cools the tip freezing the barium in solid xenon trapping it for spectroscopic study.

as long as necessary to make an identification. The barium is not lost in the process of detection. If it were desired, then the barium ion could in principle be released into a RF Paul trap or some other detector after tagging in the xenon ice. The concept for detecting and grabbing a candidate event in solid xenon is shown in Fig. 1.9. When a candidate event is detected in the TPC, the position of the event is reconstructed. A cryogenic probe is then deployed into the detector to the site. There a pulse of cooling of the probe freezes the barium daughter in some xenon. The probe can then be removed from the TPC where it can be cooled further, then scanned for the barium candidate using fluorescence spectroscopy. The detection of single barium atoms in solid xenon is the focus of this dissertation.

Table 1.2: EXO proposed experimental sensitivity.

Case	**Mass (ton)**	**Eff. (%)**	**Run time (yr)**	**σ/E @ 2.5MeV (%)**	**$2\nu\beta\beta$ bkg. (events)**	**$T^{0\nu}_{1/2}$, 90% C.I. (yr)**	**Majorana mass (meV)**	
							RQRPA	**NSM**
Cons.	1	70	5	1.6	0.5 ($\rightarrow$ 1)	2×10^{27}	19	24
Aggr.	10	70	10	1	0.7 ($\rightarrow$ 1)	4.1×10^{28}	4.3	5.3

All of these techniques require the ability to locate the daughter barium ion/atom in the TPC. A liquid xenon TPC, such as EXO-200, can reconstruct the event location for a $\beta\beta$ decay to a few millimeters. If the barium daughter remains singly ionized, its velocity is known, as the mobility of barium ions in liquid xenon has already been studied under the influence of an electric field [39]. Location of the drifting ion with millimeter accuracy for the placement of the probe is possible. If the barium neutralizes instantly the atom will not diffuse significantly before a grabber probe is deployed, and the atom will be found at the original decay site.

With barium tagging EXO has the potential to measure absolute neutrino masses to around 5 meV. The proposed experimental parameters for EXO are shown in Table 1.2 with expected sensitivities. With tagging the only background for EXO would be $2\nu\beta\beta$ decays near the $0\nu\beta\beta$ endpoint.

Chapter 2

Background

Information relevant to the detection of a single barium atom in solid xenon is reviewed in this chapter. First the energy levels of barium atoms in vacuum, without complications from a solid xenon host, are reviewed. Then spectroscopy of atoms in solid hosts is briefly discussed. This field is called matrix isolation spectroscopy, and spectra for many Group-I and Group-II atoms in solid noble gas hosts have been published. Single molecule detection techniques are then reviewed as a starting point for detection of a single barium atom. In the last section a tagging method based on a single mode fiber optic is introduced. Optical properties of dye molecules and quantum dots, which were used to test the fiber detector, are introduced and compared to barium atoms.

2.1 Neutral Barium Energy Levels

The lowest lying atomic energy levels for neutral barium in vacuum [40] are shown in Figure 2.1. The strongest excitation out of the ground state is with 553.7 nm

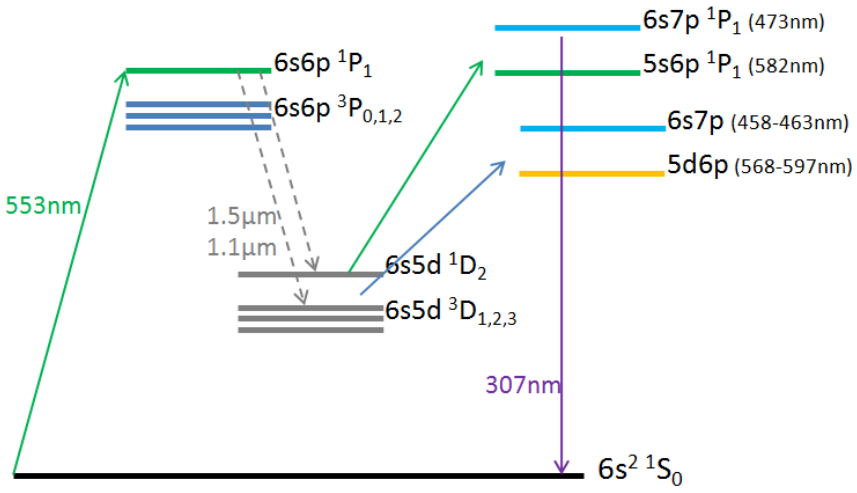

Figure 2.1: Energy level diagram of the lowest lying states for neutral barium. Main excitation out of the ground state is with 553 nm. Additional excitations are also shown out of the D states which may be seen with visible laser wavelengths.

(18060.261 cm^{-1}). Excited barium atoms usually decay back to the ground state ($6s6p\ ^1P_1 \rightarrow 6s^2\ ^1S_0$) by emission of a photon. Occasionally however, barium atoms will decay to the metastable D states ($6s6p\ ^1P_1 \rightarrow 6s5d$). These states are metastable because the parity selection rule forbids them to decay back to the ground state[1]. This is a problem for sensitive fluorescence detection because an atom in a metastable state will no longer respond to excitation. This process, referred to as optical pumping, causes the fluorescence signal of many atoms to decrease with continued excitation as atoms get stuck in metastable states. In some simple atomic systems this can be remedied with an additional excitation wavelength that excites atoms out of the metastable state to states that can decay back to the ground state (for example in Ba^+ [37]). One potential pathway for neutral barium out of the metastable state

[1]Parity selection rule states that the atom's wavefunction must change: even↔odd. This rule can be broken but the lifetime is long compared to an allowed transition

($6s5d\ ^1D_2 \rightarrow 6s7p\ ^1P_1$) can return the atom back to the ground state with a 307 nm emission, although not 100% of the time.

The probability that an excited barium atom ($6s6s\ ^1P_1$) decays to a metastable state is referred to as the branching-ratio. This branching-ratio was measured by several different researchers, a few of which are reported in Table 2.1. The average

Table 2.1: Barium branching ratios for transitions out of the $6s6p\ ^1P_1$ state.

Transition	Ref [41]	Ref [42]	Ref [43]	Ref [44]
$6s6p\ ^1P_1 \rightarrow 6s^2\ ^1S_0$		0.9966(0.2)		
$6s6p\ ^1P_1 \rightarrow 6s5d\ ^1D_2$		0.0025(15)	.0023(2)	0.00206(17)
$6s6p\ ^1P_1 \rightarrow 6s5d\ ^3D_2$		0.0009(25)		
$6s6p\ ^1P_1 \rightarrow 6s5d\ ^3D_1$		< 0.00008		
$6s6p\ ^1P_1 \rightarrow 6s5d\ \sum$	0.00354(4)			

number of absorptions by a barium atom before it decays to the metastable D state (optically pumped) is given by:

$$\mu = \frac{1-p}{p} \tag{2.1}$$

where p is the branching ratio into the metastable states [45]. For $p = 0.0034$ this corresponds to 293 cycles on average in vacuum.

Single barium atoms in vacuum have been successfully detected by exciting with 553.7 nm and observing fluorescence back to the ground state using photon-burst technique [46]. Lewis et al. created a beam of barium atoms in vacuum that pass through a perpendicular 554 nm laser beam, exciting them ($6s^2\ ^1S_0 \rightarrow 6s6p\ ^1P_1$) and detecting the fluorescence photons. Their total fluorescence yield was limited by the interaction time of the atoms in the laser, and not by optical pumping. With 5% photon detection efficiency, single barium atoms were successfully detected using a single laser wavelength in vacuum.

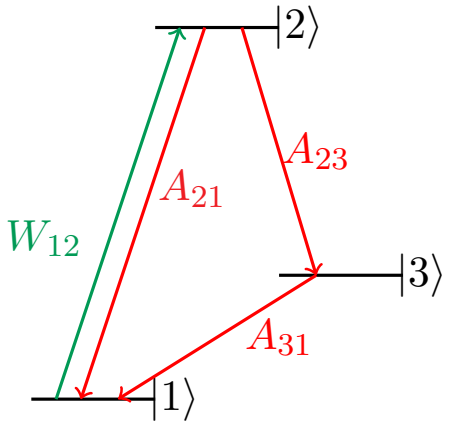

Figure 2.2: Three state model for neutral barium.

2.1.1 Multi-Level System Model

A simple three state model of the barium energy transitions has been worked out to quantitatively understand time and intensity dependence of the fluorescence yield using a single excitation wavelength for the $6s^2\ {}^1S_0 \rightarrow 6s6p\ {}^1P_1$ transition. The system from Fig. 2.1 is considered in a simplified form, shown in Fig. 2.2 where the states are labeled numerically, N_1, N_2, and N_3. The rate equations for the three state system are:

$$\frac{dN_1}{dt} = -W_{12}N_1 + A_{21}N_2 + A_{31}N_3 \ , \tag{2.2}$$

$$\frac{dN_2}{dt} = W_{12}N_1 - A_{21}N_2 - A_{23}N_2 \ , \tag{2.3}$$

$$\frac{dN_3}{dt} = A_{23}N_2 - A_{31}N_3 \ , \tag{2.4}$$

$$N_{total} = N_1 + N_2 + N_3 \ , \tag{2.5}$$

$$\frac{dN_{total}}{dt} = 0 \ , \tag{2.6}$$

where W_{12} is the $6s^2\ {}^1S_0 \rightarrow 6s6p\ {}^1P_1$ excitation rate, and A_{ij} is the rate that an atom in state i decays to state j. This system can be solved by either substituting equations to get a second order non-homogeneous equation in terms of only one state (like N_2), or equivalently, by solving the system using an eigenvalue technique. The solution has the form

$$N_2(t) = \alpha_1 e^{r_1 t} + \alpha_2 e^{r_2 t} + \beta \tag{2.7}$$

where

$$r_1 = -\frac{\mathrm{A_{21}}}{2} - \frac{\mathrm{A_{23}}}{2} - \frac{\mathrm{A_{31}}}{2} - \frac{\mathrm{W_{12}}}{2} - \frac{\sqrt{\mathrm{A_{21}}^2 + 2\,\mathrm{A_{21}}\,\mathrm{A_{23}} - 2\,\mathrm{A_{21}}\,\mathrm{A_{31}} + 2\,\mathrm{A_{21}}\,\mathrm{W_{12}} + \mathrm{A_{23}}^2 - 2\,\mathrm{A_{23}}\,\mathrm{A_{31}} - 2\,\mathrm{A_{23}}\,\mathrm{W_{12}} + \mathrm{A_{31}}^2 - 2\,\mathrm{A_{31}}\,\mathrm{W_{12}} + \mathrm{W_{12}}^2}}{2}\,, \tag{2.8}$$

$$r_2 = \frac{\sqrt{\mathrm{A_{21}}^2 + 2\,\mathrm{A_{21}}\,\mathrm{A_{23}} - 2\,\mathrm{A_{21}}\,\mathrm{A_{31}} + 2\,\mathrm{A_{21}}\,\mathrm{W_{12}} + \mathrm{A_{23}}^2 - 2\,\mathrm{A_{23}}\,\mathrm{A_{31}} - 2\,\mathrm{A_{23}}\,\mathrm{W_{12}} + \mathrm{A_{31}}^2 - 2\,\mathrm{A_{31}}\,\mathrm{W_{12}} + \mathrm{W_{12}}^2}}{2} - \frac{\mathrm{A_{23}}}{2} - \frac{\mathrm{A_{31}}}{2} - \frac{\mathrm{W_{12}}}{2} - \frac{\mathrm{A_{21}}}{2}\,, \tag{2.9}$$

β is the particular solution, and α_1 and α_2 are constants that solve the initial conditions. The particular solution, in this case just a constant, is the steady state solution:

$$\beta = \frac{N_{total} W_{12} A_{31}}{W_{12}A_{23} + A_{31}A_{21} + A_{31}A_{23} + W_{12}A_{31}}. \tag{2.10}$$

The constants α_1 and α_2 are found with the initial conditions

$$N_2(0) = 0\,, \tag{2.11}$$

and

$$\frac{dN_2(0)}{dt} = W_{12} N_{total}\,, \tag{2.12}$$

giving

$$\alpha_1 = \left(\frac{W_{12} N_{total}}{r_2} + \frac{N_{total} R_{12} A_{31}}{W_{12} A_{23} + A_{31} A_{21} + A_{31} A_{23} + W_{12} A_{31}} \right) \left(\frac{1}{\frac{r_1}{r_2} - 1} \right) \tag{2.13}$$

and

$$\alpha_2 = \frac{W_{12} N_{total} - \alpha_1 r_1}{r_2} \, . \tag{2.14}$$

These equations describe the time dependence of the excited state population as a function of time, which is proportional to the fluorescence rate. The exponential term with r_1 describes the rapid initial rise in N_2 due to excitation when all the atoms start in the ground state. The second exponential term describes the gradual in loss of atoms to N_3, and the offset β describes the steady state condition.

The decay rate from the metastable states to the ground state (modeled as A_{31}) is unknown for barium in solid xenon. If the decay out of the metastable states is much slower than rate into them, then the fluorescence rate decreases with time, which is referred to as optical pumping. This is shown in Fig. 2.3 for several excitation rates, W_{12}, and metastable-decay rates, A_{31}. Taking an extreme case, if $A_{31} = 0$ then N_2 eventually reaches zero as all of the atoms become stuck in N_3. Conversely, if $A_{31} \sim W_{12}$ then the fluorescence rate is dominated by the pumping rate alone, and $N_2 \approx W_{12}/A_{21}$.

If a single atom were being observed, the fluorescence would stop when the atom branched into the metastable state, until it eventually decays back to the ground state, assuming $A_{31} > 0$. Determining A_{31} is therefore important to decide how to move forward to single atom detection. If A_{31} is very small, then efficient detection

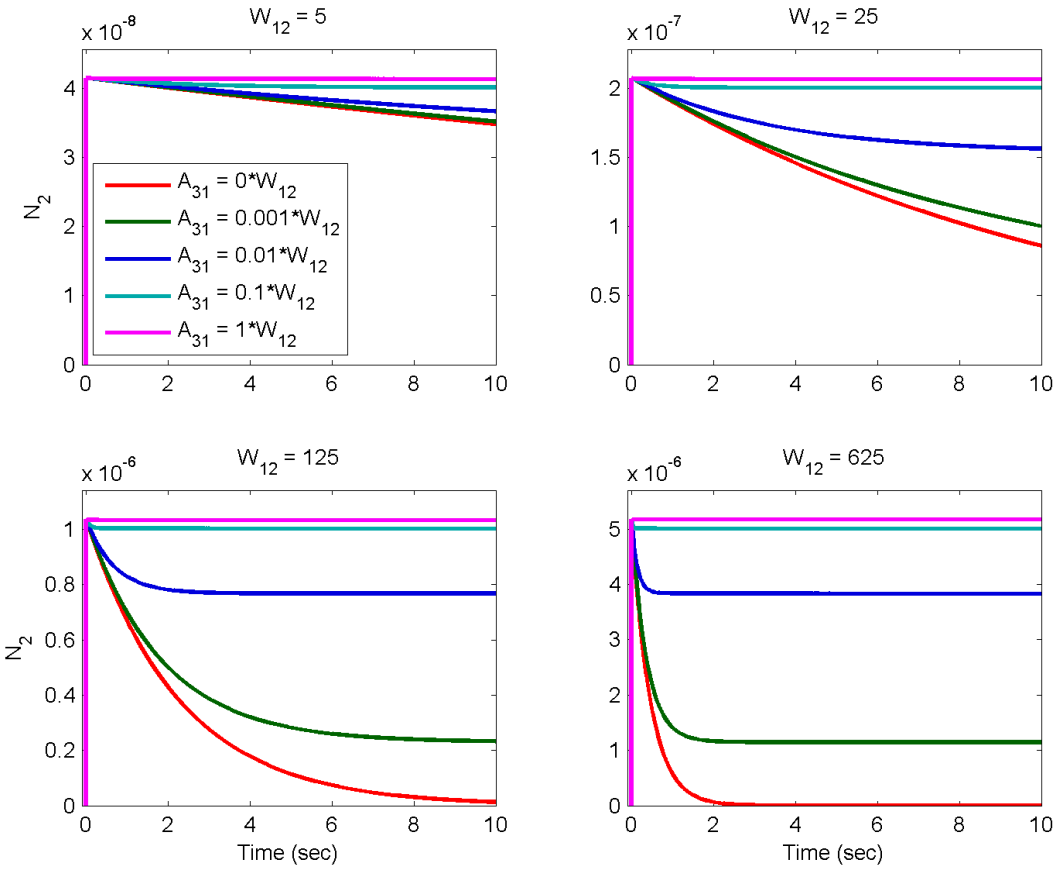

Figure 2.3: Three level optical pumping model solved for the number of atoms in the excited state as a function of time, $N_2(t)$. Each frame represents a different pumping strength W_{12}, and each line represents a different decay rate (A_{31}) out of the metastable N_3 state (relative to the pumping rate). The relationship of A_{31} to W_{12} is shown in the top right frame, and is consistent in all frames. As atoms are trapped in the metastable state the number of atoms in the excited state decreases with time, as will the fluorescence. Plotted using $A_{31} = 1.2 \times 10^8 \text{sec}^{-1}$, $A_{23} = A_{21} \times 0.00354$, and $N_{total} = 1$.

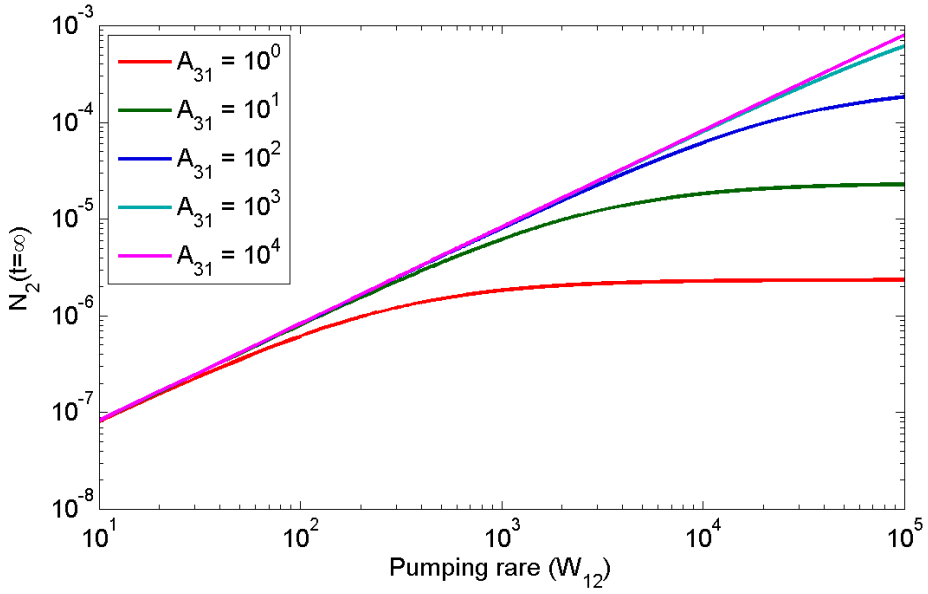

Figure 2.4: Effects of optical pumping on fluorescence in steady state as a function of pumping rate. Plotted using $A_{31} = 1.2 \times 10^8 \text{sec}^{-1}$, $A_{23} = A_{21} \times 0.00354$, and $N_{total} = 1$.

or some form of active repumping of the atoms from the metastable state may be necessary.

One way to measure A_{31} is to use the steady state solution Eq. 2.10, shown more directly as a function of the pumping rate W_{12} and A_{31}

$$N_2^{SS} = \frac{N A_{31} W_{12}}{W_{12} + A_{31}} \left(A_{21} + A_{23} - \frac{W_{12}(A_{21} - A_{31})}{W_{12} + A_{31}} \right)^{-1}. \tag{2.15}$$

N_2^{SS} for several values of A_{31} are plotted as a function of the pumping rate in Fig. 2.4. By measuring the fluorescence rate for several laser intensities, A_{31} may be determined. The steady state fluorescence rate increases linearly with W_{12} and then begins to turn over when $W_{12} \sim 10 A_{31}$. A_{31} can be smaller than W_{12} since only about 1 in 300 excitations results in a decay to the metastable state.

Table 2.2: Properties of solid xenon and argon (from [49]).

	Xenon	Argon
Vapor Pressure = 10^{-7} torr	54.2 K	28.6 K
Vapor Pressure = 10^{-5} torr	62.7 K	33.1 K
Lattice Parameter @ 10 K	0.6132 nm	0.5312 nm
Density @ 10 K (g/cm^3)	3.780	1.765

2.2 Matrix isolation spectroscopy

Matrix isolation spectroscopy is a technique whereby a guest species, frozen in a weakly interacting host, can be studied in lieu of studies of its free counterpart, while maintaining similar spectral properties. Matrix isolation was first coined by Pimentel et al. in 1954 [47] where they described the technique to study short lived unstable species by freezing them in a matrix, preventing further reactions [48]. Since then, matrix isolation has found numerous uses (arguably the most exotic application would be in a tagging schema for a $0\nu\beta\beta$ search!).

The use of noble gases as the host in matrix isolation is quite common due to their low reactivity and transparency in the visible range when solid. Noble gases require cryogenic temperatures to be rigid solids suitable as a host. It is suggested that matrix isolation experiments should be performed at less than 0.6 times the vaporization temperature to reduce diffusion of the guest inside the solid [49]. Xenon and argon vapor pressures and other properties of its solid form can be found in Table 2.2.

To highlight a few points covered in detail in B. Meyer's review book on the subject [49], understanding how a solid matrix influences spectra of isolated guests is useful for interpretation of results. High concentrations of the guest to host can

influence spectral properties. This will not be an issue for tagging but may be for initial studies of concentrated samples. Concentrations of 1:1000 guest to host are generally sufficiently isolated to represent individual atoms with minimal guest-guest interactions. The matrix alone can cause spectral shifts, which can be either to shorter or longer wavelengths depending on the interactions involved. For the most part, noble gas matricies of higher polarizability cause greater red-shifts. Structure of individual resonance lines can also be observed in matrix isolated species, often in a triplet. This is caused by degeneracy of the excited P state being split by interactions with the neighboring atoms. Local structure can also produce different spectral shifts due to non-equivalent arrangements between neighboring atoms of the host matrix, referred to as sites. Deposition conditions can greatly influence the spectra observed by changing the proportion of guests in particular sites. Slower depositions are noted as having more varying sites [49]. Sites also have dramatic effects that can be observed by annealing the matrix, which give less stable sites the opportunity to convert to more stable sites. Spin forbidden transitions can become more significant inside a heavy solid host, this is known as the external heavy atom effect [50]. Non-radiative decay are also allowed by interactions with the matrix, with multiple potential explanations from phonon coupling, spin conversion, and internal conversion. These theories are not discussed in this work, other than to acknowledge they exist and could present a problem. In short there are many possibilities that can create complications in the interpretation of spectra of matrix isolated atoms.

The emission and absorption spectra of matrix isolated barium in solid argon and krypton have been measured by Balling and Wright[51] at 10 K, and are shown in Figure 2.5. The $6s^2\ {}^1S_0 \rightarrow 6s6p\ {}^1P_1$ absorption of both spectra are blue shifted and broadened, with argon having the largest shift to 513 nm (from 554 nm). This

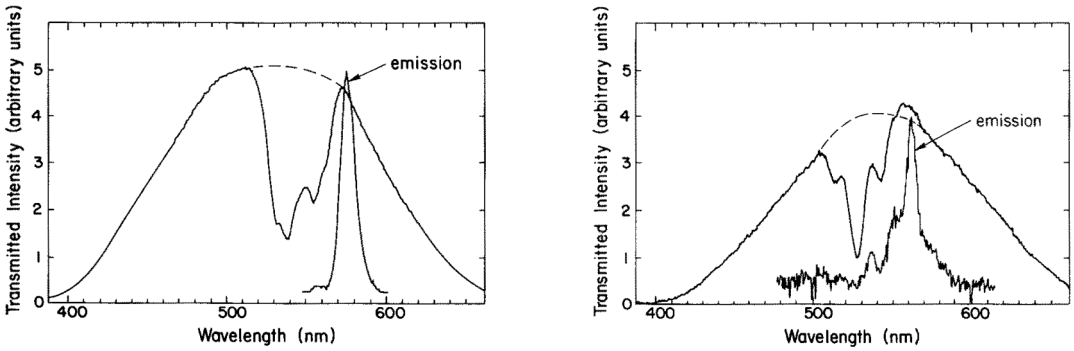

Figure 2.5: White light absorption bands and N_2 laser induced emission associated Ba in Kr (left) and Ba in Ar (right). Reprinted with permission from L. Balling and J. Wright. Absorption and emission spectra of matrix-isolated Ba atoms. The Journal of chemical physics, 83(5) 2614, 1985. Copyright 1985, American Institute of Physics.

Table 2.3: Absorption and emission wavelengths from [51] for argon and xenon matrices.

	Argon	Krypton	Xenon
Absorption (nm)	513	531	553
	527	538	556
	542	555	573
Emission (nm)	536	582	
	568		

shift is caused by interactions of the barium energy levels with the matrix. Multiple absorption peaks are seen. Balling and Wright reported barium in solid xenon was too unstable to acquire an absorption trace or any fluorescence spectra; however absorption peaks were identified. Fluorescence measurements were performed with a 337 nm N_2 laser which excites higher energy levels that decay, finally resulting in the emission of a photon on the $6s6p\ ^1P_1 \rightarrow 6s^2\ ^1S_0$ transition. The peak locations for all three hosts is summarized in Table 2.3. The peaks move to the red with heavier hosts, an example of the effect of increased polarizability for those species.

2.3 Single atom detection

Detection of single fluorescent molecules in a condensed phase sample is now common practice with sensitive spectroscopic techniques, and several systems have been studied [52, 53]. The advantage of single molecule spectroscopy is that information is directly gathered from the individual molecule without complicating the observation by studying the average. Differences in spectra of individual molecules can, for example, be due to the local environment or species heterogeneity.

One technique that was reviewed in [53] is a candidate for barium tagging. Called confocal microscopy, it uses a high numerical aperture (NA) microscope objective to focus the excitation light onto the sample as well as to collect fluorescence light, this is shown in Fig. 2.6. A dichroic filter is used to reflect laser light into the objective focused on the sample. Some of the fluorescence and scattered laser light are collected by the objective and collimated. The dichroic filter transmits the red-shifted fluorescence, while blocking the scattered light at the laser wavelength. The fluorescence then goes through additional laser blocking filters and a spatial filter before it is measured. The spatial filter serves to reduce the depth of field that is being observed in the sample. This limits the volume that is being observed, reducing fluorescence contribution from impurities in the sample, and Raman scattering from the host, which helps reduce the overall background.

High NA objectives are ideal because they collect fluorescence light from a large solid angle

$$NA = n \sin\theta \tag{2.16}$$

with θ's that can approach nearly 70 degrees! The collection efficiency of such a system can be calculated, assuming an isotropic emission source. The fraction of

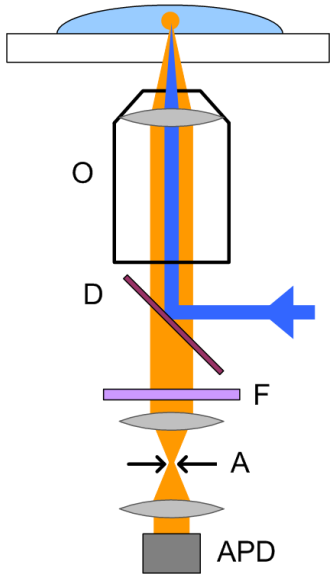

Figure 2.6: Confocal microscopy setup for single molecule spectroscopy. (O) Objective, (D) dichroic filter, (F) laser blocking filter, (A) aperture.

light gathered by the objective is

$$\left(\frac{1}{4\pi}\right)\int_0^{2\pi}\int_0^{\sin^{-1}(NA/n)} \sin\theta\, d\theta\, d\phi = \frac{1}{2}\left(1-\cos\left(\sin^{-1}\left(NA/n\right)\right)\right) \ . \tag{2.17}$$

The focus spot size of the excitation region is diffraction limited ($d \approx \frac{\lambda}{2 \cdot NA}$). A small focus reduces the backgrounds, while providing the most excitation intensity to the atom where it is useful.

2.3.1 Rhodamine 6G and quantum dots

Rhodamine 6G is a popular laser dye with a large absorption cross section used for its strong fluorescing characteristics. In this work Rhodamine 6G was used to study the sensitivity of a fiber optic probe detector, which might be used for detecting single barium atoms in solid xenon. Rhodamine 6G is an appropriate choice for a

Table 2.4: Rhodamine 6G properties in solution, from [54].

Property	Methanol	Ethylene glycol
Index of refraction	1.3288	1.4310
Peak absorption (nm)	530	535
Peak emission (nm)	556	562
Cross section (cm^2)	4.39×10^{-16}[55]	

test, as it has a somewhat similar absorption and fluoresce spectra, as well as similar absorption cross section, to barium in solid xenon. The dye was diluted in either ethylene glycol or methanol, depending on the particular experiment, to get down to the single molecule level in the detection volume. The properties of Rhodamine 6G in these solutions are given in Table 2.4.

Quantum dots are fluorescing nanocrystals which can also be used as barium analogues. They are a strong fluorescing species that can be manufactured to emit at any wavelength, simply by changing the physical size of the crystal. They differ from other fluorescent species in one remarkable way, however, which was why they are of interest for testing the sensitivity of the fiber probe. Quantum dots have a property know as blinking. They act like a normal fluorescing molecule with rapid transitions for a while, then stop responding suddenly for long time periods, on the order of a second [56]. Observation of this blinking would clearly demonstrate detection of a single dot, since individual dots blink independently. The long blinking periods are convenient for the detection system which has minimum 0.1 second exposure times.

Chapter 3

Apparatus methods and procedure

This chapter details the apparatus for performing spectroscopic measurements of barium neutrals in solid xenon and argon hosts that was constructed at CSU. The sample preparation system is broken up into three major parts and discussed in Section 3.1.1: the vacuum insulated cryostat, the host gas supply, and the barium source. The procedure for creating the matrix isolated barium is then discussed in Section 3.1.2. Section 3.2 covers the apparatus used for making spectroscopic measurements. Diagnostic measurements with a residual gas analyzer are discussed in Section 3.3. The last section details the setup for a fiber optic probe detector that was constructed and tested as a potential tagging method.

3.1 Matrix Isolated Barium

3.1.1 Apparatus

The matrix isolation setup is built around an Advanced Research Systems^{TM} two stage closed cycle helium cryostat that cools a small cold finger to 10 K with 0.1 watts

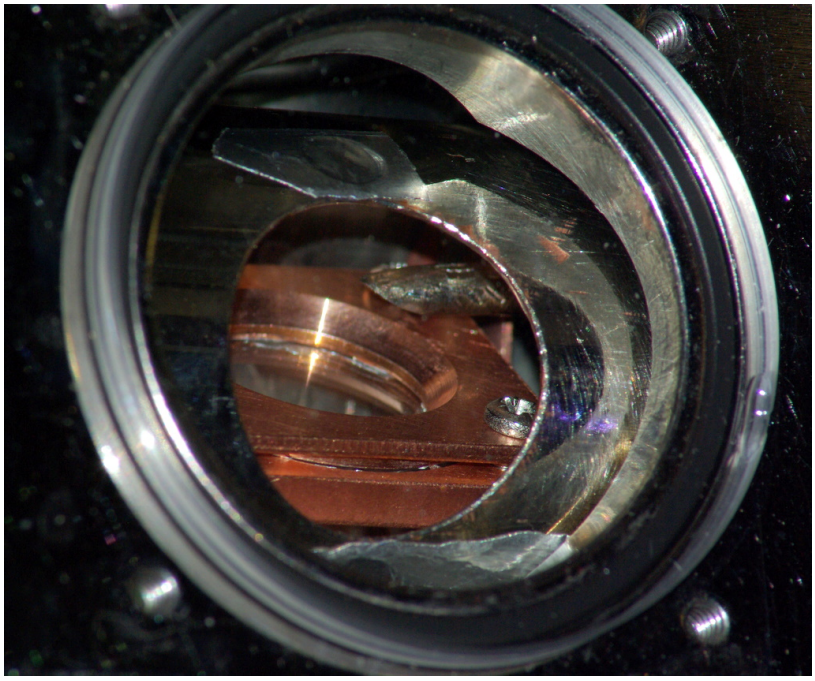

Figure 3.1: Cryostat cold finger with copper window holder. Sapphire plate and gas inlet are visible through the hole in the cold shield, all of which is inside the vacuum housing.

of cooling power. Attached to the cryo-finger is a copper window holder for a 19 millimeter diameter sapphire window, 0.5 millimeters thick. This is shown in Fig. 3.1 as seen through the viewport and cold shield access hole. The copper holder has 16 millimeter clear view at normal incidence, holding the window on its circumference with indium foil pads. The copper window holder is attached to the cold-finger with an indium foil gasket to increase surface area contact. The temperature of the cold finger is read out using a Gold-Chromille type thermocouple. A more accurate silicon diode temperature sensor was also installed for later experiments. A 15 watt band heater attached to the cold finger allows for sample heating, and is feedback controlled using the thermocouple temperature. Temperatures can be set anywhere from 10 K to 300 K.

Table 3.1: Heat load estimates by source on the second stage of the cryostat.

Heat Source	Power (milliwatts)
Shield Radiation at 77K	< 1
Radiation from holes in shield	30
Freezing of Xe	19

A radiation shield attached to the first stage of the cryostat ($\sim$ 77 K) covers much of the second stage to provide shielding from room temperature radiation. Holes in the radiation shield are necessary, however, for access to the sample window for gas inlet, barium deposition, and optical access. The heat load from the heat shield radiation and radiation through the holes in the shield was estimated to be 30 mW (Table 3.1), while the heat load of freezing xenon at nominal deposition rates (Leak=43) was about 19 mW.

The setup for delivery of the host gas and barium was modified several times in the evolution of the apparatus. Although data was gathered at several different stages of the modification, there have been two fundamental modes of operation. Initially the barium and host gas came through a short 1/4" O.D. feed through tube, connected to a barium getter housing (Fig. 3.2.A). Later the gas supply and the barium sources were separated to make the barium deposition path colinear with a barium ion beam (Fig. 3.2.B). This was done to directly compare their spectra and to test for neutralization of the ions in the matrix.

The gas supply system uses research-grade gas without further purification. The host gas pressure is reduced to 20 psig by regulator, and fed into a Granville-Phillips^{TM} series 203 leak valve. Leak rates for several valve settings were calibrated at this backing pressure by depositing gas on the cold sample window and measuring interference

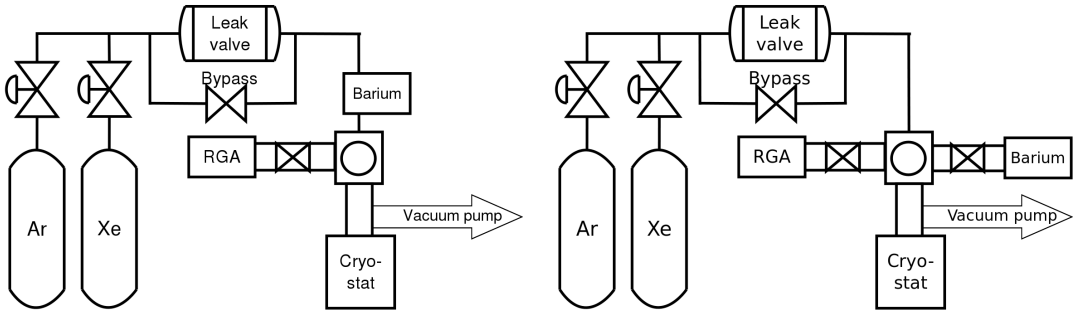

Figure 3.2: Barium and gas supply schematic for the cryostat. (A) early combined supply, (B) separated barium and gas supplies.

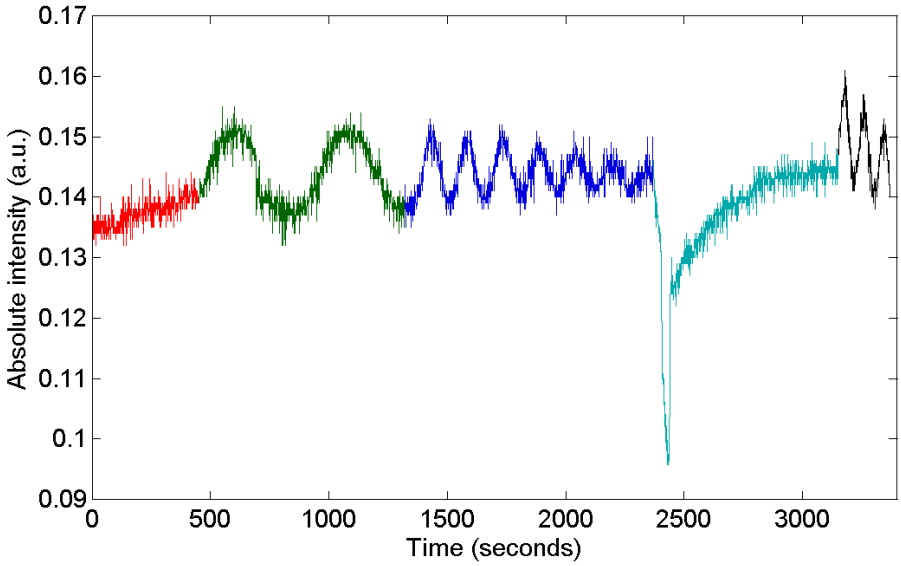

Figure 3.3: Interference fringes indicating xenon deposition growth for leak rates from left to right: 40 (red; no fringes), 41 (green; T_p = 466 sec), 42 (blue; T_p = 154 sec), evaporation of the sample using the heater(cyan), 43 (black; T_p = 83 sec). This was done with the separated configuration as shown in Fig. 3.2.B.

fringes of a laser beam passing through the growing sample. From the period of the fringes shown in Fig. 3.3, the growth rate of the matrix was determined for each leak setting.

The neutral barium source is a getter manufactured by SAES^{TM}. A common application for these getters is to deposit barium as a getter in vacuum tubes, such as television tubes. The series HU-13 getters used have a stainless steel U-channel ring filled with a barium alloy. These rings were cut in half (as show in Fig. 3.4) and connected in vacuum to a high current power supply. By Joule heating the barium in the alloy could be evaporated. The atoms spray from the U-channel onto anything that has line-of-sight to the channel opening, including the sample window. In the combined barium gas system (Fig. 3.2.A) the solid angle of the window at the getter was limited by the small aperture of the 1/4" tube connecting the getter housing to the cryostat shroud. Later when the getter was moved to the separate configuration (Fig. 3.2.B), the barium yield (in atoms/area) was greatly increased. The average current necessary to evaporate barium from the getter also changed, for some unknown reason, between configurations. In the combined configuration the getter was mounted with stainless steel tabs pinching the ends of the getter, and the average current was around 9 amps to release the barium. The new holder used all copper current carrying components, and the average current was around 14 amps[1]. Before cooling down the cryostat, the getters were sometimes run at a reduced current ($\sim 4\ A$) for a few minutes to bake out adsorbed water and gases so that they were not deposited with barium into the xenon matrix.

A barium ion source (Colutron^{TM}) was also used to deposit barium in the solid matrix. This source used solid barium samples which were heated by a filament, and ionized by a discharge. Ionized barium is pulled out of the source by an extraction field and mass selected with an $\vec{E} \times \vec{B}$ filter. While the source provides ions to

[1]It would seem the resistance of the getter length and power required to heat that length would only depend on the getter properties. Perhaps resistance at the connection between the stainless tabs and getter caused significant local heating.

Figure 3.4: Half of a SAES HU-13 barium after use. The darkened color was not there prior to use.

the sample, many neutralize, which for the purpose of this work is a perfectly good source of matrix isolated barium. Ionic barium spectra and neutralization studies are the subject of Shon Cook's Ph.D. thesis. Understanding the spectrum of neutral barium is important in that context for separating the fluorescence components due to neutralized barium atoms from those of matrix isolated barium ions.

3.1.2 Creating matrix isolated barium samples

Matrix preparation begins with cooling the sapphire window. During the hour long cool down process some molecules of background gases freeze onto the sample window. After the system is cooled, the heater on the coldfinger was used to warm up the sample window to 80 K, removing some of this contamination (N_2 in particular is suspected). The sample holder cools back down quickly. The host gas is then leaked into the cryostat to form a foundation for the matrix (as recommended in [49]). This foundation was typically deposited for 5 to 10 minutes at a leak rate setting of 43 ($\sim$ 3nm/s) before barium is deposited. Then the barium getter current is slowly

ramped up until barium begins to be emitted by the getter and deposited onto the sample window (the gas must continue to be deposited as well to isolate the barium). Barium yield could be tuned slightly by applying more or less current, and monitored by observing absorption and or fluorescence measurements. The getter would always visibly glow BrickRed when the getter would release barium. Finally, when the barium deposition is finished, the host gas is deposited for another 5 minutes to cap the matrix and then shut off. This cap serves to keep any additional background gas molecules freezing to the sample separated from the barium. Samples prepared in this way can be used for a few hours without having contamination problems. When using the ion beam as a source of barium, the beam was started early and physically shuttered to control the time and duration of a deposit.

3.2 Spectroscopic System

The detection apparatus is shown in Figure 3.5. White light transmission or fluorescence is collected and coupled into the fiber optic bundle which is fed into a spectrometer/CCD. All spectroscopic measurements were made using an imaging spectrometer (Acton SpectraPro-2150-i) attached to a liquid nitrogen cooled CCD camera (Princton Inst. SPEC-10). The imaging spectrometer input is a fiber optic bundle consisting of 19 multimode fibers arranged in a vertical line for maximum resolution (Fig. 3.6A). The input to the fiber bundle, which is circular at the collection end (Fig. 3.6B), is a fiber coupler consisting of a lens in a tube housing. The coupler contains a 1 cm diameter lens with a 2 cm focal length sitting 1.6 cm in front of the fiber face.

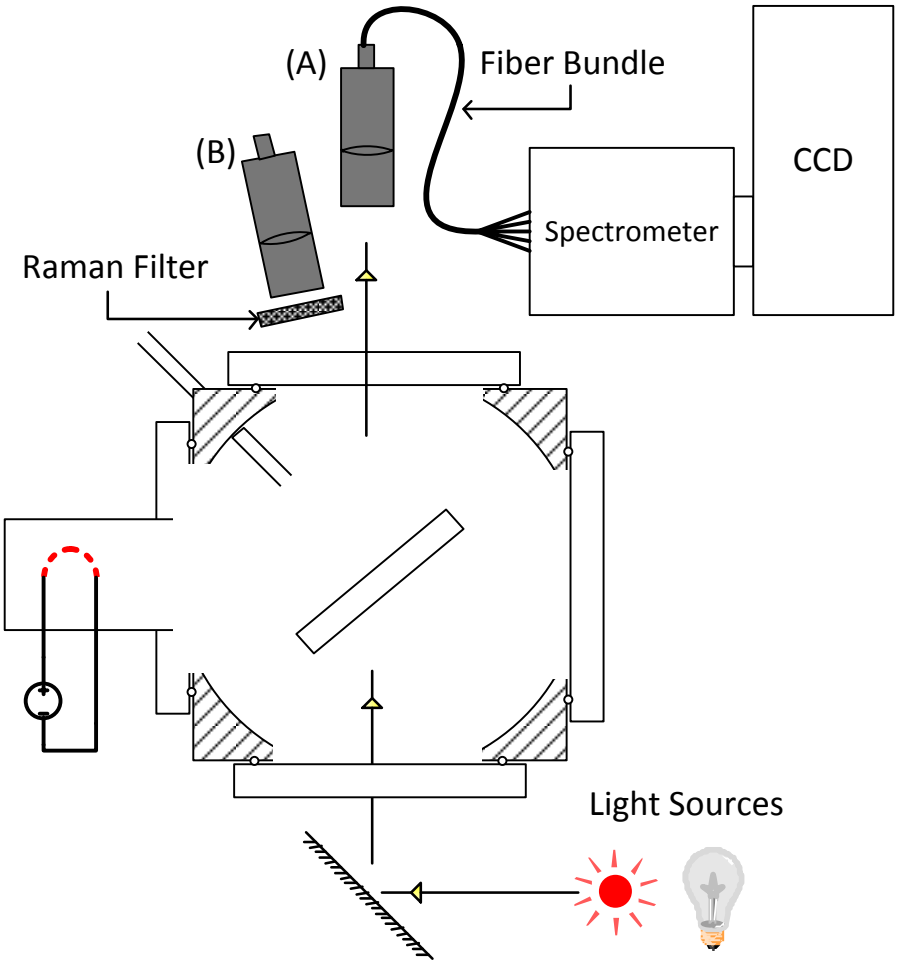

Figure 3.5: Spectroscopic measurement apparatus schematic. Fiber bundle is in position (A) for absorption measurements, and (B) for fluorescence measurements.

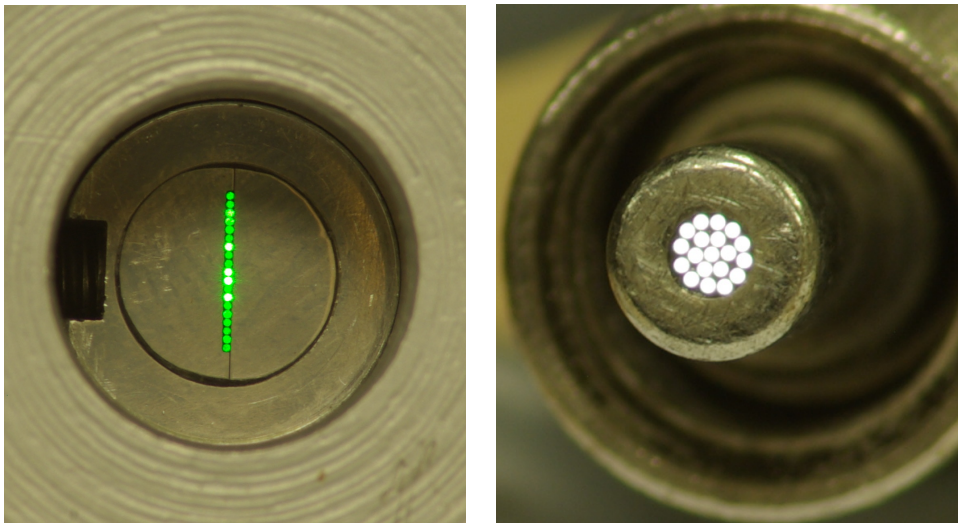

A B

Figure 3.6: Fiber bundle used to couple light into the spectrometer. (A) Spectrometer input end has the individual fibers aligned vertically to act as the input slit. (B) Fiber input is arranged in a circular pattern to accept light coupled into it with a lens.

The spectrometer is equipped with a 300 lines/mm and a 600 lines/mm grating, mounted on a computer controlled turret so that the grating and grating angle can be selected automatically. The grating serves to diffract the incoming light (separating the light in angle by wavelength) onto the CCD detector. The first order grating equation is

$$d\,(\sin\theta - \sin\theta_i) = \lambda \tag{3.1}$$

where d is the separation distance of the lines, θ_i is the incident angle of the light, λ is the wavelength, and θ is the angle of the reflected maximum at that wavelength. The grating groves are oriented horizontally, so different columns on the CCD receive different wavelengths of light.

The CCD chip itself contains a 2 dimensional array of pixels, with a single analog to digital converter (ADC). To get the charge on each pixel to the ADC, the

CCD transfers the charge between pixels, moving each to the readout pixel after the previous has been read and cleared. In imaging mode, where each pixel is read out individually, it begins by reading the bottom row first, then dropping all of the rows down one row and repeating the process. In spectroscopy mode the CCD pixels are grouped horizontally (in columns) so that each group is receiving the same wavelength from the grating. The CCD transfers all of the charge collected down first, and is then readout by the ADC. By grouping the pixels, ADC readout noise is greatly reduced for small signals. A disadvantage is the total signal size must be small enough to 'fit' within a single pixel, 65000 counts. The camera has an additional feature that allows additional grouping of pixels of neighboring columns, referred to as x-binning. This binning is useful for detection of very small signals, when spectral resolution can be sacrificed for additional signal-to-noise. This is demonstrated in Fig. 3.7 where 50 dark spectra were taken for each of the three x-binning settings: no binning, bin by 5 columns, and bin by 10 columns. Then the mean of each pixel was determined and the the difference from the mean for each pixel was put into a histogram. The histogram distributions were fit to gaussians:

$$f(x) = Ae^{\frac{x^2}{2\sigma^2}}, \tag{3.2}$$

where A is amplitude of the gaussian which was also fit. The best fit width of the gaussian was $\sigma = 4.1$ counts for no x-binning. Increasing the binning slightly increased the distribution width. Since the noise does not increase linearly with binning and the signal does, a net overall increase in signal to noise is achieved by binning. The ADC has two different gain modes (slow and fast). It was used in the high (slow) gain mode for all experiments in this thesis. The conversion factor in slow mode is

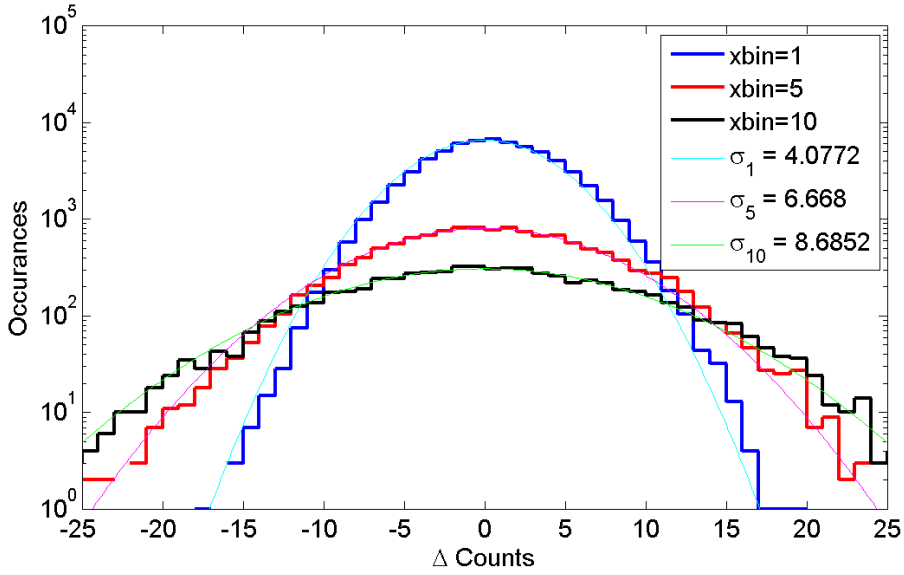

Figure 3.7: Histogram of CCD readout noise with binning. Fifty dark spectra were taken in each case and the difference of each pixel from that pixel's mean was put into the histogram. This determines the variability of the readout.

one ADC count for every 2 photo electrons. The CCD has a quantum efficiency of 90% in the visible.

3.2.1 White light absorption measurements

White light absorption measurements are performed with a halogen lamp filtered with color filters to reduce infrared and red light. The spectrum of the halogen lamp with filters is shown in Fig. 3.8. The light is roughly collimated into a beam by apertures that accept a small solid angle of the emission from the halogen lamp. It is directed though the sample window and coupled directly into the bundled fiber that takes it to the spectrometer (position A of Fig. 3.5). Because the CCD in the spectrometer is sensitive, the white-light beam intensity is reduced with neutral

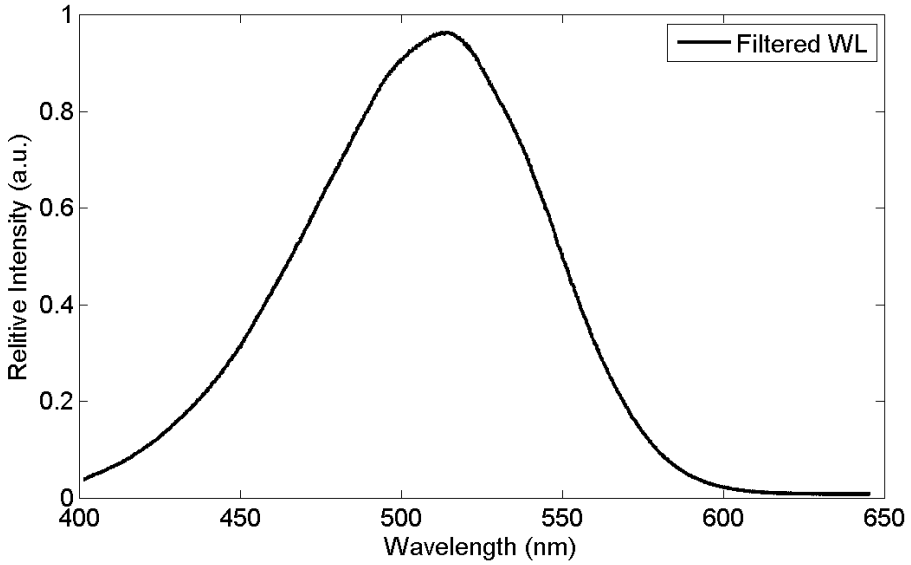

Figure 3.8: Halogen spectrum before and after filtering for use in white light measurements.

density filters. Because the white light that incident on the sample is directly coupled into the detector (no isotropic $1/r^2$ loss), the intensity of this light is small, insufficient to cause any noticeable optical pumping.

The intensity before and after the barium matrix is related to the density of barium atoms (N), path length through the matrix (l), and absorption cross section of matrix isolated barium (σ) via the Beer-Lambert law:

$$I(\lambda) = I_0(\lambda)e^{-\sigma(\lambda)Nl} \, . \tag{3.3}$$

This measurement is useful for estimating the number of barium atoms in the white light beam, which is assumed to have a uniform distribution. The absorption cross

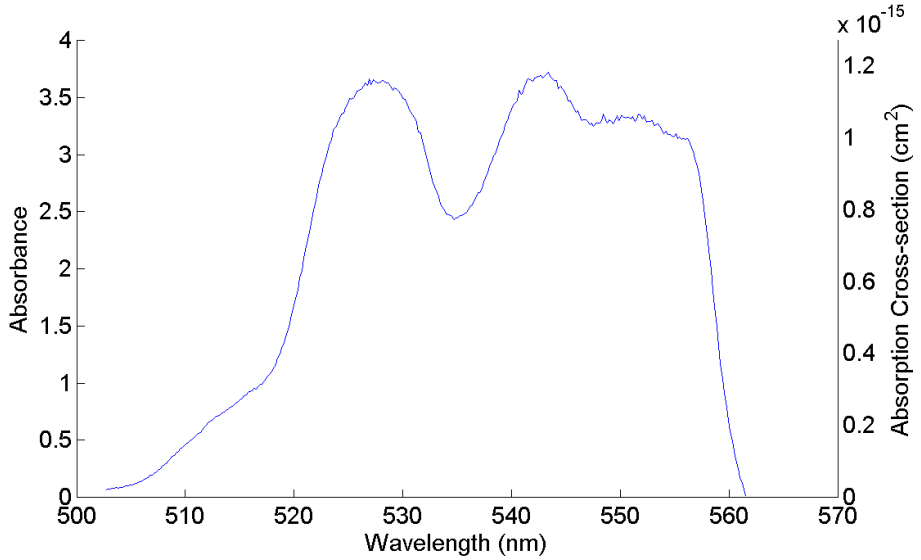

Figure 3.9: Absorbance and absorption cross-section was calculated for barium in solid argon using the absorption measurement.

section is calculated with the following relation:

$$\sigma(\nu) = A_{21}\frac{g_2}{g_1}\frac{c^2}{8\pi\nu^2}g(\nu)\ , \tag{3.4}$$

where

$$\int_0^\infty g(\nu)d\nu \doteq 1\ . \tag{3.5}$$

This has the effect that a wider absorption region has a smaller $g(\nu)$ is at any particular wavelength, and therefore a smaller the absorption cross section at that wavelength. An absorption spectrum from barium deposited in solid argon is shown in Fig. 3.9. The absorption cross-section has been calculated with $A_{21} = 1.19 \times 10^8 s^{-1}$, $g_2 = 3$, and $g_1 = 1$, with the requirement that $g(\nu)$ satisfies Eqn. 3.5. With $\sigma(\nu)$, the number of barium atoms per area, Nl, can be calculated with Eqn. 3.3 from $I(\lambda)/I_0(\lambda)$ measurements.

3.2.2 Laser induced fluorescence measurements

Fluorescence measurements were made using emission from one of several different laser sources. An argon-ion laser with a prism in its cavity provided eight fixed wavelengths (in nanometers): 454.5, 458, 466, 472, 476.5, 488, 496.5, and 514.5. A diode pumped solid state (DPSS) frequency doubled Nd-YAG laser which supplied 532 nm light. There were also two dye-lasers which provided a wide range of laser wavelengths. A Rhodamine 110 laser pumped with the argon-ion laser supplied tunable yellow wavelengths (545-565 nm), and a blue Coumarin 480 pumped with a krypton-ion laser supplied tunable blue wavelengths (450-510 nm). Laser light directed onto the matrix excited barium atoms yielding spontaneous emission of photons as the atoms decay back to the ground state.

Fluorescence is collected by a fiber coupler at an angle to the laser path (Fig. 3.5B). It is placed as close as practical for increased collection efficiency. Scattered laser light is blocked by a Raman edge filter, which is a high pass filter with a very sharp transition. These filters can block laser light with 10^6 attenuation (6 optical density) below the cutoff wavelength, and around 90% transmission above.

A schematic of the fluorescence detection optical system is shown in Fig. 3.10, which also defines the variables. The light is assumed to be a point source a distance d_{sl} from the lens, which is collected and focused by the lens some distance behind the lens, S as determined by the thin lens equation:

$$\frac{1}{f} = \frac{1}{d_{sl}} + \frac{1}{S} \, . \tag{3.6}$$

The diameter of the image at the fiber plane, D_{light}, and consequently the light that hits the fiber optics, is

$$D_{light} = \frac{D_{lens}}{S}\left(S - d_{lf}\right) \tag{3.7}$$

where d_lf is the distance from the lens to the fiber face. Plugging in S from Egn. 3.6 the efficiency of the lens to couple light into the fiber optics can be determined by considering the ratio of areas for the light and the fibers

$$\epsilon_{lens} = \frac{D_{fiber}^2}{{D_{light}}^2}\ , \tag{3.8}$$

where D_{fiber} is the fiber core diameter. A mismatch between the fiber optic numerical aperture (NA) and the collection optics also effects the collection efficiency. This is because the fiber is unable to couple light at incoming angles greater than the total internal reflection angle

$$\epsilon_{NA} = \frac{{NA_{lens}}^2}{{NA_{fiber}}^2} = \frac{\left(S/D_{lens}\right)^2}{{NA_{fiber}}^2}\ . \tag{3.9}$$

The other factors that affect the collection efficiency are constants, such as losses due to surface reflections on the fiber optics and lens. These factors are shown in Table 3.2.

Since the total collection efficiency is a function of the distance the collection lens is from the detection region, it has been calculated for the range of values that are typical for a fluorescence measurement, somewhere around 6 cm, and is shown in Fig. 3.11). The MATLAB^{TM} program that performed this calculation can be found in Appendix A. The collection efficiency used in calculations was 2.6×10^{-5}.

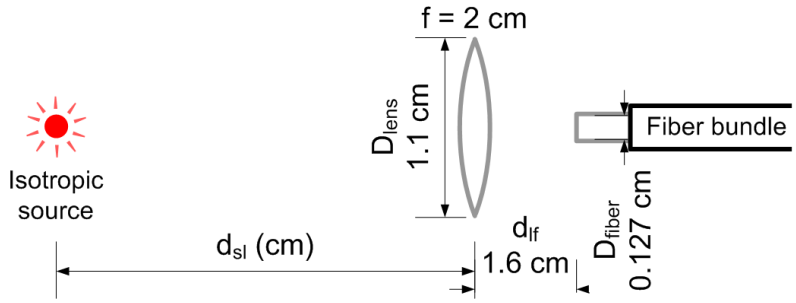

Figure 3.10: Collection optics used for fluorescence measurements. A 2 cm focal length lens collects light and couples some of it into the fiber optic bundle that transmits it to the spectrometer. The distance from the lens to the light source, d, is variable but was typically around 6 cm for most experiments.

Table 3.2: Constant factors for various losses taken into account for the collection efficiency calculation. Fiber core density was determined by counting pixels from Fig. 3.6A.

Description	Name	Value
Counts per photon	ϵ_{cnt}	0.5
Fiber core density	ϵ_{fiber}	0.68
Spectrometer transmission	ϵ_{spec}	0.5
CCD quantum efficiency	ϵ_{CCD}	0.9
Loss to reflections per surface	ϵ_{ref}	0.9

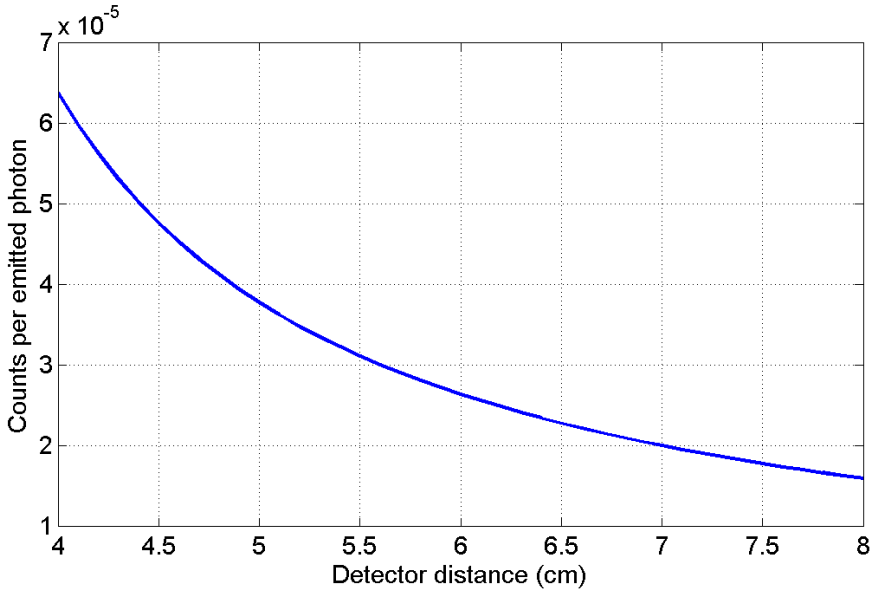

Figure 3.11: Collection efficiency for fluorescence detection. Relates the total number of emitted photons to number of counts measured with the CCD. The detector distance starts from the face of the first collection lens.

3.3 Residual gas analyzer diagnostics

A residual gas analyzer (RGA) was used to monitor the components of the background gas, and the gas leaking onto the sample. It works by ionizing gas near the entrance of a quadrapole mass spectrometer, which transports only the selected ions to a detector. This spectrometer can be tuned to scan $\frac{\text{mass}}{\text{charge}}$ from 0 to 200 amu in our model (SRS RGA-200). This covers common vacuum impurities as well as xenon isotopes. The residual gas analyzer was a useful tool added to the apparatus after battling intermittent failed experiments, which might have been associated with vacuum leaks. By tuning the RGA to helium we were able to find and fix leaks by blowing helium on the outside of the vacuum and looking for a rise in the detected helium inside.

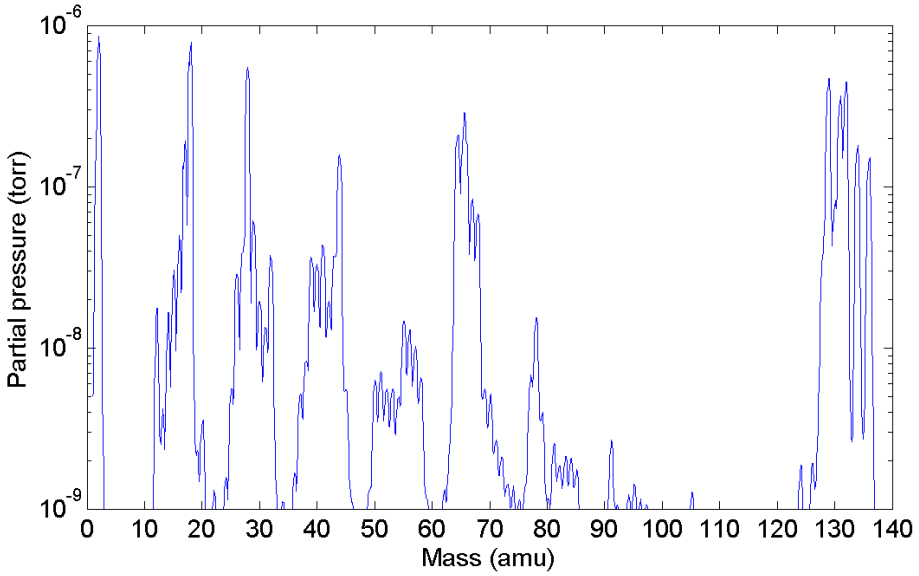

Figure 3.12: A typical "good" RGA spectrum of the vacuum space prior to cooling down. The largest residual vacuum components are H_2, H_2O, N_2, Xe, Xe^{++}.

It is critical to have good vacuum quality prior to cool down as the sampling surface becomes an effective cryopump, which compromises matrix purity. The RGA was used to scan the contaminants of the vacuum system at the beginning of each experiment. These scans sometimes provided hints that leaks in the vacuum system existed, which typically show up as a dramatic increase in nitrogen, oxygen, and argon gas. A typical "good" RGA spectrum is shown in Fig. 3.12. It shows several peaks associated with common vacuum contaminants primarily He, H_2O, N_2. Residual Xe and Xe^{++} from our gas source are also observed because the leak valve can never truly be closed. The cryostat is not bake able due to several rubber gaskets seals, so a significant water peak is not surprising. Nitrogen, however, is an indication of a vacuum leak, particularly when its partial pressure exceeds that of water. These gas levels are tolerable and typical for the barium in solid xenon experiments. A proper

Table 3.3: Gas impurity levels as specified and calculated from leak measurement shown in Fig. 3.13. These values may not represent actual matrix conditions.

Impurity	Gas Specification	RGA Measurement
Kr	$< 5ppm$	0.03%
N_2	$< 3ppm$	1.4%
O_2	$< 0.5ppm$	0.25%
H_2O	$< 0.5ppm$	7.0%

procedure for creating the matrix can also help reduce background contaminants frozen in the matrix as discussed in Section 3.1.2.

The host gas purity was measured with the RGA while the cryostat was warm. The relative increase in gas levels as the xenon gas leak rate was increased is shown in Fig. 3.13. As the xenon leak was increased from 39 to 40, it becomes the dominant gas species, but the other gases also show slight increase. The relative rise in pressures allows a estimate of the contamination in the source gas to be made, and are given in Table 3.3 along with the xenon specifications. The contamination may arise from outgassing in the regulator and stainless steel tubing, although it could be from the xenon gas bottle or xenon gas itself. These measurements are not necessarily representative of matrix deposition conditions since this was a warm measurement at a very low leak rate. Ideally if barium assumes a substitutional site in xenon, it would have 12 nearest neighbors in a face center cubic crystal, and 6 next-nearest neighbors. Having any of these as being an impurity could influence the spectral response. Even a few percent of a contaminant will be a neighbor to a significant fraction of barium atoms. Formation of barium+impurity molecules would reduce the pure barium signal.

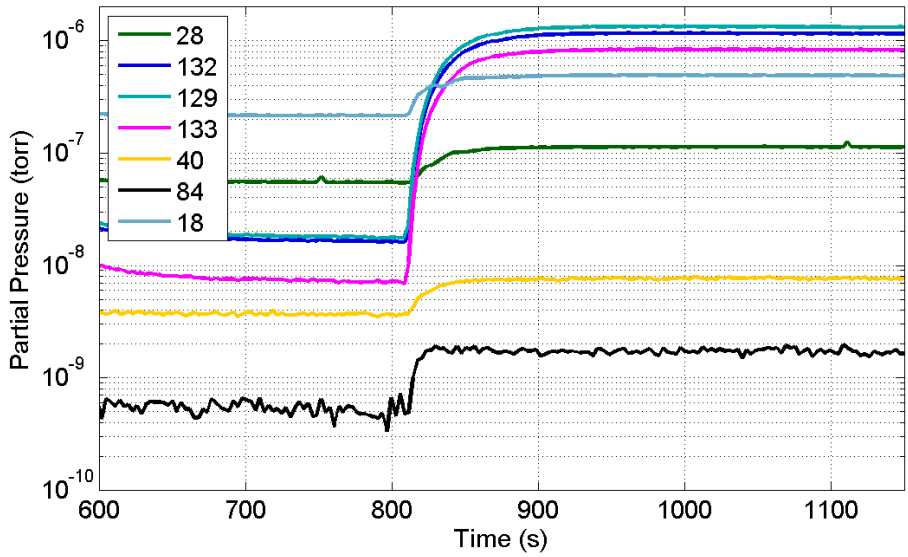

Figure 3.13: Xenon gas composition as measured with an RGA. Leak=39 before 800 seconds, and Leak=40 after 800 seconds. Typical leak rates during experiments are between 42-44.

3.4 Fiber optic detector probe

This section describes a fiber optic probe detector that was tested for single barium atom or ion detection for EXO. First the design of the detector is presented. Then the analysis technique is demonstrated on spectra from 10 Rhodamine 6G (R6G) molecules in methanol which act as analogues for barium atoms/ions. R6G molecules are used because they have similar fluorescence wavelengths and absorption cross section as barium. This example shows how the backgrounds were dealt with to make measurements of single dye molecules.

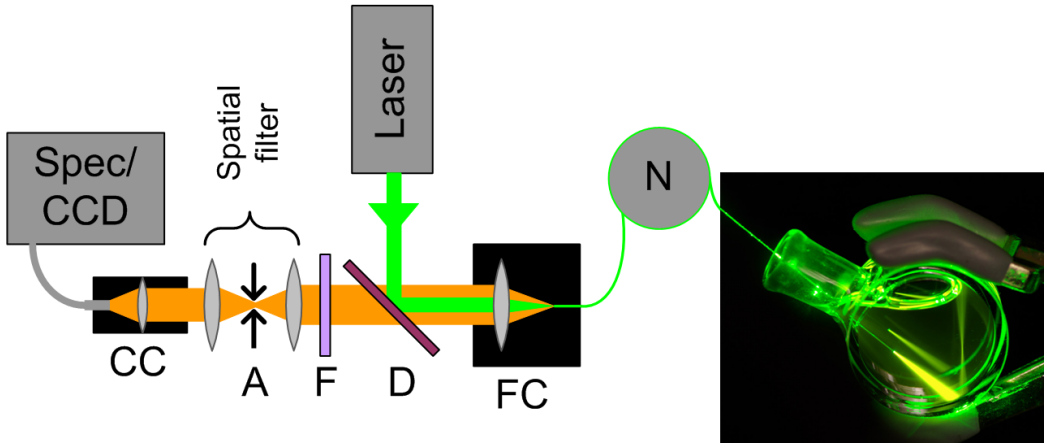

Figure 3.14: Fiber optic probe detector schematic: (D) dichroic, (FC) fiber coupler, (N) wound fiber, (F) Raman edge filter, (A) aperture, and (CC) camera coupler. The fiber probe tip is immersed into a solution with a known concentration of R6G molecules.

3.4.1 Fiber probe detector apparatus

The fiber optic detector apparatus is schematically shown in Fig. 3.14. A dichroic mirror was used to reflect laser light into a lens that coupled the light into a single mode fiber and propagated the light to the detection region. This light excited dye molecules in a small detection volume at the fiber tip. Fluorescence from excited molecules radiates isotropically, and a small fraction of it was coupled back into the fiber. This collected fluorescence propagated back up the fiber and was made into a parallel beam by the fiber coupler. The dichroic mirror let red shifted light, like the fluorescence, pass through to a spatial filter while reflecting backscattered laser light. The core of the fiber was imaged on the aperture of the spatial filter. This blocked light propagating in the cladding, which was mostly background. A Raman edge filter was then used to further block any laser light before it was sent to the spectrometer. Each component is also explained in more detail below.

Table 3.4: Optical fiber properties for the single mode fiber probe.

Operating Wavelength	$460 - 600$ nm
Mode Field Diameter	$3.4 \pm 0.5\mu$m @ 460nm
Core Numerical Aperture	0.13 / 0.12(pure core)
Clad Diameter	$125.0 \pm 1.0\mu$m

The fiber used for the probe detector is Nufern^{TM}HP-460. The fiber is made in two different ways make the index of refraction of the core greater than the cladding: a germanium doped core, or a fluoride doped cladding. The specifications for these fibers can be found in Table 3.4. Experiments were performed using both fiber types. No significant differences in spectra were noticed between the two fiber types.

A Newport^{TM} Model-9091 5-Axis fiber optic aligner was used with an 8 mm focal length aspheric lens to couple light into the fiber. The aligner has 0.02 μm x-y translation resolution which is necessary for good coupling efficiency to the very small fiber core.

The dichroic mirror functions as a highly reflective mirror for wavelengths below its designated cutoff, and transmits wavelengths above that. This design is suited particularly well for separating red shifted fluorescence from scattered excitation light. These filters are made by stacking many dielectric layers together.

The spatial filter takes parallel light from the fiber coupler and focuses it down to a small point where the beam is apertured. This serves to confine the region of light transmitted by the filter. A 15 cm focal length lens was used to focus onto a 100 μm diameter aperture. A second 15 cm lens was occasionally used to recreate a parallel beam after the aperture, but the rest of the time it was simply coupled into the fiber bundle input on the spectrometer. The aperture was mounted to a X-Y-Z translation

stage. Its placement was determined by maximizing the amount of fluorescence signal that was detected when the fiber probe was in a concentrated solution of fluorescent species; at least 10,000 $\frac{\text{molecules}}{10^{-10}\text{cm}^3}$ so that the background signals are negligible.

The Raman edge filter is a series of stacked dielectric layers that work on the principle of constructive and destructive interference. The result is a filter that blocks light below the designed cutoff, and transmits above the cutoff with a very steep rise. These filters typically go from 10^{-6} optical density to transmitting at the 90% level in only a few nanometers. They are commonly used for blocking excitation laser scatter from red shifted fluorescence and Stokes shifted Raman measurements. Fluorescence light that passes through all of these components is measured in the same way as described in Section 3.2, passing directly through the fiber bundle to the spectrometer and CCD detector.

The fiber probe was wound two to three times around a 25 mm diameter cylinder. The end was fixed pointing down towards the optical table. The winding decreased laser scatter and silica Raman scattering propagating in the cladding of the fiber. Vials containing the fluorescent species were raised to the fiber tip, until the tip was just immersed by a few millimeters. For some experiments a shutter was used to block excitation light when spectra were not being taken. This was to prevent photo bleaching the samples unnecessarily.

To calibrate the fiber probe detector the effective light collection volume is needed to determine the average number of dye molecules that are being observed in solution at a time. A Monte Carlo calculation was performed to approximate the collection efficiency as a function of position in front of the fiber tip (Fig. 3.15). The calculation was performed by creating a million light rays in random directions at each point on a grid. The computer program then determined how many rays were physically

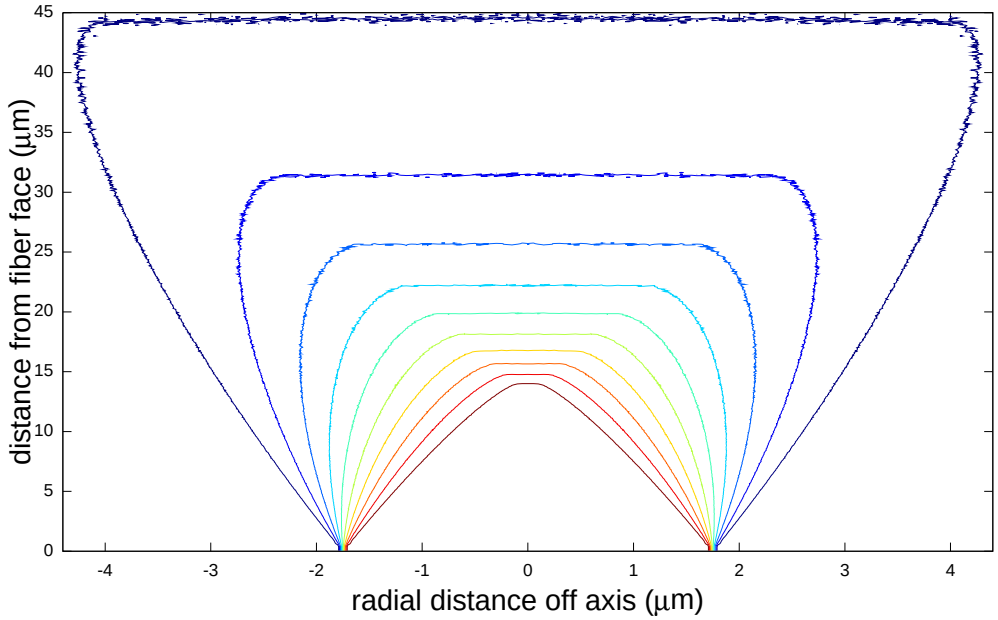

Figure 3.15: Fiber optic detection efficiency as a function of radius and distance. Each region represents a 10% loss from the previous region starting with maximum efficiency at (0,0) of 0.424%. A volume of $100\mu m^3$ is used as the effective detection volume of this fiber probe.

able to be coupled into the fiber core, giving an effective coupling efficiency at each grid point. This calculation neglected the mismatch in wavefront shapes between the emission and allowed modes in the single mode fiber. From Fig 3.15, a detection region of 100 μm^3 was used as the detection volume (that is roughly a cylinder 11 μm long and 1.75 μm in radius). Since the core of the fiber is a few microns in diameter and the numerical aperture is small (NA=0.13 compared to most confocal systems having objectives with NA$\sim$1.0) the collection efficiency is small. The best coupling occurs directly in front of the fiber face, where collection efficiency is limited only by the fiber acceptance angle, determined by its the numerical aperture:

$$\left(\frac{1}{4\pi}\right)\int_0^{2\pi}\int_0^{\sin^{-1}NA}\sin\theta\, d\theta\, d\phi = 0.00424\ . \tag{3.10}$$

This model however does not consider losses due to wavefront mismatch.

3.4.2 Fiber optic probe procedure

Single molecule, or atom, detection requires careful subtraction of background signals. Hundreds of dark spectra were taken before each experiment to average and subtract out readout noise associated with the CCD device. Spectra without sample vials were taken periodically to determine the backgrounds from the fiber detector and system components. These system backgrounds were seldom used for subtraction because the solvent dramatically affected the total background. This is due to differences of the backscattering of light at the interface between the tip and a liquid sample with and without the fluid. Spectra with the tip in a pure solvent sample were measured often since it provided a complete background spectrum. The fiber probe background periodically changed a little bit, perhaps as dye molecules dried on the fiber, or as dried dye molecules became photo-bleached. Raman scattering of the solvent also provided a background.

Most of the work on the fiber probe detector was with R6G in methanol solvent, but etheline glycol was also used. An initial solution was made by weighing the dye and mixing in a known volume of solvent, this solution concentration was also verified by measuring absorption in a 1 cm thick quartz cell with the white light beam described in Section 3.2.1 (Fig. 3.16). Further dilutions were then made from this original solution stepping down each time by a few orders of magnitude to a single dye molecule in 100 μm^3.

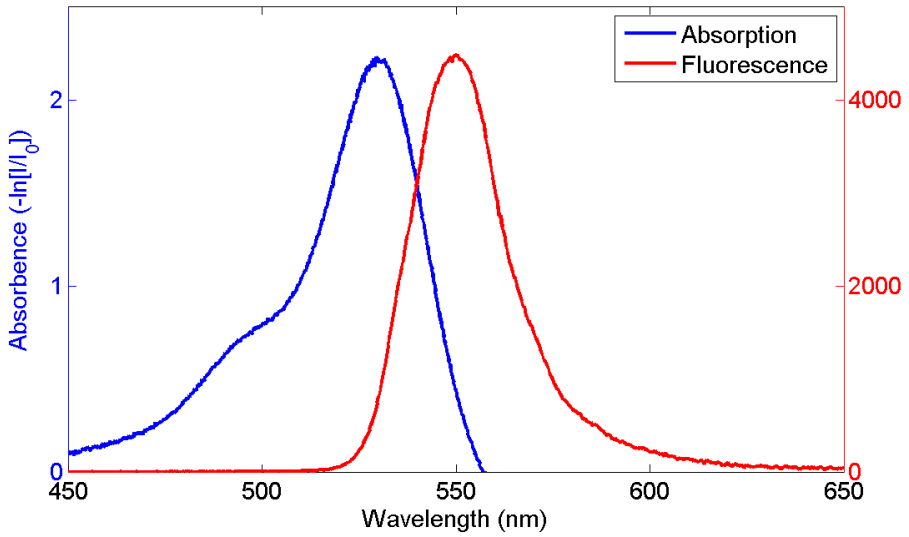

Figure 3.16: Absorption and fluorescence measurements of RG6 solution in a 1 cm thick quartz vial. An absorbence of 2.25 yields R6G concentration of $5.1 \times 10^{15}\text{cm}^{-3}$.

3.4.3 Fiber optic probe analysis technique

Two and sometimes three fitting functions were used to correctly subtract out backgrounds which cannot be held exactly constant (for example, Raman signal was a function of the laser power and tip depth in the solution). The two and three function fitting algorithms work on the principle of residue minimization. Individual component spectra were multiplied by fitting amplitude constants and subtracted from the data. The constants are chosen that minimize the remaining residue by a least squares criterion. This was performed with a MATLAB$^{\text{TM}}$ script that took the spectral components and the combined spectra and returned the best fit constants. These scripts can be found in Appendix C. An example of the fitting method for R6G in methanol for a signal of 10 molecules per $100\mu\text{m}^3$ is reviewed step by step in the remaining part of this chapter.

First several dark spectra, with all light to the detector blocked, were taken and averaged to reduce random noise. This spectrum is mostly an offset from zero but since some pixels are 'hotter' than others, so it is better than using a constant. This dark spectrum is subtracted from all spectra before using them in any analysis.

A fiber detector background spectrum was created by placing the fiber tip in a vial of pure methanol, and many exposures were taken with the laser emission on. This background consisted of silica and methanol Raman scattering as well as any fluorescence from optical components. A sample vial was then placed at the tip and spectra were taken. These spectra contained the fluorescence of the sample, as well as the backgrounds from the system.

The spectral shape for R6G that will be used for fitting is measured using a concentrated solution of 500 molecules. To get a pure R6G spectrum, the background is subtracted. This pure spectrum is shown in Fig. 3.17 along with the background. In Fig. 3.18, the raw signal of a $\sim$ 10 molecule/100μm^3 solution is plotted next to the detector background.

Finally, the experimental dye spectrum was fit to the pure R6G spectrum and the background spectrum using a least-squares method. Each spectral shape going into the fit was multiplied by a fitting constant that when summed fits the data with the minimum residual. The fitting constants were then used to accurately subtract out the background and determine the number of fluorescing molecules in the sample. The background subtracted spectrum for a 10 molecule solution is shown in Fig. 3.19. The resulting spectral shape was identical to a R6G spectrum, and the R6G fit weight was 0.032 (0.032*500 = 16 molecules), i.e. 16 molecules per 100 μm^3 were observed. This is not exactly in agreement with the numbers calculated from the dilution factors, but is approximately the same.

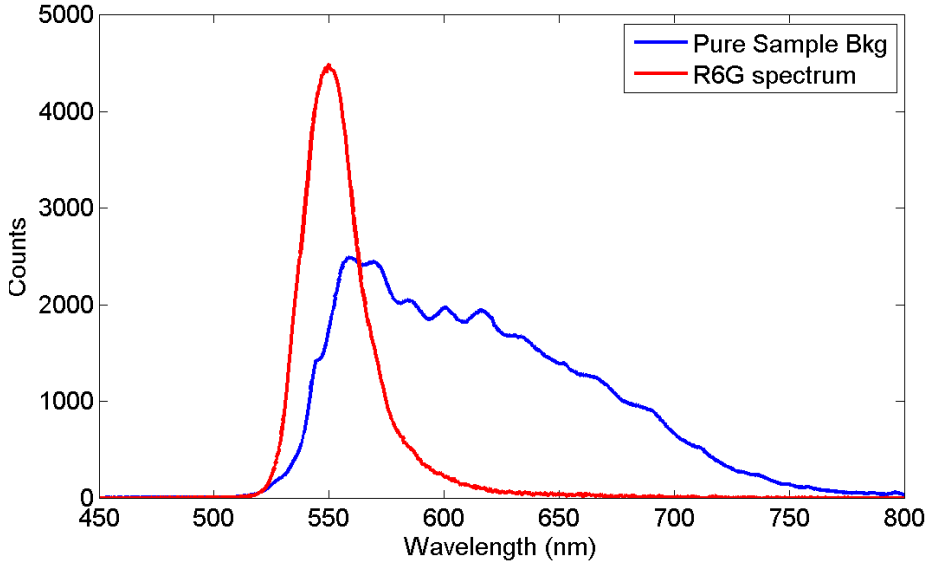

Figure 3.17: Fiber detector signals for 500 molecules of R6G and the detector background.

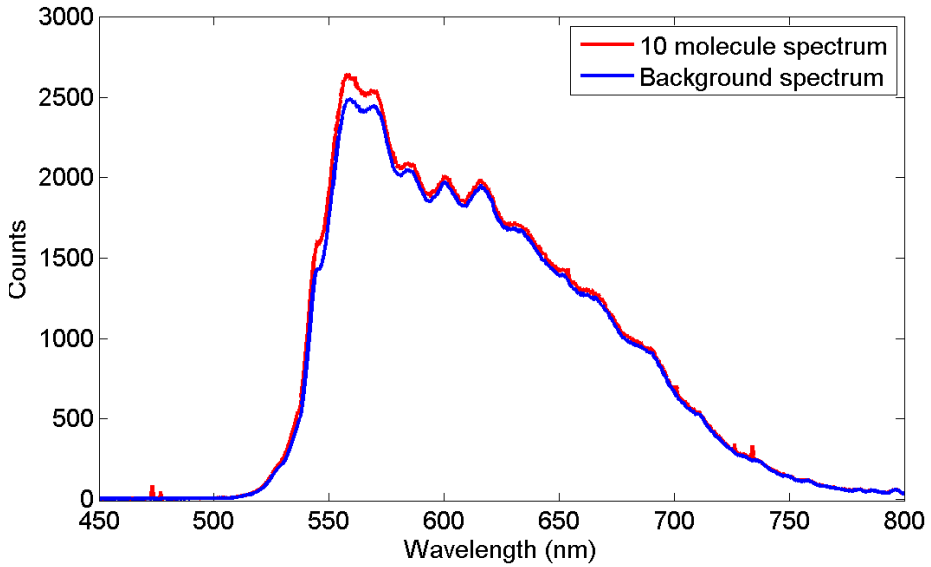

Figure 3.18: Fiber detector $\sim$ 10 molecule raw spectrum.

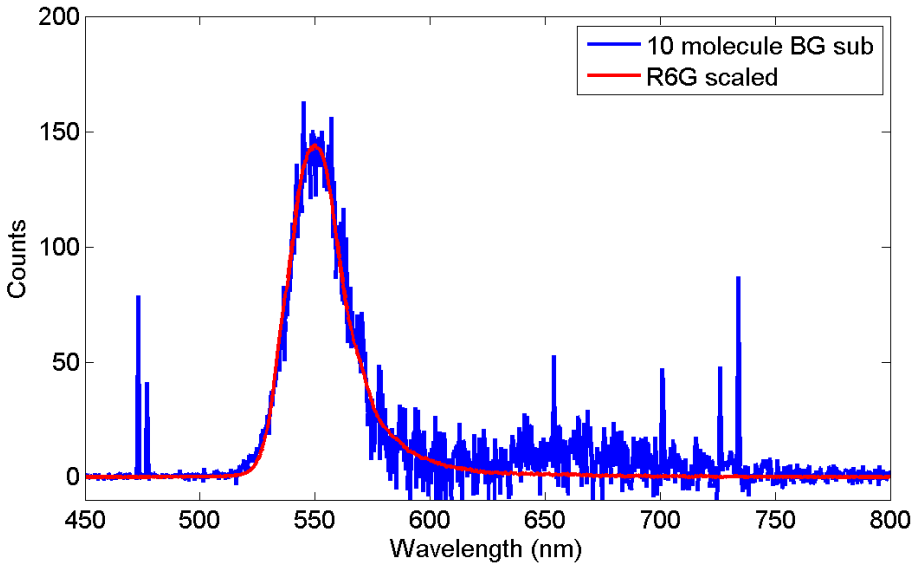

Figure 3.19: Fiber detector demonstration of a 10 molecule, background subtracted, spectrum.

Chapter 4

Results

Results for spectroscopy of barium atoms in solid argon matrices are presented first, followed by results of barium in solid xenon matrices. Absorption and fluorescence peaks were identified in both cases and associated with neutral barium transitions in vacuum. Saturation measurements and experiments with smaller numbers of atoms were performed, and based on these results the required conditions for detecting a single atom in solid xenon are presented. Finally, experiments with a single mode fiber optic probe are presented as a demonstration of this method as a tagging device for the next generation EXO experiment.

4.1 Barium in solid argon

Spectroscopy of barium in solid argon was performed first to become experienced with matrix-isolation methods, and in part because the spectrum had already been established [51]. Argon was also easier to work with, and more economical during the

learning period. Comparing the results of barium in solid argon with those in solid xenon also helps in interpreting the results.

The absorption and fluorescence, excited with 532 nm, spectra of barium atoms in solid argon is shown in Figure 4.1. The main absorption feature from 520-560 nm is close to the resonance transition at 554 nm in vacuum, therefore it is assigned to the $6s^2\ {}^1S_0 \rightarrow 6s6p\ {}^1P_1$ transition. This spectrum was similar to Balling and Wright's (Fig. 2.5) who also assigned it to this transition. Interactions of barium with the solid matrix broadens the absorption spectrum, and multiple absorption peaks were observed. The multiple absorption peaks may be due to barium in different local environments in the argon matrix, called sites, or could be due to energy level splitting in the matrix environment. There were also three absorption peaks in the blue (452, 461, and 465 nm) which were observed the for the first time for barium in an argon matrix. The fluorescence spectrum, also shown in Fig. 4.1, was from excitation with a 532 nm laser. The fluorescence spectrum also clearly shows three peaks. We label the fluorescence peaks from blue to red as: A (542 nm), B (552 nm), and C (562 nm).

A barium-argon matrix sample was excited with 532 nm and 514 nm laser light, which preferentially excited different emission peaks, as shown in Fig. 4.2. The relative strength of the A and B emission peaks was significantly different between the two excitation wavelengths, even upon repeated excitation. This may be evidence that the absorption peaks are associated with particular matrix sites that also produce individual fluorescence peaks. Excitation with 532 nm more strongly excited the bluest and sharpest A-peak site, while 514 nm excitation excites on a broad shoulder, and produced more broad B-peak fluorescence.

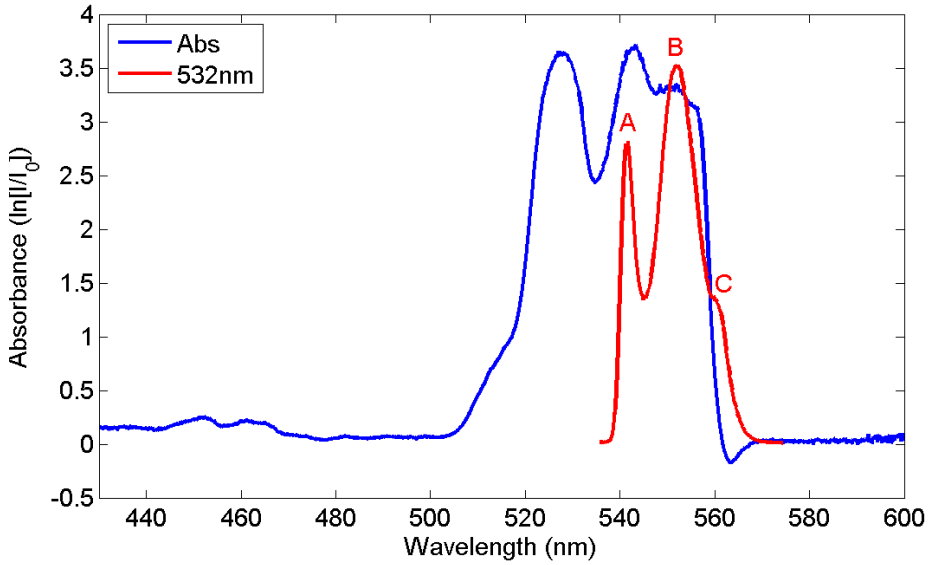

Figure 4.1: Barium in SAr matrix absorption and 532 nm laser induced fluorescence. Fluorescence peaks are labeled as: A (542 nm), B (552 nm), and C (562 nm).

Spectra taken while slowly depositing a barium-argon matrix using the getter source shows proportionate growth of the peaks as excited by 532 nm laser (Fig. 4.3). This demonstrates that barium deposition in the various sites is constant throughout sample creation. The probabilities for barium to choose a particular site may be related to the deposition conditions like xenon leak rate and matrix temperature (see [57] for a discussion), but were not explored in this work.

Annealing the matrix (raising then lowering the temperature) after deposition resulted in changes in relative heights of the peaks in the fluorescence spectrum. Spectra at the maximum and minimum temperature points are shown in Fig. 4.4 for three subsequently higher annealing cycles. Annealing the matrix caused peak-B to decrease, and peak-A to increase (peak-C was no longer visible). Each annealing cycle caused a permanent loss in peak-B, while peak-A gained in height with suc-

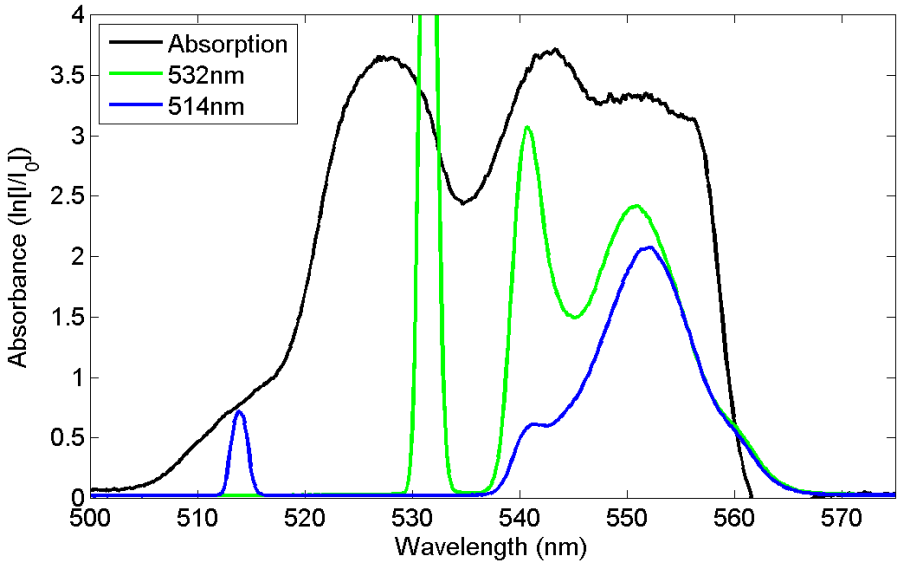

Figure 4.2: Ba-SAr fluorescence differenced induced by 532nm and 514 nm excitation plotted with the absorption spectrum. The lowest wavelength feature in both spectra is laser scatter that was not completely blocked by the Raman filters. Differences in spectra between experiments can be induced by exposure to laser light or caused by deposition conditions.

cessive cool-downs. This is evidence that these peaks are due to different sites in the matrix. A possible interpretation is that site-B (and maybe site-C) is less stable than site-A, and given a perturbation, barium in these other sites move to the more stable site-A configuration. Fig. 4.5 shows the peak heights from Fig. 4.4 plotted as a function of temperature for several annealing cycles. The initial height of peak-A started out at half of its eventual maximum, and then grew after annealing. Conversely each annealing cycle caused some fractional loss of atoms in site-B. This behavior demonstrated that site-B atoms are converting to the most stable site-A. The fluorescence signal from site-A was also seen to decrease reversibly during the increases in temperature up to at least 25 K, but less than 30 K. This temporary loss could be caused by increased matrix vibrational energy with temperature, allowing

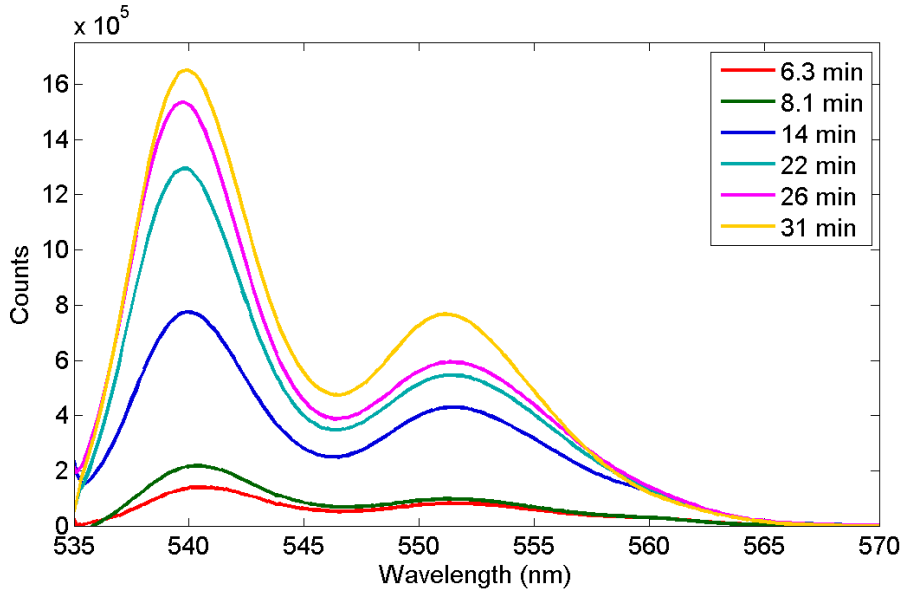

Figure 4.3: Ba-SAr growth of a deposit excited by 532 nm.

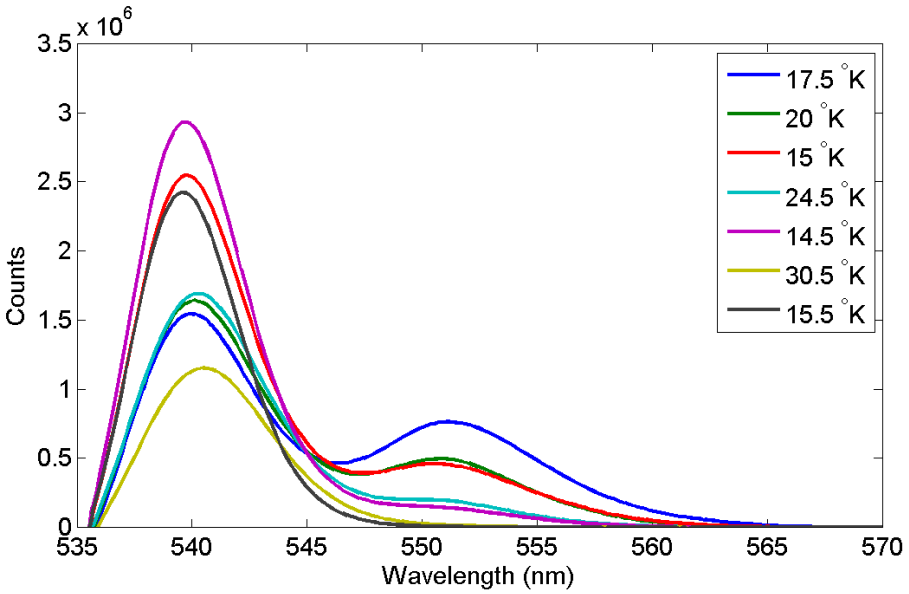

Figure 4.4: Annealing barium in solid argon converts B sites to A sites. Spectra are plotted at extreme temperatures over the course of three subsequently higher annealing sessions.

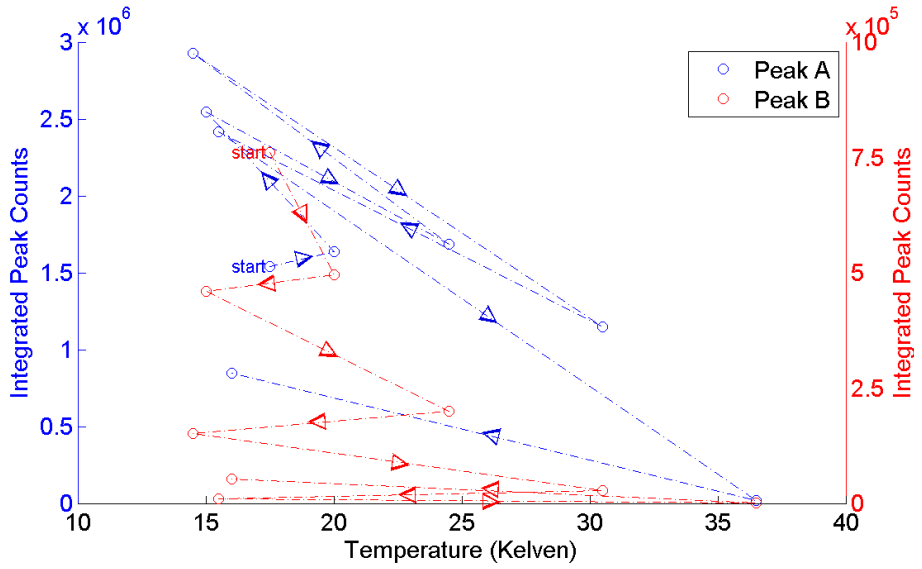

Figure 4.5: Peak heights of (A) and (B) sites of barium in solid argon during annealing over many cycles. The loss of (B) and gain of (A) for annealing below 25 K may suggest (B) sites are converting to (A).

more non-radiative decays. When matrix temperature was raised above 25-30 K the fluorescence is permanently lost. This is around the temperature that the solid argon matrix sublimates. It is unknown what happens to the barium when the argon matrix evaporates; it could also evaporate, or it may be left behind on the sapphire plate. It has been demonstrated, however, that no fluorescence is seen after the argon matrix is gone, or while the next sample is being prepared.

It was also found that deposition of mass-selected barium ions from an ion beam gave some neutral barium fluorescence. Spectra were taken of the initial deposit and then continuously during continued exposure to the excitation laser (Fig. 4.6). These spectra are from a one second ion deposit with 12.7 nA/mm^2 of Ba^+. The excitation is with 6 mW of 532 nm laser light in a 0.8 mm^2 area, and spectra are 0.1 second exposures. This is identified as neutral barium because is coincides with the known

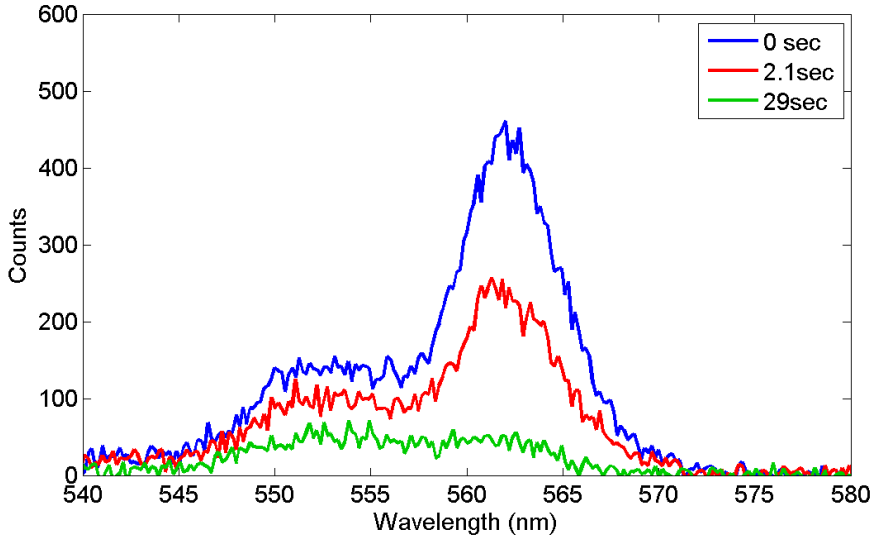

Figure 4.6: Neutral barium spectrum deposited as barium ions, correspond to peaks B and C previously observed from the neutral source. Spectra are shown at various points during continuous exposure to excitation wavelength.

neutral peak-B and peak-C from Fig. 4.1. Peak height differences, and the fact that peak-A is missing entirely, may be due to the difference in deposition conditions (such as high velocity deposition).

The exposure of the neutralized barium, deposited as ions, in solid argon to laser light caused a reduction of fluorescence signal with time. This is shown in Fig. 4.7 for the same one second deposition in Fig. 4.6. Barium atoms in site-C were affected by exposure more than the site-B. Peak heights for B and C are shown decaying, rapidly at first, then slowly.

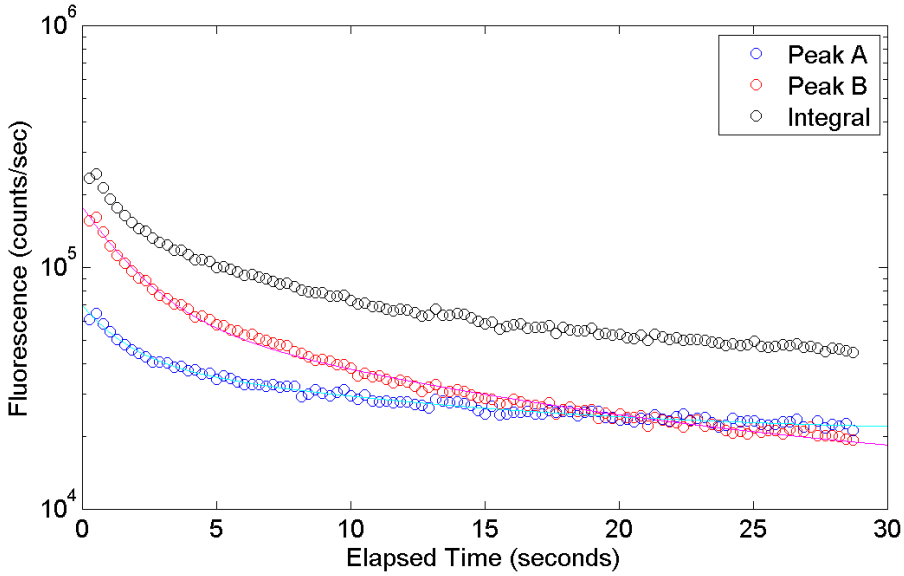

Figure 4.7: Bleaching of neutral barium deposited as ions in solid argon with continuous 532 nm laser exposure, looking at peaks A and B, and integrated fluorescence.

4.2 Barium in solid xenon

The absorption spectrum of barium in solid xenon and the emission spectrum with 532 nm excitation are shown in Fig. 4.8. The large absorption region between 520 and 570 nm is close to the 553.7 nm line, and therefore is attributed to the $6s^2\ {}^1S_0 \rightarrow 6s6p\ {}^1P_1$ transition. Similar to argon, absorption in xenon has multiple peaks believed to be associated with unique sites barium can occupy in the matrix. The absorption spectrum is centered closer to the vacuum transition than it was in argon. The absorption is also red-shifted compared to argon, which is predicted by the heavy atom effect (Section 2.2). A blue absorption band was observed with three distinct peaks at 457, 463, and 470 nm. These absorptions might be associated with transitions out of the metastable $6s5d$ states. These absorption peaks are also shifted

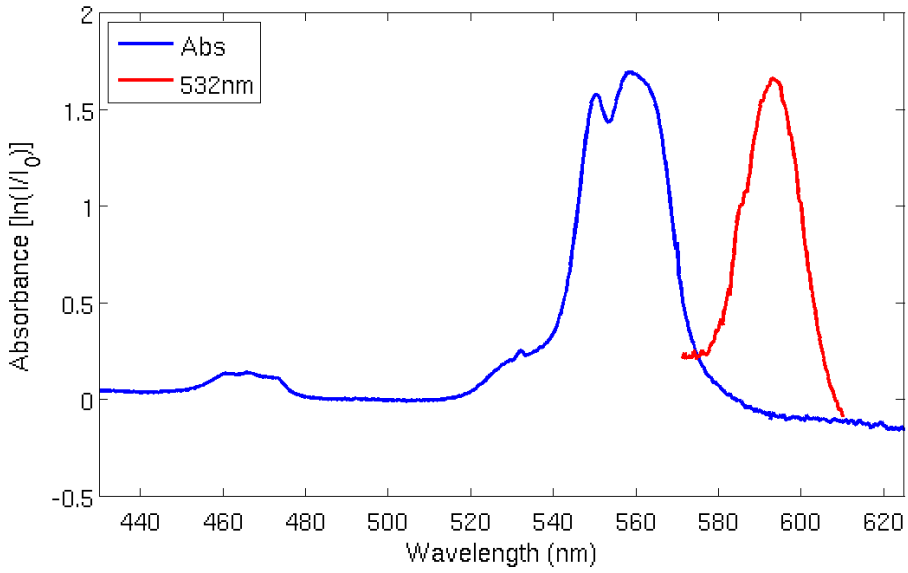

Figure 4.8: Absorption and 532 nm laser-induced fluorescence of barium isolated in solid xenon.

to slightly longer wavelengths in comparison to the observed blue absorption peaks in solid argon. Fluorescence from the $6s6p\ ^1P_1 \rightarrow 6s^2\ ^1S_0$ transition excited with 532 nm was shifted from the vacuum transition by +40 nm, centered at 594 nm. In contrast to solid argon, there were no well separated fluorescence components in xenon, but there was a hint of a shoulder on the blue side of the main peak, centered at 579 nm.

The absorption cross-section for the $6s^2\ ^1S_0 \rightarrow 6s6p\ ^1P_1$ transition was calculated (see Sec. 3.2.1) from the absorption spectrum in Fig. 4.8 using Eqn. 3.4; this is shown in Fig. 4.9. This assumes a conservation of integrated absorption compared to vacuum in the matrix, which has not been explicitly verified. The cross-section peaks at 558 nm at $1.2 \times 10^{-15}\text{cm}^2$. In experiments with the dye laser, this wavelength was used to optimally excite barium in solid xenon. For most of the experiments, however,

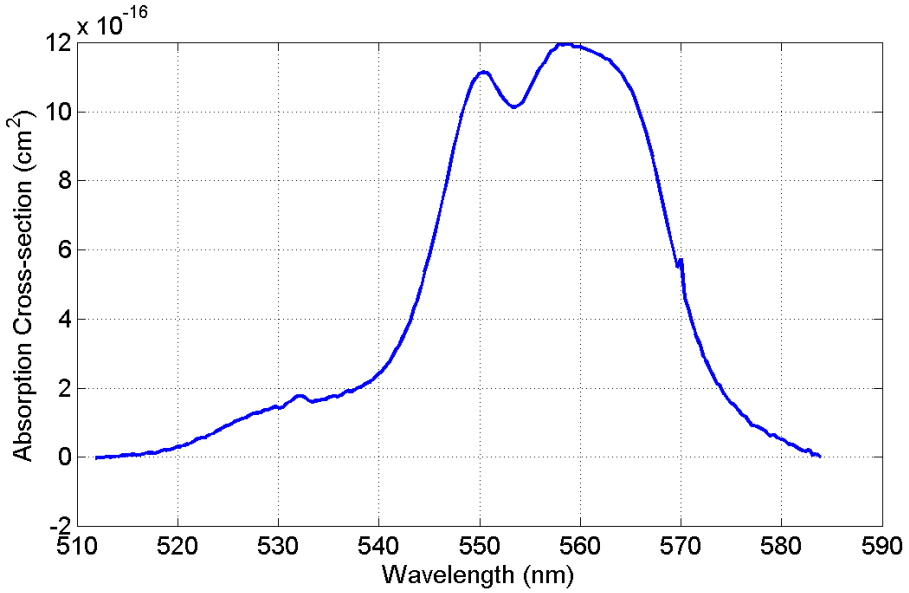

Figure 4.9: Absorption cross section calculated from absorption spectrum for the $6s^2\ {}^1S_0 \rightarrow 6s6p\ {}^1P_1$.

532 nm was used to excite barium atoms. Note that the absorption cross-section at 532 nm is $1.6 \times 10^{-16}\text{cm}^2$.

Excitation of the blue absorption region was performed using several fixed wavelengths from an argon-ion laser in the blue absorption region. New fluorescence peaks were found at 482.4 nm, 492.4 nm, 532.4 nm, and 552.2 nm (Fig. 4.10). These fluorescence peaks may be associated with absorptions out of the metastable $6s5d$ states, emitting and returning to the metastable state (see Fig. 2.1). The small sharp peaks in the 454 nm spectrum were from the argon-ion laser spontaneous emission which did not subtract out. Because there are a number of possible transitions in this region, it is difficult to determine which transitions these peaks correspond to.

The $6s6p\ {}^1P_1 \rightarrow 6s^2\ {}^1S_0$ fluorescence emission rate was observed to rapidly decrease when exposed to 532 nm emission from the laser source. The integrated fluorescence

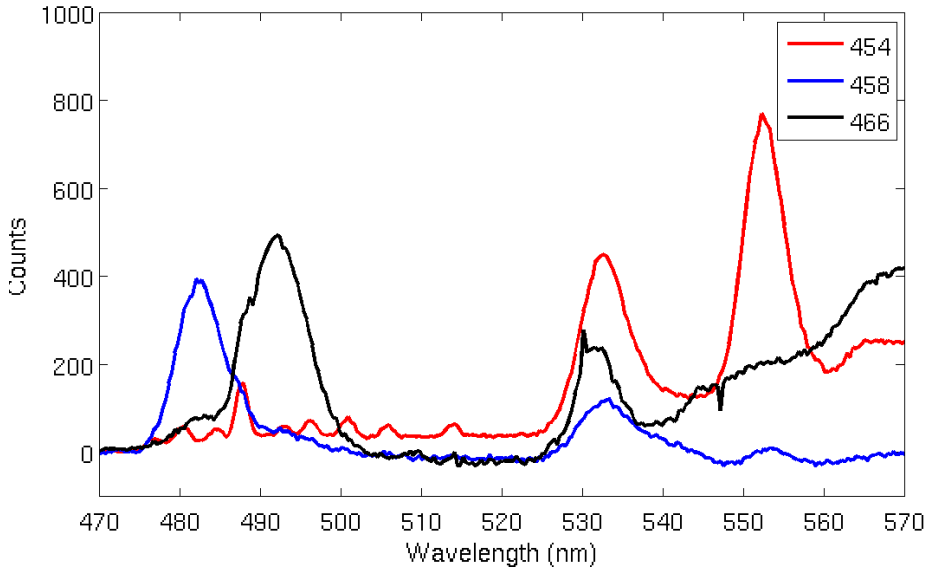

Figure 4.10: Ba-SXe excited by argon-ion laser wavelengths, background subtracted. Deposit made with the getter source.

counts for spectra taken in rapid succession of neutralized barium, deposited with the ion beam, during continuous laser exposure is shown in Fig. 4.11. The neutral atom fluorescence associated with $6s6p\ ^1P_1 \rightarrow 6s^2\ ^1S_0$ transition dropped by a factor of three in the first 50 seconds of exposure, rapidly at first and then more slowly. This could be from optical pumping, barium site shifting, or photo bleaching. After a period of time with no laser light incident on the sample a small portion of the original fluorescence returned.

The fluorescence loss during bleaching is best fit with a dual exponential ($R^2 = 1.0$) rather than a single exponential ($R^2 = 0.95$). Fit parameters for the data in Fig. 4.11 for both fits are given in Table 4.1. If fluorescence loss was due only to populating the metastable states, the decay would be governed by a single exponential

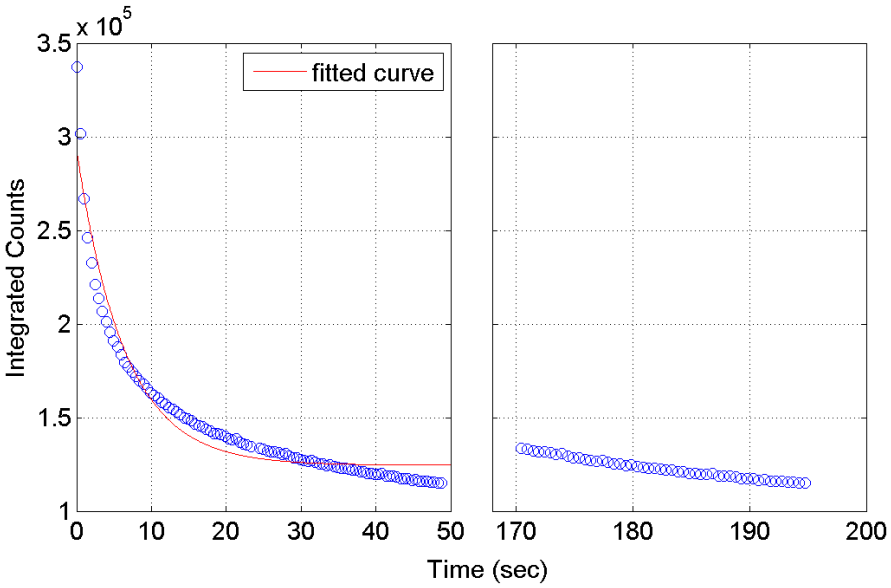

Figure 4.11: Ba-SXe bleaching due to exposure to 532 nm excitation. Laser emission is blocked between datasets, during which time the fluorescence recovers slightly. Single exponential form is A*exp(-x*B)+C, and dual exponential form is A*exp(-x*B)+C*exp(-x*D)+E.

Table 4.1: Ba-SXe bleaching rates for a small deposit excited by 532nm laser. Error based on 95% confidence interval.

	$Ae^{-Bt} + Ce^{-Dt} + E$	$Ae^{-Bt} + C$
A	$1.26(3) \times 10^5$	$1.68(9) \times 10^5$
B	0.66(2)	0.157(15)
C	$1.01(2) \times 10^5$	$1.25(3) \times 10^5$
D	$6.23(26) \times 10^{-2}$	
E	$1.100(5) \times 10^5$	

(see Section 2.1.1). It is not understood why the behavior fits a two exponential function best.

To determine the minimum number of atoms needed to detect a fluorescence signal in our current configuration, the total number of atoms deposited in a sample is needed. This can found for a sample prepared with the neutral getter source by measuring white-light absorption and using Eqn. 3.3. Alternatively an ion beam deposit can be made with a known ion beam flux and neutrals can constrained by the limit of ions deposited (assume 100% neutralization). Both techniques have advantages and disadvantages. Calibration of a deposit using white-light absorption requires a large density of barium atoms to see absorption (10^8 atoms in a focused excitation beam), in order to calibrate the fluorescence yield. This requires extrapolating over eight orders of magnitude in fluorescence signal to detect a single atom. The ion beam, on the other hand, can deposit a single ion in our detection region, but the unknown neutralization efficiency, Coulomb repulsion from already deposited ions, and effects of high velocity deposition give uncertainties in the total numbers of neutral atoms in reasonable site configurations. In either case, with 532 nm excitation, fluorescence loss due to bleaching or optical pumping complicates the results. Fluorescence is

therefore measured after significant exposure to excitation light to ensure the same steady state conditions are used for this measurement.

The fluorescence detection limit was measured first using 532 nm excitation light. Barium was slowly co-deposited with xenon using the getter source while continually taking fluorescence spectra. As barium was deposited the fluorescence slowly grew, which continued until a substantial deposition was made where absorption could also be measured. The fluorescence yield with the large deposits were calibrated with the number of atoms in the area, determined by the absorption spectrum. Then by extrapolating back to the first fluorescence signal, the number of atoms could be determined giving an effective detection limit. The integrated fluorescence for each shot during the whole experiment, as well as the getter current, is shown in Fig. 4.12. Each colored point represents a series of 5 fluorescence measurements in rapid succession, labeled with a series number. The getter was turned off after initial deposition, then turned back on to continue deposition so absorption could be measured. Two absorption measurements were made and noted in figure at the time taken for reference. To illustrate the initial fluorescence spectrum growth, the first several spectra are shown in Fig. 4.13 which correspond to the first two series of colored dots in Fig. 4.12. The integrated fluorescence counts for these spectra are listed in Table 4.2. This sum consists of 201 individually read channels of the CCD in the range of 575-615 nm. Readout of individual channels (no x-binning) allowed larger signals to be detected without saturation of the CCD, at the expense sensitivity and additional noise (see Section 3.2). The standard deviation of the first seven spectra was 107 counts[1], therefore the first clear signal above background was shot 32-3 with

[1]Assuming gaussian noise from the CCD readout, the fits from Fig. 3.7 gives $\sigma = 4.1$. The expected readout noise for 201 channels is $\sigma \times \sqrt{N} = 58$. Fluctuations in laser power are one possible source of larger than expected fluctuations.

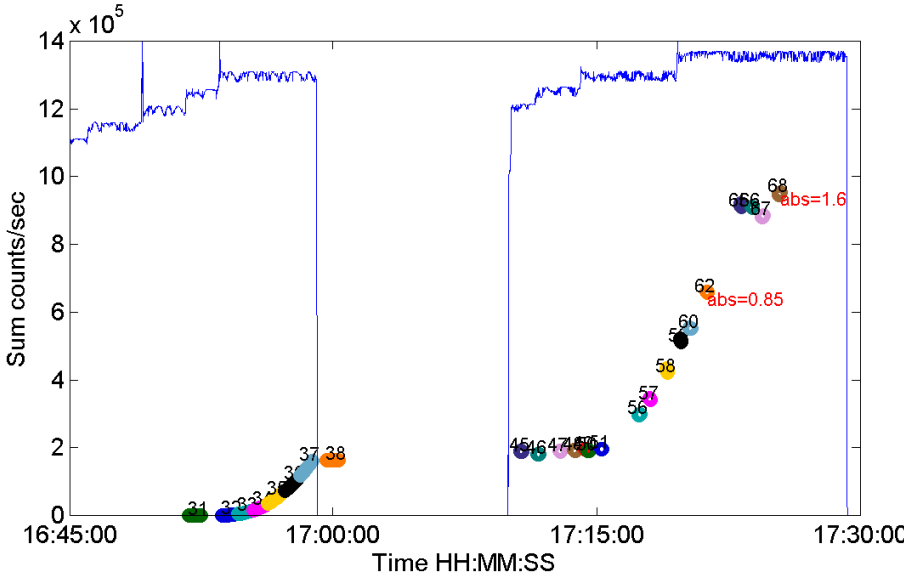

Figure 4.12: (Points) Ba-SXe integrated fluorescence during deposition with getter source, each color represents a series of five spectra. (Line) Getter current in amps. Deposition of barium continues until the absorption can be measured, giving the number of atoms per area. Absorption measurements were made for shots 62 and 68, with a absorbance of 0.85 and 1.6 respectively. Total fluorescence counts is calibrated to that number, then scaled back to the first detectable signal. This linear extrapolation gives the minimum number of atoms required to observe a signal.

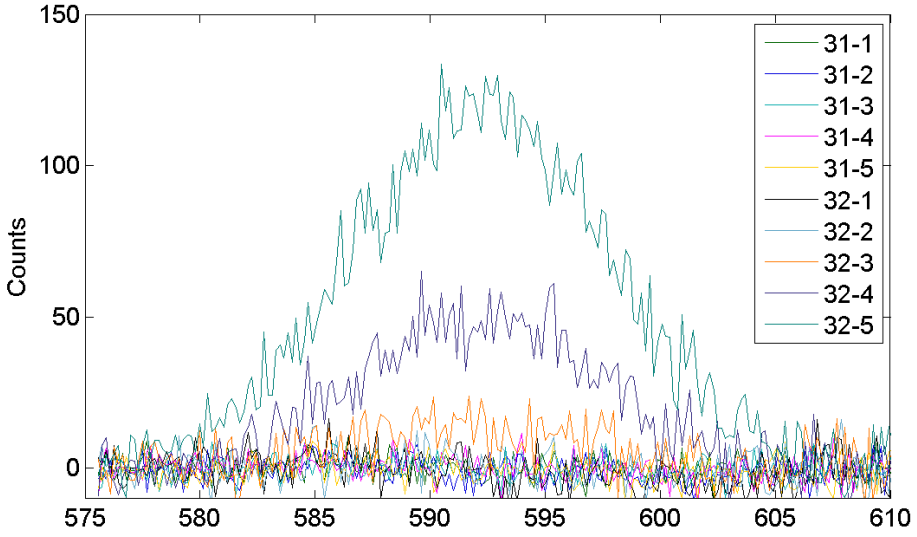

Figure 4.13: Fluorescence spectra of the first observed barium from Fig. 4.12. First detectable spectrum corresponds to shot 32-3.

Table 4.2: Barium in solid xenon integrated counts from with 532 nm excitation. Exposure 32-3 is the first signal detected fluorescence signal.

Exposure	Integrated Counts
31-1	-4
31-2	-176
31-3	-2
31-4	3
31-5	-203
32-1	-170
32-2	59
32-3	1048
32-4	3725
32-5	9505

$> 3\sigma$. The absorbance (α) at the end of the deposit was 1.6, which corresponds to $1.3 \times 10^{15} \frac{\text{atoms}}{\text{cm}^2}$. Fluorescence measurements were made with a laser interaction area

of $5.02 \times 10^{-3}\text{cm}^2$, laser power of 3 mW, and exposure times varied from 10 seconds at the beginning, to 1 second at the end. The final fluorescence measurement (series 68) yielded 9.5×10^5 fluorescence counts in one second from 1.0×10^{13} atoms in the laser interaction area. The first signal identified was 1048 counts in a 10 second exposure, or 105 counts per second. The ratio of fluorescence signals is then used to extrapolate back to the number of atoms in the first positive signal. That is

$$\frac{105}{9.5 \times 10^5} \cdot 1.0 \times 10^{13}\text{atoms} = 1.1 \times 10^9\text{atoms} \tag{4.1}$$

were observed fluorescing in shot 32-3. This technique of extrapolating back to first signals to determine detection sensitivity is difficult because it requires extrapolating back from large barium densities where absorption measurements are possible (10^{12} atoms in the laser area in this case). This can be improved by focusing the laser beam so that fewer atoms being are being probed by the excitation laser. With CCD binning, laser focusing, and resonance excitation, establishing a detection limit on the order of 10^6 atoms with this detection apparatus would be a notable achievement. This is addressed again in Section 4.2.1 using a dye laser tuned to the peak absorption, which is a more efficient excitation source.

A fluorescence efficiency can also be calculated at the absorption calibration point. The number of absorbed photons per second (R_A) is determined by multiplying the absorbance (α) by the photon flux.

$$R_A = \alpha \cdot \frac{P}{h\nu} \, , \tag{4.2}$$

where P is the laser power, h is Plank's constant, and ν is the laser frequency. The fluorescence efficiency is then determined by taking the number of fluorescence count rate observed (F), dividing by the photon counting efficiency ($\epsilon_{det} = 2.6 \times 10^{-5}$) to get rate of fluorescence photons being emitted per second, and dividing by the number of absorption per second:

$$\epsilon_{flur} = \frac{F/\epsilon_{det}}{R_A} \ . \tag{4.3}$$

The fluorescence efficiency was measured for shot 68 to be 2.8×10^{-6} ($\alpha = 1.6$, $P =$ 3mW, and $F = 9.5 \times 10^5$counts/sec). The cause of this fluorescence inefficiency has two primary suspects: barium atoms are being pumped into sites that do not respond to 532 nm excitation, and/or the barium atoms are undergoing non-radiative decay due to vibrational relaxation. The fluorescence efficiency for an earlier shot (shot 62) shows the effect of bleaching caused by excitation exposure: $F = 6.58 \times 10^5$ counts/sec, $\alpha = 0.85$, resulting in $\epsilon_{flur} = 3.71 \times 10^{-6}$. The difference between the two efficiencies is due to the fact that that atoms in the later measurement were exposed to more excitation light, and therefore more were bleached.

Fluorescence with 532 nm laser source was primarily used to develop the technique of fluorescence spectroscopy of barium in solid xenon. The fluorescence yield of barium in solid xenon at 532 nm, however, is low. Fluorescence was observed to bleach rapidly when excited, which would reduce the efficiency of detection. Since 532 nm lies on the shoulder of the main absorption peak the use of a dye laser centered on the maximum absorption would provide better conditions for fluorescence detection.

4.2.1 Barium fluorescence on-resonance (dye laser)

On-resonance fluorescence spectroscopy was possible with the addition of a Rhodamine 110 dye laser to the lab. Conditions using dye laser excitation produced significantly better results for barium fluorescence spectroscopy. One obvious improvement was the absorption efficiency, which increased due to the difference in cross sections (Fig. 4.9) between 532 nm and 558 nm. The fluorescence spectrum as excited with 558 nm fluorescence was the same as spectra taken excited with 532 nm (Fig. 4.14), with a main peak at 594 nm, and a shoulder around 579 nm (the shoulder is less pronounced).

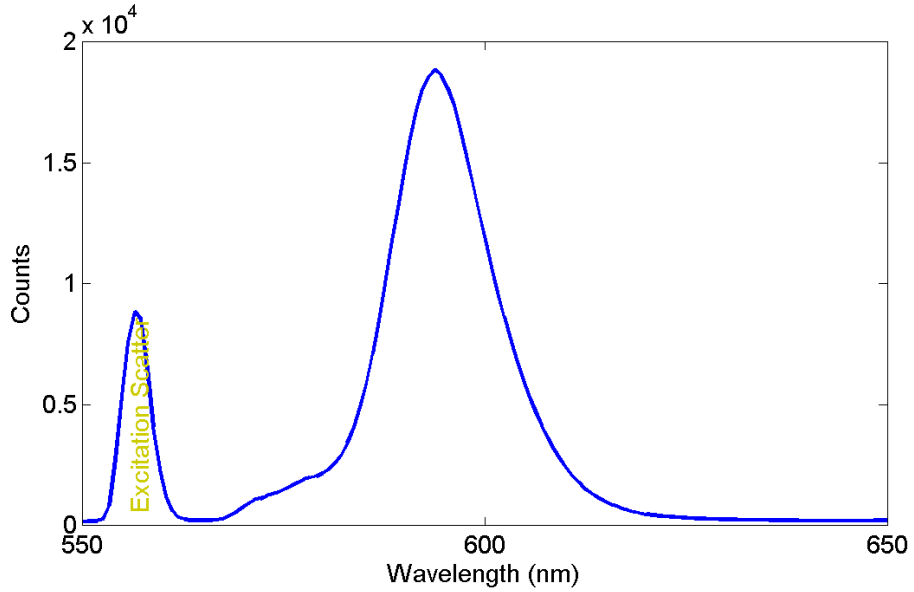

Figure 4.14: Fluorescence spectrum of barium in solid xenon using 558 nm excitation.

Unlike 532 nm excitation where fluorescence bleaching was significant, exposure to dye-laser excitation in the peak absorption region does not cause bleaching, and actually caused the fluorescence signal to rise in a few experiments. The integrated

fluorescence signal is shown in Fig. 4.15 for a series of exposures with a neutral barium deposit until the 37th frame, when it was turned off. The integrated fluorescence continued to rise with exposure to the excitation laser. This behavior, and the bleaching behavior with 532 nm excitation, may be explained as a migration of atoms between two different sites. Barium atoms in the unstable absorption site around 532 nm may be converting to a more stable site at 558 nm.

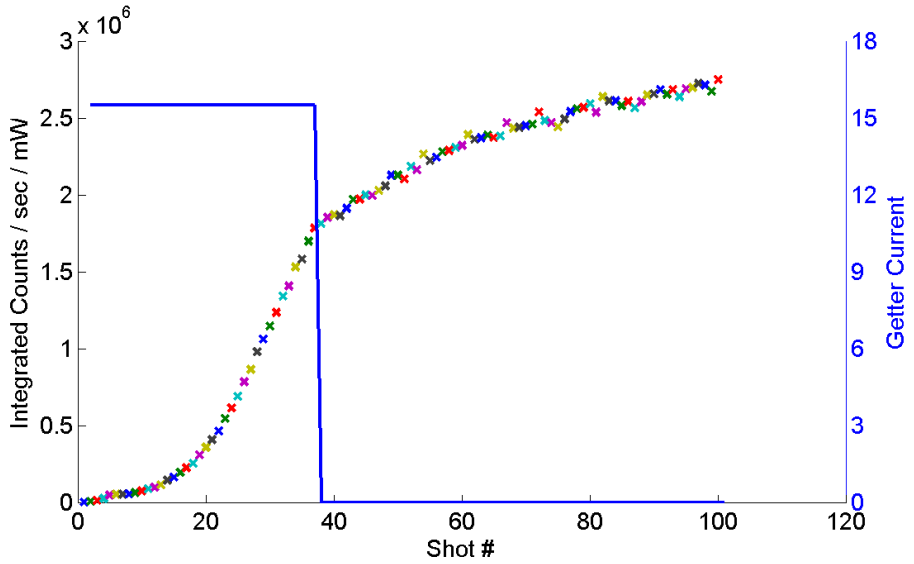

Figure 4.15: Integrated fluorescence gain in repeated spectra during exposure to 558 nm excitation during and after a neutral barium deposition. Getter current (shown in blue) was on for first 37 exposures then turned off. Signal gain with the getter turned off was unexpected. Experiment: 20110716.

The effect of multiple annealing cycles for a sample of barium in solid xenon is shown in Fig. 4.16. The excitation laser was continuously exposed to the sample to maintain steady state pumping conditions. Annealing temperature was varied, and exposures were taken during the annealing process. For each frame the fluorescence spectrum was fit with three gaussians centered at 579, 594, 614 nm with fixed widths and floating heights. The height of each gaussian is plotted at the time taken. The

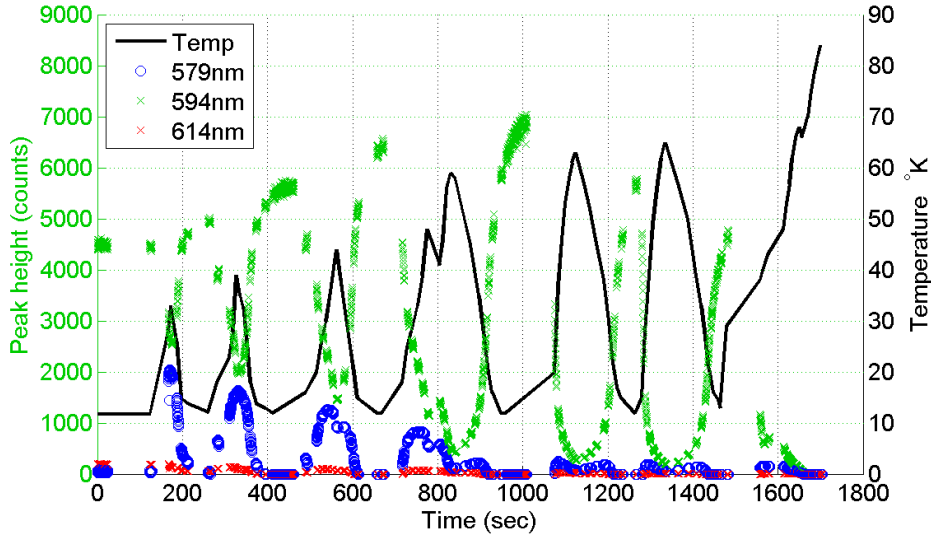

Figure 4.16: Annealing of barium in solid xenon several times. Main fluorescence peak (green) grew with initial annealing up to 60 K. The blue shoulder grew with increased temperature, but subsequent cooling decreased the blue shoulder overall.

temperature during the experiment is also plotted as a function of time. The fluorescence of the main peak at 594 nm decreased with rising sample temperature. This could be evidence for temperature-dependent rates of a non-radiative pathway back to the ground state. Cooling the sample back down increased fluorescence of the main peak beyond initial values. This is evidence that other sites are converted to the main peak site.

The integrated fluorescence signal excited with the 558 nm dye laser was not conserved with annealing. With subsequent annealing cycles the total barium fluorescence increased, as shown in Fig. 4.17. This may be evidence that atoms in non-radiative sites were being converted to fluorescing sites, or the fluorescence efficiency of atoms in other sites is lower than the main site. For single atom detection it will be important to determine whether the low fluorescence efficiency is due to

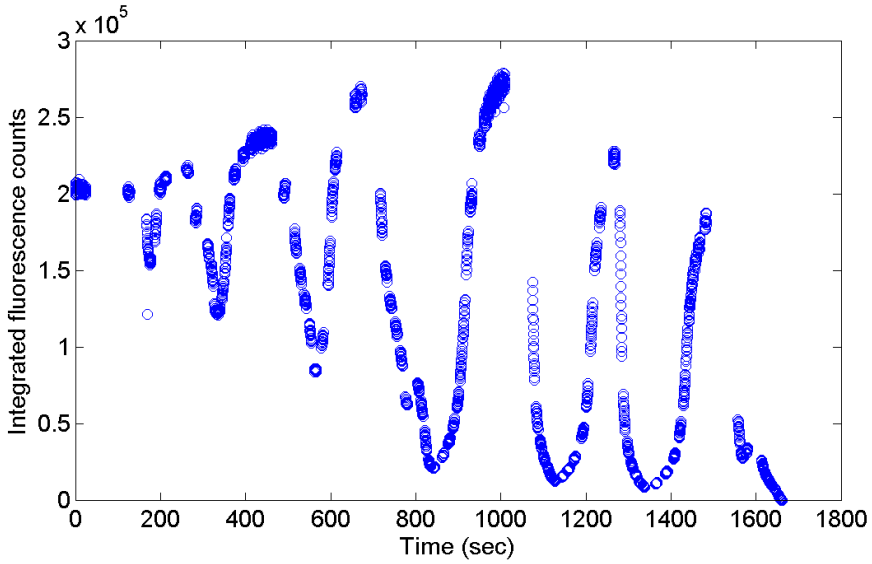

Figure 4.17: Integrated fluorescence gains through the annealing of barium in solid xenon.

inhomogeneous effects, e.g., some barium sites may not fluoresce at all, or homogeneous effects, such as a relaxation pathway that all atoms in all sites use to decay without fluorescing. In either case annealing may be used to get more fluorescence out of barium atoms in solid xenon.

The fluorescence yield was measured at multiple laser intensities to probe for saturation of the emission of barium in solid xenon. The 558 nm excitation laser was focused using a 13 cm focal length lens to probe saturation at large intensities. The laser power was decreased by adding neutral density filters between each measurement. The fluorescence was observed to increase linearly with laser intensity in this range ($y = mx$). No deviation from the linear behavior means that only a limit for A_{31} can be set with this data. The curves represent various A_{31} rates from the the energy level model in steady state (Eqn. 2.15). The values used in the model are given

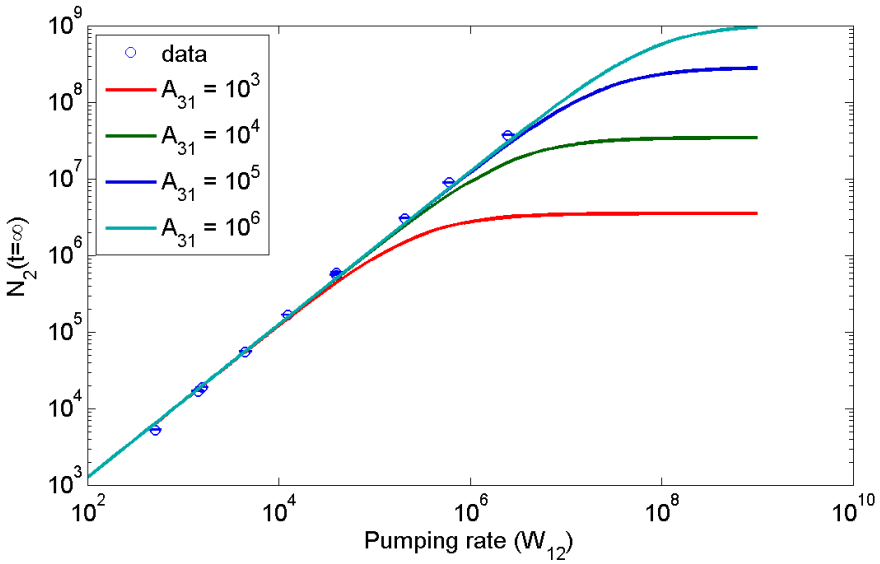

Figure 4.18: Fluorescence intensity curve with 555 nm laser excitation.

Table 4.3: Parameters used to fit saturation data in Fig. 4.18 to a three state pumping model Eqn. 2.15.

N	A_{21}	A_{23}	A_{31}
1.5E^9	1.2E^8	$3.54\text{E}^{-3}A_{21}$	$> 10^4 s^{-1}$

in Table 4.3. Since the data does not deviate from the straight line the conclusion is that atoms decay rapidly out of the metastable D state, i.e., $A_{31} > 10^4 s^{-1}$.

The experiment to determine the smallest number of atoms detectable with the current apparatus was repeated, this time using 558 nm excitation light from the dye-laser, since it strongly excites the most stable barium site in solid xenon without bleaching or significant optical pumping. In this experiment the excitation laser was focused on the sample plate with a 13 cm focal length lens. The beam diameter was not measured for this particular experiment, but can be determined using the dye

laser specifications. The dye laser is a Choherent-599 dye laser, which has a specified beam waist ($\omega_0 = 0.25$ mm) at the output. The beam waist, ω, before the focusing lens is determined using

$$\omega = \omega_0 \sqrt{1 + (z/z_0)^2} \,, \tag{4.4}$$

where z is the distance to the lens, and

$$z_0 = \frac{\pi {\omega_0}^2}{\lambda} \,. \tag{4.5}$$

Using 4 meters for the distance (z), the beam waist is 2.8 mm at the lens. The lens focuses this to a waist of

$$\omega_f = \frac{f\lambda}{\omega\pi} = 8.1\mu\text{m} \,, \tag{4.6}$$

where f is the focal length of the lens. The laser interaction area is then

$$A = \frac{\pi {\omega_f}^2}{2} \,. \tag{4.7}$$

Increased intensities and smaller interaction area enabled smaller numbers of atoms to be probed with the fluorescence laser. The integrated fluorescence signal is plotted in Fig. 4.19 from just before the deposition, all the way to the point where a absorption was measured. At the end of the deposition the absorption measurement was 0.25, corresponding to a total deposition of 2.08×10^{14} $\frac{\text{atoms}}{\text{cm}^2}$. The spectrum for the first few signals are shown in Fig. 4.20. The first detectable fluorescence signal was frame 8 (F08) with 2341 total counts (1814 counts/s/mW) which was $> 3\sigma$ over background fluctuations (N=20, AVG=0 counts by definition, σ=346 counts/s/mW).

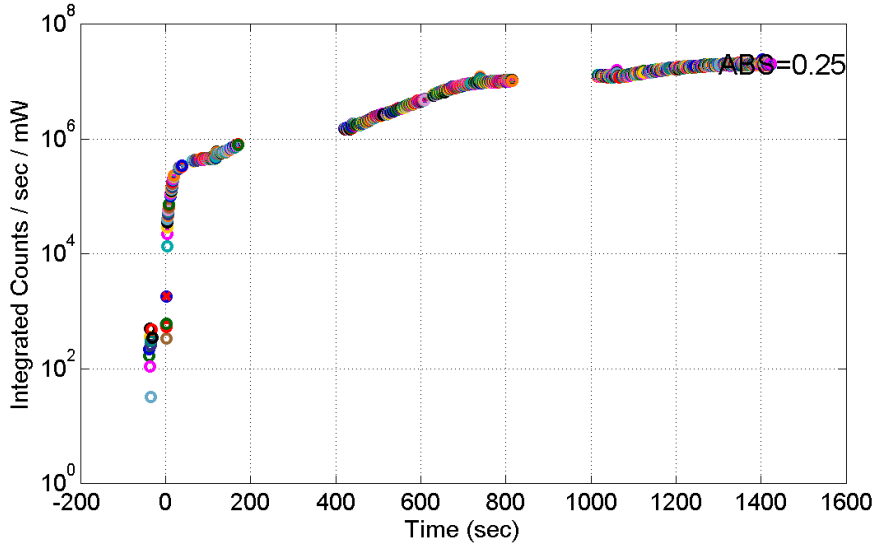

Figure 4.19: SXe deposition history using 555 nm excitation. Observed first signal was 1814 counts per second per mW of laser power, shown as the blue circle with the red center. Three total barium depositions were made to eventually get to the 0.25 absorbance value. Negative values (after background subtraction) are plotted as the as the absolute value.

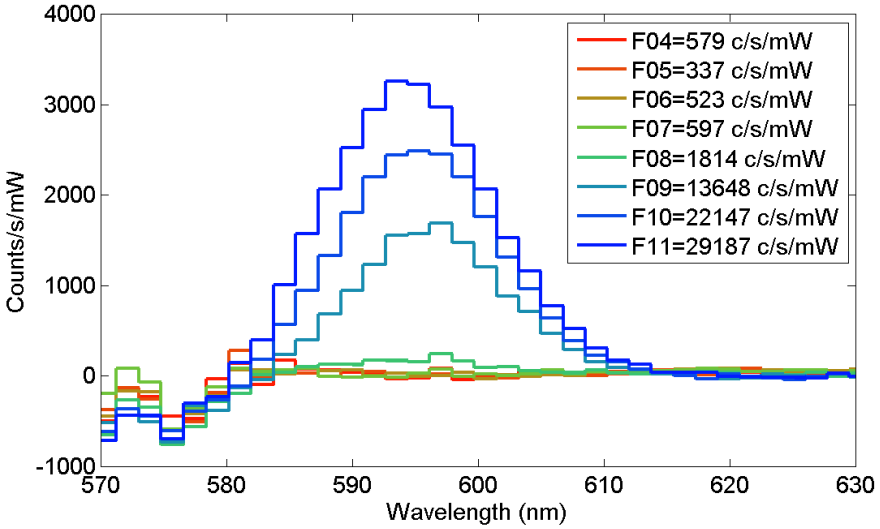

Figure 4.20: First detectable spectrum for barium atoms in solid xenon was F08.

Table 4.4: Experimental parameters for detection limit using 558 nm excitation.

Frame	Counts/s/mW	Exp(s)	Laser(mW)	Atoms
F08	1814	0.3	4.3	20700
F09	13647	0.3	4.3	156000
ABS=0.25	1.87E^{7}	0.1	1.336	2.14E^{8}

This corresponded to a first signal of 20,000 barium atoms! Experimental figures can be found in Table 4.4 for this calculation.

The fluorescence efficiency at the absorption measurement can be calculated as before using Eqn. 4.3. The absorption measured at the end of the run was 0.25, and the laser power was 1.3 mW, giving 9.4×10^{14} absorptions/sec (see Eqn. 4.2). The corresponding fluorescence count rate for this measurement was 2.50×10^{7} counts/sec. This gives a total fluorescence efficiency of 0.1%. This efficiency is significantly higher than that found when exciting with 532 nm.

Fluorescence measurements made with the dye laser tuned to the peak absorption of barium in solid xenon was demonstrated to be sensitive to small numbers of barium atoms. The stable fluorescence behavior provides strong signal over long exposure times and high laser power intensities which will be needed for single atom detection. Fluorescence efficiencies were higher with the dye laser, particularly since bleaching did not occur. These efficiencies, while still low, are sufficient for single atom detection with other system improvements like detection efficiency and increased excitation rates.

4.3 Single molecule detection with a fiber optic probe

Tests of the fiber optic detector probe concept were were made with diluted Rhodamine 6G (R6G) dye solutions. These solutions served as convenient analogues for barium atoms or ions placed at the fiber tip. Results using ethylene glycol as the solvent are presented first, followed by results with methanol as a solvent. In an attempt to find a better analogue to barium frozen to the tip, initial tests with quantum dots dried on the tip of the fiber probe are then discussed.

4.3.1 Fiber probe detection of R6G molecules in ethylene glycol

Solutions of pure ethylene glycol and a diluted dye solution of 4 molecules per 100 μm^3 detection volume were alternately measured, with five spectra taken in each measurement. Analysis was done with spectral fits of the R6G and backgrounds, as

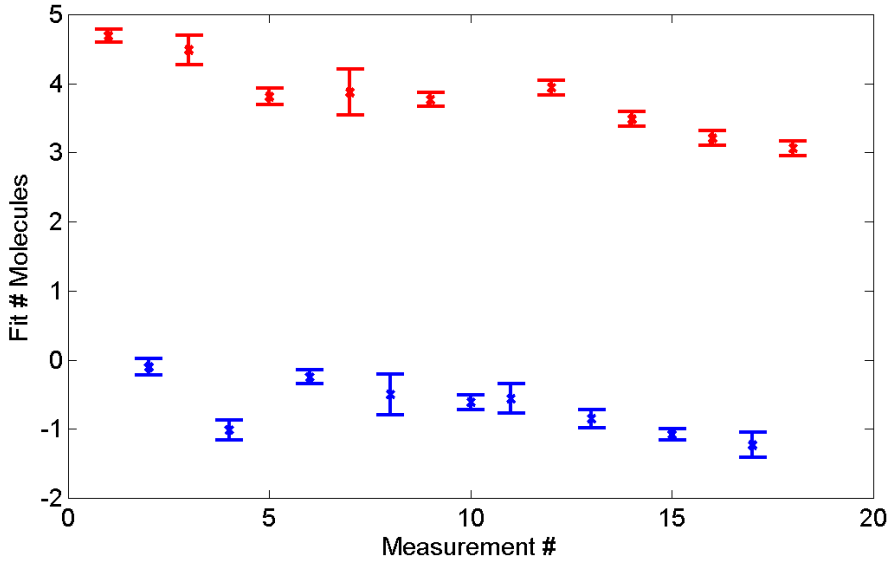

Figure 4.21: Fiber detector measurements of 4 molecules per 100 μm^3 solutions (red) and pure ethylene glycol (blue). Errors are plotted as one standard deviation of the five measurements.

outlined in Section 3.4.3. The mean and standard deviation of the fit R6G weight is plotted for each set, shown in Fig. 4.21. This demonstration shows the fiber probe detector was able to distinguish between 4 molecule and 0 molecule solutions with less than one molecule variation. The trend downwards could be due to gradual loss of dye-molecules attached to the cladding or fiber face from the calibration solution with high concentration of R6G.

4.3.2 Fiber optic probe quantum dot detection

The sensitivity of the fiber probe method at the single dot level could be clearly demonstrated by detecting blinking of a single quantum dot on the tip of the fiber probe. Quantum dots diluted in hexane showed clear fluorescence signal using the

same analysis techniques as the R6G dye (Fig. 4.22). The goal, however, was to dry a single dot at the tip of the fiber probe directly in front of the core, and observe blinking fluorescence signal from a single quantum dot.

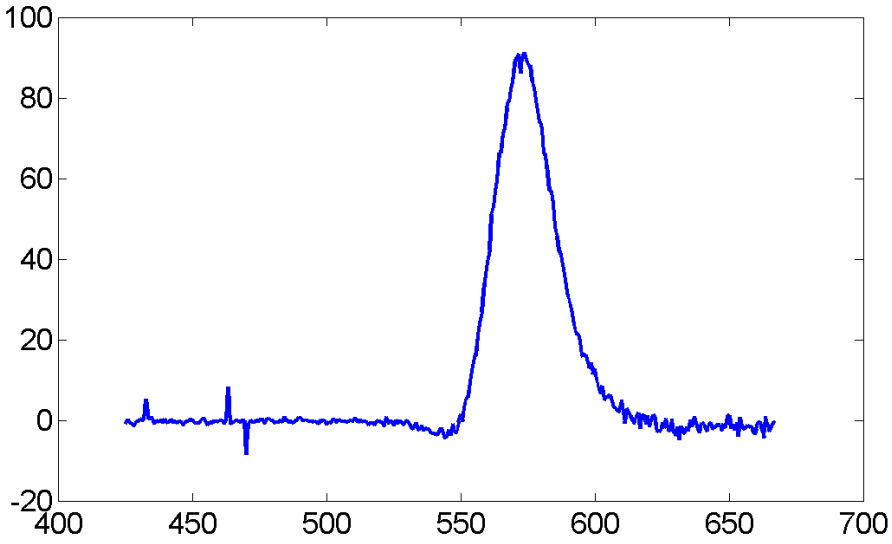

Figure 4.22: Quantum dot fluorescence of a dilute solution detected with the fiber probe.

Detecting dried quantum dots on a fiber tip used a similar procedure to the detection of R6G molecules. A spectrum of concentrated quantum dots in solution was used to define the quantum dot spectrum. A bare fiber defined the background. The fiber tip was then dipped into a solution of quantum dots and then removed. Spectra taken just after removal were so called 'fresh' spectra. To determine if a dot was on the tip, spectra were taken continuously that could be fit using spectral shapes of the dot fluorescence and backgrounds (just like the dye molecule demonstration in section 3.4.3). A series of spectra were also taken after a 5 minute drying period. The quantum dot fit plotted as a function of time for a typical experiment is shown in

Fig. 4.23. If a quantum dot was on the fiber tip the fluorescence signal should have fluctuated between one and zero over this time scale. All attempts to dry quantum dots on the fiber tip by dipping the fiber in solutions failed to yield fluorescence signals. It is possible that the concentrations used for these experiments (2000 μm^{-3}) were just too low.

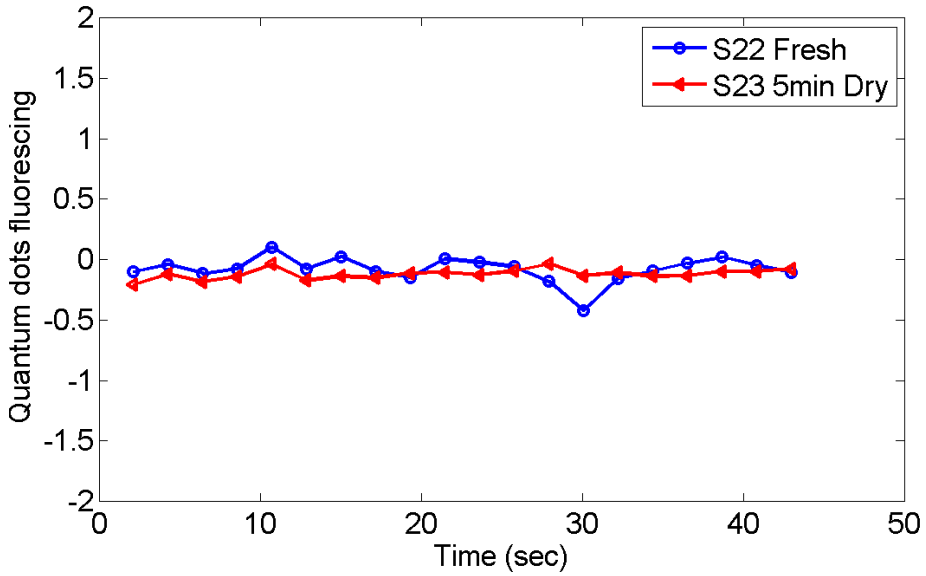

Figure 4.23: Fluorescence contribution of quantum dots on the end of a fiber detected after dipping in a dilute solution, directly after dipping (Fresh), and after a 5 minute dry.

Chapter 5

Discussion

Fluorescence spectroscopy of barium in solid xenon is reported for the first time for the $6s6p\ ^1P_1 \rightarrow 6s^2\ ^1S_0$ transition. The largest absorption was found to be at 557.2 nm, and the emission is primarily at 594 nm. Additional absorption peaks were also found to the blue of the main absorption region, centered at 457, 463, and 470 nm. The exact energy level transitions have not been determined for these blue absorptions. Excitation with several fixed frequency wavelengths in this region with an argon-ion laser caused additional emission peaks to be observed. Absorption and fluorescence component wavelengths for barium in solid argon and solid xenon are summarized in Table 5.1. In all cases the corresponding transition in solid xenon is shifted to the red relative to that of solid argon.

The behavior of barium atoms in various local configurations (sites) inside solid xenon have been studied. Atoms in different sites respond differently to excitation. This is important to understand for future single atom studies. The local environment of an atom can change long after it has been deposited, both with excitation from a laser, and through annealing the solid host. Atoms in solid xenon prefer a particular

Table 5.1: Summery of the spectrum of barium in solid xenon.

Absorption (nm)			
Transition	Vacuum	SXe	SAr
$6s^2\ ^1S_0 \rightarrow 6s6p\ ^1P_1$	553.7	537.7	512.4
		549.8	527
		557.2	543
		562.7	554.5
Unknown		457	452
		463	461
		470	465
Fluorescence Emission (nm)			
Transition	Vacuum	SXe	SAr
$6s6p\ ^1P_1 \rightarrow 6s^2\ ^1S_0$	553.7	579	538.6
		594	549.1
			558.4
Unknown		482.4	
		492.4	
		532.4	
		552.2	

local configuration. This was shown by annealing studies (Fig. 4.16) where the main fluorescing peak grew as other side peaks decreased. Excitation at 532 nm in a small unstable site peak also caused conversion to the dominant stable site. Successful single atom detection in solid xenon may need to use some form of annealing or off-resonance excitation to move an atom in an unstable site to the stable and strong fluorescing site.

Fluorescence loss due to optical pumping or photo bleaching could be due to atoms moving out of sites that were strongly absorbing the excitation light to sites that have lower absorption cross-sections at that wavelength. This is supported by observation of strong bleaching using 532 nm excitation (Fig. 4.11), which excites atoms in the

lowest wavelength absorption peak at 537.7 nm (an unstable site). As atoms in this site absorb, they may be able to reconfigure their site to the one that absorbs at 557.2 nm. Observations of increased fluorescence signal with exposure to 557.2 nm excitation support the theory that atoms in other sites may be converting to this site. No bleaching or optical pumping was observed using 558 nm excitation with the highest absorption rates that could be obtained in the current setup. The decay rate out of the metastable D states has been shown to be greater than 10^4 per second (Fig. 4.18). This rapid depletion from the D states means detection can be performed with a single laser wavelength, tuned to the stable site absorption wavelength.

Detection of $\sim 2 \times 10^4$ atoms (Fig. 4.20) with the current spectroscopic setup demonstrates the viability of detecting single barium atoms in solid xenon. Seven orders in sensitivity can be gained with improvements to collection efficiency, excitation rate, and exposure time. This means that the potential sensitivity for detection barium in solid xenon is less than one atom. Collection efficiency can be increased by placing a collection lens much closer to the sample plate with a larger collection area (e.g., Fig. 2.6), this might increase the collection efficiency by 10^2. Trading out the fiber coupler and spectrometer-CCD with a single photon counting avalanche photo diode could improve collection efficiency by a factor of 10^2. With additional laser blocking filters, exposure time and laser intensity could have been increased in the previous detection limit experiment. A factor of more than 10^3 in signal might be obtainable. Together these factors make single atom detection in solid xenon a very promising method for tagging in EXO.

Sensitivity measurements made with the fiber optic detector (Fig. 4.21) show reasonable ability to detect a few Rhodamine 6G molecules in solution. This sensitivity is the first reported on the single molecule scale for this kind of detector. This fiber

optic based detector apparatus may find use in any number of high precision fluorescent measurement applications where access is limited. The limited fluorescence efficiency of barium in solid xenon may prevent detection of a single atom with the fiber probe arrangement of Fig. 3.14 because of fluctuations in the silica Raman background. However, an external tip scanning arrangement (Fig. 2.6), would eliminate the silica Raman problem and is very promising for single barium atom detection in solid xenon.

Bibliography

[1] F.T. Avignone III, S.R. Elliott, and J. Engel. "Double beta decay, Majorana neutrinos, and neutrino mass". In: *Reviews of Modern Physics* 80.2 (2008), p. 481.

[2] MK Moe. "Detection of neutrinoless double-beta decay". In: *Physical Review C* 44.3 (1991), pp. 931–934.

[3] C. L. Cowan et al. "Detection of the Free Neutrino: a Confirmation". In: *Science* 124.3212 (1956), pp. 103–104. DOI: 10.1126/science.124.3212.103. eprint: http://www.sciencemag.org/content/124/3212/103.full.pdf. URL: http://www.sciencemag.org/content/124/3212/103.short.

[4] Raymond Davis, Don S. Harmer, and Kenneth C. Hoffman. "Search for Neutrinos from the Sun". In: *Phys. Rev. Lett.* 20.21 (1968), pp. 1205–1209. DOI: 10.1103/PhysRevLett.20.1205.

[5] Bruce T. Cleveland et al. "Measurement of the Solar Electron Neutrino Flux with the Homestake Chlorine Detector". In: *The Astrophysical Journal* 496.1 (1998), p. 505. URL: http://stacks.iop.org/0004-637X/496/i=1/a=505.

[6] Y. Fukuda et al. "Measurement of a small atmospheric $\nu\mu/\nu$e ratio". In: *Physics Letters B* 433.1-2 (1998), pp. 9–18.

[7] SM Bilenky. "The history of neutrino oscillations". In: *Physica Scripta* 2005 (2005), p. 17.

[8] R.N. Mohapatra et al. "Theory of neutrinos: a white paper". In: *Reports on Progress in Physics* 70 (2007), p. 1757.

[9] Q. R. Ahmad et al. "Measurement of the Rate of $\nu_e + d \rightarrow p + p + e^-$ Interactions Produced by ^8B Solar Neutrinos at the Sudbury Neutrino Observatory". In: *Phys. Rev. Lett.* 87.7 (2001), p. 071301. DOI: 10.1103/PhysRevLett.87.071301.

[10] G. Alimonti et al. "The Borexino detector at the Laboratori Nazionali del Gran Sasso". In: *Nuclear Instruments and Methods in Physics Research Section A: Accelerators, Spectrometers, Detectors and Associated Equipment* 600.3 (2009), pp. 568 –593. ISSN: 0168-9002. DOI: 10.1016/j.nima.2008.11.076. URL: http://www.sciencedirect.com/science/article/pii/S016890020801601X.

[11] Y. Ashie et al. "Evidence for an Oscillatory Signature in Atmospheric Neutrino Oscillations". In: *Phys. Rev. Lett.* 93.10 (2004), p. 101801. DOI: 10.1103/PhysRevLett.93.101801.

[12] T. Araki et al. "Measurement of Neutrino Oscillation with KamLAND: Evidence of Spectral Distortion". In: *Phys. Rev. Lett.* 94.8 (2005), p. 081801. DOI: 10.1103/PhysRevLett.94.081801.

[13] E. Aliu et al. "Evidence for Muon Neutrino Oscillation in an Accelerator-Based Experiment". In: *Phys. Rev. Lett.* 94.8 (2005), p. 081802. DOI: 10.1103/PhysRevLett.94.081802.

[14] P. Adamson et al. “First Direct Observation of Muon Antineutrino Disappearance”. In: *Phys. Rev. Lett.* 107 (2 2011), p. 021801. DOI: 10.1103/PhysRevLett.107.021801. URL: http://link.aps.org/doi/10.1103/PhysRevLett.107.021801.

[15] Leslie Camilleri, Eligio Lisi, and John F. Wilkerson. “Neutrino Masses and Mixings: Status and Prospects”. In: *Annual Review of Nuclear and Particle Science* 58.1 (2008), pp. 343–369. DOI: 10.1146/annurev.nucl.57.090506.123038. eprint: http://www.annualreviews.org/doi/pdf/10.1146/annurev.nucl.57.090506.123038. URL: http://www.annualreviews.org/doi/abs/10.1146/annurev.nucl.57.090506.123038.

[16] SM Bilenky et al. “Absolute values of neutrino masses: Status and prospects”. In: *Physics reports* 379.2 (2003), pp. 69–148.

[17] G. L. Fogli et al. “Evidence of theta(13)¿0 from global neutrino data analysis”. In: (2011). arXiv:1106.6028 [hep-ph].

[18] K. Abe et al. “Indication of Electron Neutrino Appearance from an Accelerator-produced Off-axis Muon Neutrino Beam”. In: *Phys. Rev. Lett.* 107 (2011), p. 041801. DOI: 10.1103/PhysRevLett.107.041801. arXiv:1106.2822 [hep-ex].

[19] G. L. Fogli et al. “Observables sensitive to absolute neutrino masses: Constraints and correlations from world neutrino data”. In: *Phys. Rev. D* 70.11 (2004), p. 113003. DOI: 10.1103/PhysRevD.70.113003.

[20] M. Prall. “The Katrin experiment and the pre-spectrometer at reduced retarding potential”. In: *Progress in Particle and Nuclear Physics* 66.2 (2011). Particle and Nuclear Astrophysics, International Workshop on Nuclear Physics, 32nd Course, pp. 418 –423. ISSN: 0146-6410. DOI: DOI:10.1016/j.ppnp.2011.01.0

44. URL: http://www.sciencedirect.com/science/article/pii/S0146641011000457.

[21] Alessandro Melchiorri, Francesco De Bernardis, and Eloisa Menegoni. "Limits on the neutrino mass from cosmology". In: *AIP Conference Proceedings* 1256.1 (2010). Ed. by H. A. Morales-Tecotl et al., pp. 96–106. DOI: 10.1063/1.3473882. URL: http://link.aip.org/link/?APC/1256/96/1.

[22] Øystein Elgarøy and Ofer Lahav. "Neutrino masses from cosmological probes". In: *New Journal of Physics* 7.1 (2005), p. 61. URL: http://stacks.iop.org/1367-2630/7/i=1/a=061.

[23] B. Pritychenko. "On Double-Beta Decay Half-Life Time Systematics". In: (2010). arXiv:1004.3280 [nucl-th].

[24] M. Redshaw et al. "Mass and Double-Beta-Decay Q Value ofˆ{136} Xe". In: *Physical review letters* 98.5 (2007), p. 53003.

[25] M. Danilov et al. "Detection of very small neutrino masses in double-beta decay using laser tagging". In: *Physics Letters B* 480.1-2 (2000), pp. 12–18. ISSN: 0370-2693.

[26] HV Klapdor-Kleingrothaus and IV Krivosheina. "THE EVIDENCE FOR THE OBSERVATION OF $0\nu\beta\beta$ DECAY". In: *Modern Physics Letters A* 21.20 (2006), pp. 1547–1566.

[27] CE Aalseth et al. "Comment on "Evidence for neutrinoless double beta decay"". English. In: *MODERN PHYSICS LETTERS A* 17.22 (2002), 1475–1478. ISSN: 0217-7323.

[28] Ferruccio Feruglio, Alessandro Strumia, and Francesco Vissani. "Neutrino oscillations and signals in [beta] and 0[nu]2[beta] experiments". In: *Nuclear Physics B* 637.1-3 (2002), pp. 345 –377. ISSN: 0550-3213. DOI: DOI:10.1016/S0550-3213(02)00345-0. URL: http://www.sciencedirect.com/science/article/pii/S0550321302003450.

[29] HL Harney. "Reply to the Comment on". In: *Arxiv preprint hep-ph/0205293* (2002).

[30] HV Klapdor-Kleingrothaus. "Lessons after the evidence for $0\nu\beta\beta$ decay". In: *Physica Scripta* 2006 (2006), p. 40.

[31] Vladimir I. Tretyak and Yuri G. Zdesenko. "Tables of double beta decay–an update". In: *Atomic Data and Nuclear Data Tables* 80.1 (2002), pp. 83 –116. ISSN: 0092-640X. DOI: DOI:10.1006/adnd.2001.0873. URL: http://www.sciencedirect.com/science/article/B6WBB-45FK5YD-3/2/3f2307dae6141525a69b57d8bd20086a.

[32] R. Luescher et al. "Search for [beta][beta] decay in 136Xe: new results from the Gotthard experiment". In: *Physics Letters B* 434.3-4 (1998), pp. 407 –414. ISSN: 0370-2693. DOI: DOI:10.1016/S0370-2693(98)00906-X. URL: http://www.sciencedirect.com/science/article/pii/S037026939800906X.

[33] M.Z. Iqbal et al. "Design and construction of a high pressure xenon time projection chamber". In: *Nuclear Instruments and Methods in Physics Research Section A: Accelerators, Spectrometers, Detectors and Associated Equipment* 259.3 (1987), pp. 459 –465. ISSN: 0168-9002. DOI: DOI:10.1016/0168-9002(87)90827-8. URL: http://www.sciencedirect.com/science/article/pii/0168900287908278.

[34] J. C. Vuilleumier et al. "Search for neutrinoless double-β decay in ^{136}Xe with a time projection chamber". In: *Phys. Rev. D* 48.3 (1993), pp. 1009–1020. DOI: 10.1103/PhysRevD.48.1009.

[35] E. Conti et al. "Correlated fluctuations between luminescence and ionization in liquid xenon". In: *Physical Review B* 68.5 (2003), p. 054201.

[36] D.S. Leonard et al. "Systematic study of trace radioactive impurities in candidate construction materials for EXO-200". In: *Nuclear Instruments and Methods in Physics Research Section A: Accelerators, Spectrometers, Detectors and Associated Equipment* 591.3 (2008), pp. 490 –509. ISSN: 0168-9002. DOI: DOI:10.1016/j.nima.2008.03.001. URL: http://www.sciencedirect.com/science/article/pii/S016890020800346X.

[37] M. Green et al. "Observation of single collisionally cooled trapped ions in a buffer gas". In: *Phys. Rev. A* 76.2 (2007), p. 023404. DOI: 10.1103/PhysRevA.76.023404.

[38] P. Fierlinger et al. "A microfabricated sensor for thin dielectric layers". In: *Review of Scientific Instruments* 79 (2008), p. 045101.

[39] SC Jeng, WM Fairbank, and M. Miyajima. "Measurements of the mobility of alkaline earth ions in liquid xenon". In: *Journal of Physics D: Applied Physics* 42 (2009), p. 035302.

[40] JJ Curry. "Compilation of Wavelengths, Energy Levels, and Transition Probabilities for Ba I and Ba II". In: *Journal of Physical and Chemical Reference Data* 33.3 (2004), pp. 725–746.

[41] D. A. Lewis et al. "Determination of the branching of the $^1P_1$ Ba i level from studies of the intensity dependence of resonance fluorescence". In: *Phys. Rev. A* 35.1 (1987), pp. 131–134. DOI: 10.1103/PhysRevA.35.131.

[42] S. Niggli and M. C. E. Huber. "Transition probabilities in neutral barium". In: *Phys. Rev. A* 35.7 (1987), pp. 2908–2918. DOI: 10.1103/PhysRevA.35.2908.

[43] G. K. Gerke and B. A. Bushaw. "Measurement of weak branching out of the (near-) two-level system Ba 6s6p 1P1 6s2 1S0". In: *Phys. Rev. A* 37.5 (1988), pp. 1502–1506. DOI: 10.1103/PhysRevA.37.1502.

[44] A. Bizzarri and M. C. E. Huber. "Transition probabilities from the 6s6p $^1P^\circ_1$ resonance level of neutral barium". In: *Phys. Rev. A* 42.9 (1990), pp. 5422–5424. DOI: 10.1103/PhysRevA.42.5422.

[45] Eric W. Weisstein. *Geometric Distribution*. From MathWorld–A Wolfram Web Resource. 2011. URL: http://mathworld.wolfram.com/GeometricDistribution.html.

[46] D. A. Lewis et al. "Photon-burst method in high-resolution laser spectroscopy". In: *Phys. Rev. A* 19.4 (1979), pp. 1580–1588. DOI: 10.1103/PhysRevA.19.1580.

[47] V.E. Bondybey, A.M. Smith, and J. Agreiter. "New developments in matrix isolation spectroscopy". In: *Chem. Rev* 96.6 (1996), pp. 2113–2134.

[48] E. Whittle, D.A. Dows, and G.C. Pimentel. "Matrix isolation method for the experimental study of unstable species". In: *The Journal of Chemical Physics* 22 (1954), p. 1943.

[49] Beat Meyer. *Low Temperature Spectroscopy*. Ed. by Beat Meyer. American Elsevier Publishing Company, Inc., 1971.

[50] Robert Pellow and Martin Vala. "The external heavy atom effect: Theory of spin?orbit coupling of alkali and noble metals in rare gas matrices". In: 90.10 (1989), pp. 5612–5621. ISSN: 00219606. DOI: DOI:10.1063/1.456414. URL: http://dx.doi.org/10.1063/1.456414.

[51] LC Balling and JJ Wright. "Absorption and emission spectra of matrix-isolated Ba atoms". In: *The Journal of chemical physics* 83.5 (1985), pp. 2614–2615. ISSN: 0021-9606.

[52] WE Moerner. "A dozen years of single-molecule spectroscopy in physics, chemistry, and biophysics". In: *The Journal of Physical Chemistry B* 106.5 (2002), pp. 910–927.

[53] WE Moerner and D.P. Fromm. "Methods of single-molecule fluorescence spectroscopy and microscopy". In: *Review of Scientific Instruments* 74 (2003), p. 3597.

[54] T. Govindaunny and BM Sivaram. "Solvent effects on the gain of rhodamine 6G". In: *Applied Physics A: Materials Science & Processing* 23.3 (1980), pp. 253–258.

[55] Exciton. *Rhodamine 590*. Exciton. 2011. URL: http://www.exciton.com/pdfs/RH590.pdf.

[56] A.L. Efros. "Nanocrystals: almost always bright". In: *Nature Materials* 7.8 (2008), pp. 612–613.

[57] S. Tam and M.E. Fajardo. "Matrix isolation spectroscopy of metal atoms generated by laser ablation. III. The Na/Ar, Na/Kr, and Na/Xe systems". In: *The Journal of chemical physics* 99 (1993), p. 854.

Appendix A

Model of collection efficiency

The collection efficiency has been modeled using simple optical theory. Collection apparatus was described in Section 3.2. This model calculates the collection efficiency as a function of the lens position.

```
% coupler efficiency
D_lens = 1; %cm
D_fiber = 0.127; %cm
d_lf = 1.6; %distance from lens t0 fiber cm
f = 2; %cm focal length
N_fiber = 4; % f# for the fiber
N_lens = f/D_lens; % f# for the lens (lookup working f#)
e_QM = 0.9;
e_ref = 0.9;
e_fiber = 0.5;
e_cnt = 0.5;
e_spec = 0.5;

clear x; clear y; clear h;


for i=1:100;
    x(i)=i/10; % convert x to cm w/ mm resolution
    S(i) = 1/(1/f - 1/x(i))
    f_num(i) = (S(i)/D_lens)^2 / (N_fiber)^2;
    h(i)=(D_lens/2)*(1-d_lf*(1/f - 1/x(i))); %imaging factor
    y(i)=((D_fiber/2)^2/h(i)^2) *...
        (D_lens^2/(4*x(i)^2)) * ...
```

```
        e_QM*e_fiber*e_cnt*e_spec*f_num(i)*e_ref^2;
    disp(['x=' num2str(x(i)) ' y=' num2str(y(i))]);
end

figure1 = figure(1); clf;
axes1 = axes('Parent',figure1,'YMinorTick','off',...
    'PlotBoxAspectRatio',[1 0.6 1],...
    'FontSize',14);
box(axes1,'on');
hold(axes1,'all');
plot(x,y,'linewidth',2);
%axis([4,8,0.8e-5,1.6e-5]);
xlim([4,8])
grid on;
ylabel('Counts per emitted photon');
xlabel('Detector distance (cm)');
print('collection_efficiency.png','-dpng');
```

Appendix B

Fiber optic collection efficiency

The collection efficiency as a function of volume was calculated with Monte-Carlo method for the fiber optic probe detector. This code performs the MC for each ray, and determines if the ray was accepted by the fiber core.

```
% A program to simulate the coupling of a molecule into a fiber optic.
function ratio = fibersim(z,d,SIM_NUM)

NA = 0.13;
D_CORE = 3.5; % micro meters

accept_angle = asin(NA);
PIby2 = pi/2;

coupled = 0;
for i = 1:SIM_NUM
    theta = acos(1-2*rand);
    phi = rand*2*pi;
    % exclude rays that can't even be accepted

    if theta >= pi - accept_angle
        %The ray is acceptable, but depending on z and d the ray may not
            go into the core
        %project the ray into the fiber plane
        x0 = d + z * tan(pi - theta) * cos(phi);
        y0 = z * tan(pi - theta) * sin(phi);
        if sqrt(x0^2 + y0^2) <= D_CORE
            coupled=coupled+1;
```

```
        end
    end
end

ratio = coupled / SIM_NUM;
```

Appendix C

Two and three function fitting algorithms

The fitting of spectra with multiple distinct components that could be measured was performed using these scripts. The code takes the spectrum that is to be fit and the individual component spectra and returns the amplitude of the component spectra which minimizes the residue over the whole spectrum.

C.1 Two function fitting

```
% Two function fits for the spectra dater
% function [a,b] = twoFn_fit(F,Ya,Yb)

function [a,b] = twoFn_fit(F,Ya,Yb)

%check length of the files is identical
for i = 1:length(F)
    iX11(i) = Ya(i)*Ya(i);
    iX12(i) = Ya(i)*Yb(i);
    iX22(i) = Yb(i)*Yb(i);
    iY1(i) = F(i)*Ya(i);
```

```
    iY2(i) = F(i)*Yb(i);
end

X11 = sum(iX11);
X12 = sum(iX12);

X21 = X12;
X22 = sum(iX22);

Y1 = sum(iY1);
Y2 = sum(iY2);

D = (X11*X22 - X21*X12);
a = (Y1*X22 - X21*Y2)/D;
b = (X11*Y2 - Y1*X12)/D;
```

C.2 Three function fitting

```
% Three function fits for the spectra dater
% function [a,b,c] = threeFn_fit(F,Ya,Yb,Yz)

function [a,b,c] = threeFn_fit(F,Ya,Yb,Yc)

%check length of the files is identical
for i = 1:length(F)
    iX11(i) = Ya(i)*Ya(i);
    iX12(i) = Ya(i)*Yb(i);
    iX13(i) = Ya(i)*Yc(i);
    iX22(i) = Yb(i)*Yb(i);
    iX23(i) = Yb(i)*Yc(i);
    iX33(i) = Yc(i)*Yc(i);
    iY1(i) = F(i)*Ya(i);
    iY2(i) = F(i)*Yb(i);
    iY3(i) = F(i)*Yc(i);
end

X11 = sum(iX11);
X12 = sum(iX12);
X13 = sum(iX13);
X21 = X12;
X22 = sum(iX22);
X23 = sum(iX23);
X31 = X13;
X32 = X23;
X33 = sum(iX33);
Y1 = sum(iY1);
```

```
29 Y2 = sum(iY2);
30 Y3 = sum(iY3);
31
32 D = X11*(X22*X33 - X32*X23) - X21*(X12*X33 - X32*X13) + X31*(X12*X23 -
       X22*X13);
33 a = (Y1*(X22*X33 - X32*X23) - X21*(Y2*X33 - X32*Y3) + X31*(Y2*X23 - X22*
       Y3))/D;
34 b = (X11*(Y2*X33 - X32*Y3) - Y1*(X12*X33 - X32*X13) + X31*(X12*Y3 - Y2*
       X13))/D;
35 c = (X11*(X22*Y3 - Y2*X23) - X21*(X12*Y3 - Y2*X13) + Y1*(X12*X23 - X22*
       X13))/D;
```